

(NASA-CR-176485) ANALYSES OF
QUASI-ISOTROPIC COMPOSITE PLATES UNDER
QUASI-STATIC POINT LOADS SIMULATING
LOW-VELOCITY IMPACT PHENOMENA Final Report
(Old Dominion Univ., Norfolk, Va.) 207 p

N86-17475

G3/24 Unclassified
05314

ABSTRACT

ANALYSES OF QUASI-ISOTROPIC COMPOSITE PLATES UNDER QUASI-STATIC POINT LOADS SIMULATING LOW-VELOCITY IMPACT PHENOMENA

Ajit Dhundiraj Kelkar
Old Dominion University, 1985
Director: Dr. Ram Prabhakaran
Co-Director: Dr. W. Elber

Composite laminates have high strength to density ratios that make them attractive for use in aircraft structures. However, the damage tolerance of these materials is limited because they have very low ultimate strains, no plastic deformation range, and no usable strength in the thickness direction. These limitations are very obvious when laminates are subjected to impact loads. Due to these impact loads, laminates suffer visible and invisible damage. To improve the material performance in impact requires a better understanding of the deformation and damage mechanics under impact type loads.

In thin composite laminates, the first level of visible damage occurs on the back face and is called "back face spalling." A plate-membrane coupling model, and a finite element model to analyze the large deformation behavior of eight-ply quasi-isotropic circular composite plates under impact type point loads are developed. The back face spalling phenomenon in thin composite plates is explained by using the plate-membrane coupling model and the finite element model in conjunction with the fracture mechanics principles. The experimental results verifying these models are presented. The study resulted in the

following conclusions:

1. The large deformation behavior of circular isotropic membranes subjected to arbitrary axisymmetric loading can be obtained by solving a single nonlinear governing equation in terms of a radial stress.
2. Accurate large deflection behavior of circular quasi-isotropic T300/5208 laminates can be obtained by using a simple plate-membrane coupling model.
3. The functional form of deformed shape of the plate undergoing large deformations is different from the small deflection plate solution.
4. The back face spalling action in thin composite laminates is a spontaneous action and can be predicted by using the fracture mechanics principles.
5. Mixed mode (I and II) type deformations probably occur during back face spalling, however, mode I appears to govern the delamination growth during the spalling action.

ANALYSES OF QUASI-ISOTROPIC COMPOSITE PLATES UNDER QUASI-STATIC
POINT LOADS SIMULATING LOW-VELOCITY IMPACT PHENOMENA

by

Ajit Dhundiraj Kelkar
B.E., June 1975, Pune University, India
M.S., December 1981, South Dakota State University

A Dissertation Submitted to the Faculty of
Old Dominion University in Partial Fulfillment of the
Requirements for the Degree of

DOCTOR OF PHILOSOPHY

ENGINEERING MECHANICS

OLD DOMINION UNIVERSITY
August 1985

Approved by:

R. Prabhakaran

Dolf Aker

Tom W. Horwitz

John Siveth
Pramote Dechaumphai

AKNOWLEDGEMENTS

The author wishes to express his sincere gratitude to his advisor, Dr. Ram Prabhakaran, for all the help and effort provided during the course of this study at Old Dominion University. He is also indebted to Dr. Wolf Elber, of NASA Langley Research Center, whose friendly guidance and direction made this work possible.

Special thanks are due to Dr. I. S. Raju, who has been the author's guide and mentor throughout this course of study. He is also grateful to Dr. A. Sidney Roberts, Jr. for his support through the Aeronautics Research Participation Program, grant number NGR 47-003-052, which included invaluable accessibility to research facilities at NASA Langley Research Center in Hampton, Virginia. He also wishes to thank researchers at the NASA Fatigue and Fracture Branch for their help and encouragement, especially to Dr. John Crews, Dr. Shivakumar, and Mr. John Whitcomb for their valuable suggestions and comments.

The author extends his thanks to Ms. Wendy Keene who performed an exemplary and expedient job of typing throughout the preliminary and final stages of the manuscript. The author is very grateful to his parents Mr. and Mrs. D. D. Kelkar for their constant support and encouragement in this endeavor. Lastly, the author wishes to thank his wife, Vinaya, for her patience, help, and considerable understanding.

TABLE OF CONTENTS

	Page
ACKNOWLEDGEMENTS	ii
LIST OF TABLES	vii
LIST OF FIGURES	viii
LIST OF SYMBOLS	xi
Chapter	
1. INTRODUCTION	1
1.1 Motivation	1
1.2 Scope and Objectives	4
1.3 Review of Earlier Work	5
1.3.1 Experimental Studies	6
1.3.2 Theoretical Studies	7
1.4 Proposed Methods of Analyses	9
1.4.1 Plate-Membrane Coupling Model	9
1.5 Layout of Presentation	12
2. SMALL DEFLECTION PLATE ANALYSIS	15
2.1 Introduction	15
2.2 Plate Configuration	15
2.3 Assumptions	17
2.4 The Governing Differential Equation	18
2.5 Derivation of the Equivalent Flexural Modulus	21
2.6 Solution Method	26

2.6.1 Application of the Finite Difference Method for the Solution of Arbitrarily Loaded Clamped Circular Plate	29
2.6.2 Boundary Conditions	30
2.7 Illustrative Example	30
2.7.1 Problem Formulation	31
2.8 Convergence Study	37
2.9 Results and Discussion	37
2.10 Concluding Remarks	40
3. LARGE DEFLECTION MEMBRANE ANALYSIS	45
3.1 Introduction	45
3.2 Membrane Configuration and Strain- Displacement Relations	47
3.2.1 Equilibrium Equations	49
3.2.2 Derivation of a Governing Equation	53
3.3 Solution Method	55
3.3.1 Boundary Conditions	57
3.3.2 Illustrative Example	58
3.4 Convergence Study	62
3.4.1 Uniformly Loaded Circular Membrane	67
3.4.2 A Membrane With Uniformly Distributed Load Over the Inner Portion $0 < \frac{r}{a} < 0.1$	70
3.4.3 A Membrane With a Ring Load	70
3.5 Discussion	75
3.6 Concluding Remarks	76
4. PLATE-MEMBRANE COUPLING MODEL	79
4.1 Introduction	79
4.2 Analysis	79
4.2.1 Plate Configuration	80

4.2.2 Problem-1: Plate Problem	80
4.2.3 Problem-2: Membrane Problem	82
4.2.4 Coupling of the Two Problems	83
4.3 Solution Method	88
4.4 Results and Discussion	89
4.5 Concluding Remarks	98
5. FINITE ELEMENT MODEL	102
5.1 Introduction	102
5.2 Finite Element Method	102
5.3 Plate Configuration	104
5.3.1 Strain-Displacement Relations	104
5.4 The Axisymmetric Finite Element	105
5.5 Stiffness Matrix of an Axisymmetric Element	109
5.5.1 Nonlinear Terms: Linearization Procedure	112
5.5.2 Boundary Conditions	118
5.6 Solution Procedure	119
5.7 Convergence Study	121
5.8 Results and Discussion	123
5.9 Concluding Remarks	128
6. PLATE MECHANICS EXPERIMENTS	133
6.1 Introduction	133
6.2 Test Set-up	133
6.3 Test Data	138
6.4 Results and Discussion	138
6.5 Concluding Remarks	144
7. BACK FACE SPALLING MODEL	145
7.1 Introduction	145

7.2 Back Face Spalling Mechanism	145
7.3 Fracture Mechanics Concepts	146
7.3.1 The Griffith Criterion	146
7.3.2 Critical Strain Energy Release Rate G	152
7.4 Back Face Spalling Model	152
7.5 Strain Energy Release Rate Results	160
7.6 Discussion of the Back Face Spalling Phenomenon	161
7.7 Back Face Spalling Experiments	165
7.8 Prevention of Back Face Spalling in Thin Composite Laminates	166
7.9 Conclusions	168
8. SUMMARY AND CONCLUSIONS	169
REFERENCES	173
APPENDICES	178
A. NEWTON-RAPHSON METHOD FOR NONLINEAR SYSTEMS	179
A.1 Newton-Raphson Method for One Dependent Variable	179
A.2 Newton-Raphson Method for n Variables	182
A.3 Example Problem	184
B. LARGE DEFLECTION SOLUTION OF CLAMPED CIRCULAR PLATE LOADED AT THE CENTER USING THE ENERGY METHOD	187
C. DERIVATION FOR THE RADIUS OF INFLECTION	191
BIOGRAPHY	192

LIST OF TABLES

TABLE	PAGE
2.1 Elastic Properties of the Plate	43
2.2 Comparison of Maximum Center Displacements for Uniformly Loaded Plate and for a Plate Uniformly Loaded over the Region $0 < \frac{r}{a} < 0.5$	44
3.1 Sensitivity of the Present Method for the Initial Values of σ_r	77
3.2 Comparison of Normalized Displacements and Stresses for Uniformly Loaded Membrane	78
4.1 Number of Iterations to Obtain Large Deflection Solution of a Clamped Circular Plate Under Central Concentrated Load Using the Plate-Membrane Coupling Model	99
4.2 (a) Comparison of the Transverse Displacements w Obtained by Using the $\frac{w^0}{h}$ Plate-Membrane Model and the Classical Solution for $\frac{w^0}{h}$ Ratios of 0.5 and 1.0	100
(b) Comparison of the Transverse Displacements w Obtained by Using the $\frac{w^0}{h}$ Plate-Membrane Model and the Classical Solution for $\frac{w^0}{h}$ Ratios of 1.5 and 2.0	101
5.1 Number of Iterations Required to Obtain Large Deformation Solution of a Clamped Circular Plate Under Central Point Load	130
5.2 (a) Comparison of the Transverse Displacements w Obtained by Using the Finite Element Model and the Plate-Membrane Coupling Model for $\frac{w^0}{h}$ Ratios of 0.5 and 1.0	131
(b) Comparison of the Transverse Displacements w Obtained by Using the Finite Element Model and the Plate-Membrane Coupling Model for $\frac{w^0}{h}$ Ratios of 1.5 and 2.0	132

LIST OF FIGURES

FIGURE	PAGE
1.1 Back Face Spalling in a Composite Plate	3
2.1 Plate Configuration	16
2.2 Equilibrium of the Plate Element	19
2.3 Arbitrary Axisymmetrically Loaded Circular Plate	22
2.4 Finite Differences for a Continuous Function $w = f(r)$	28
2.5 Four Region Idealization for the Plate Uniformly Loaded Over the Region $0 < \frac{r}{a} < 0.5$	32
2.6 Convergence Study for the Uniformly Loaded Plate	38
2.7 Convergence Study for the Plate Uniformly Loaded Over the Region $0 < \frac{r}{a} < 0.5$	39
2.8 Comparison of the Deflected Shape Obtained by Using the Finite Difference Method and the Exact Deflected Shape for the Uniformly Loaded Plate	41
2.9 Comparison of the Deflected Shape Obtained by Using the Finite Difference Method and the Exact Deflected Shape for the Plate Uniformly Loaded Over the Region $0 < \frac{r}{a} < 0.5$	42
3.1 Membrane Configuration	46
3.2 Radial Strain Due to Large Deflections	48
3.3 State of Stress on the Membrane Element	50
3.4 Stretched Circular Membrane	52
3.5 Four Region Idealization for the Membrane Uniformly Loaded Over the Region $0 < \frac{r}{a} < 0.5$	60
3.6 Types of Loading on the Membrane	63
3.7 Convergence Study for the Membrane (a) Uniform Loading	65

(b) Uniform Loading Over the Region $0 < \frac{r}{a} < 0.5$	66
3.8 Normalized Displacements for Uniformly Loaded Membrane	68
3.9 Normalized Stresses for Uniformly Loaded Membrane	69
3.10 Normalized Displacements in a Membrane Uniformly Loaded Over the Inner Portion $0 < \frac{r}{a} < 0.1$	71
3.11 Normalized Stresses in a Membrane Uniformly Loaded Over the Inner Portion $0 < \frac{r}{a} < 0.1$	72
3.12 Normalized Displacements in a Membrane with Ring Loading Over the Region $0.5 < \frac{r}{a} < 0.6$	73
3.13 Normalized Stresses in a Membrane with Ring Loading Over the Region $0.5 < \frac{r}{a} < 0.6$	74
4.1 Plate Configuration	81
4.2 Plate-Membrane Coupling Model	84
4.3 Flow Chart for the Plate-Membrane Coupling Model	85
4.4 Deflected Shapes for the Quasi-Isotropic Circular Plate Under Point Loads for $\frac{w_0}{h} = 0.5$ and 1.0	90
4.5 Deflected Shapes for the Quasi-Isotropic Circular Plate Under Point Loads for $\frac{w_0}{h} = 1.5$ and 2.0	91
4.6 Percentage Errors in the Classical Solution Relative to the Plate-Membrane Coupling Model Solution	93
4.7 Curvature Comparison for the Quasi-Isotropic Circular Plate Under Point Load	94
4.8 Movement of Radius of Inflection as a Function of Center Deflection	96
4.9 Load-Deflection Curve Comparison	97
5.1 Axisymmetric Element	106
5.2 Flow Chart for the Finite Element Model	120
5.3 Convergence Study for the Plate Carrying a Concentrated Load at the Center	122
5.4 Load-Displacement Curve	124
5.5 Comparison of Radial Displacements for the Center Deflection to the Plate Thickness Ratio Equal to 0.5	126

5.6	Comparison of Radial Displacements for the Center Deflection to the Plate Thickness Ratio Equal to 2.0	127
6.1	Experimental Set Up	135
6.2	Loading on the Specimen	136
6.3	Static Loading on the Quasi-Isotropic Circular Laminates	137
6.4	Axisymmetric Validation for Quasi-Isotropic 8-Ply T300/5208 Laminate	140
6.5	Deflected Shapes w for the Laminate Under Quasi-Static Point Loads for $\frac{O}{h} = 0.5$ and 1.0	141
6.6	Deflected Shapes w for the Laminate Under Quasi-Static Point Loads for $\frac{O}{h} = 1.5$ and 2.0	142
6.7	Load-Deflection Curve Comparison	143
7.1	Back Face Spalling in a Composite Plate	147
7.2	Three Modes of Fracture	148
7.3	Cracked Plate	149
7.4	Load-Displacement Curve	151
7.5	Delaminations in Center Strip	155
7.6	Variation of Strain Energy Release Rates with Delamination Length for a Plate Radius of 25.4 mm	162
7.7	Variation of Strain Energy Release Rates with Delamination Length for a Plate Radius of 38.1 mm	163
A-1	Graphical Representation of the Newton-Raphson Method	180

LIST OF SYMBOLS

a	Radius of the plate/membrane
[A]	Extensional stiffness matrix
b	Width of the center strip
[B]	Coupling stiffness matrix
d_0	Delamination length
[D]	Bending stiffness matrix
D_{eq}	Equivalent bending stiffness
E	Young's modulus
E_{eq}	Equivalent Young's modulus
E_{11}	Lamina Young's modulus in fiber direction
E_{22}	Lamina Young's modulus perpendicular to the fiber direction
F	Nodal load vector
G	Strain energy release rate
G_c	Critical strain energy release rate
G_I	Strain energy release rate in the opening mode
$(G_I)_c$	Critical strain energy release rate in the opening mode
h	Thickness of the plate/membrane
[H]	Constitutive relations matrix
$[k]_e$	Total stiffness matrix of the element
$[k_L]_e$	Linear bending stiffness matrix of the element
$[k_{NL}]_e$	Nonlinear bending stiffness matrix of the element
[K]	Global stiffness matrix of the element
m	Number of regions

M	Moments
n	Number of elements
N_r, N_θ	Radial and tangential tension force
p	Pressure
P	Point load
Q_r, Q_θ	Radial and tangential shearing forces
r, θ , z	Cylindrical coordinate system
Δr	Elemental length
t	Thickness of the ply
u	Radial displacement
\bar{u}	Normalized radial displacement
U	Strain energy
U_b	Strain energy due to bending
U_m	Strain energy due to stretching
w	Transverse displacements
\bar{w}	Normalized transverse displacements
w_0	Transverse displacement at the center of the plate
x, y, z	Rectangular coordinate system
$\epsilon_r, \epsilon_\theta$	Radial and tangential strain
σ_r, σ_θ	Radial and tangential stress
$\bar{\sigma}_r, \bar{\sigma}_\theta$	Normalized radial and tangential stress
σ_z	Normal stress
κ	Curvatures
v	Poisson's ratio
v_{eq}	Equivalent Poisson's ratio

Chapter 1

INTRODUCTION

1.1 Motivation

Composite materials are being used increasingly in aircraft structures due to their high specific strength and stiffnesses, and the resultant weight savings. Traditionally, use of graphite fiber composites have been confined to secondary structures. However, requirements for reduced structural weight, improved aircraft performance, and efficiency are making composite materials increasingly competitive for expanded usage in primary, load carrying structures. In comparison to conventional metals, an understanding of the complex behavior of composites is still in its preliminary stage, and applications are based on knowledge gained through extensive experimental programs. Past experiences and experiments have confirmed that graphite fiber composite laminates have very low ultimate strains, no plastic deformation range, and no usable strength in the thickness direction. These limitations are very obvious when laminates are subjected to impact loads. Therefore the study of impact damage susceptibility of these composite laminates is increasingly important.

Resin matrix composites are basically brittle materials, and the damage caused by impact differs from the damage on ductile metal structures. The ductile metals tend to develop indentations which are normally visible. On the other hand brittle materials like composites

tend to have both visible and invisible damage. Such damage is usually in the form of delaminations, matrix cracks and possible broken fibers. It can cause significant strength losses in composite materials [1-7].* The potential severity of visible and invisible damage has instigated numerous investigations into the impact behavior of composites.

Past studies [8-12] indicate that in thin composite laminates first level of visible damage occurs on the back face of the laminate and is called as "back face spalling." A typical back face spalled laminate is shown in Fig. 1.1. Elber [8] conducted a series of tests on circular composite plates. He identified the sequence in which damage occurs in thin 8 ply T300/5208 quasi-isotropic graphite/epoxy circular plates subjected to center point loads. He showed that, first visible damage occurs in the lowest ply (8th ply) in the form of a matrix cracking parallel to the fibers. Further increase in the load levels results into the two dominant cracks in the eighth ply and delaminations between plies 7 and 8 surrounds these two cracks. Additional increase in the load levels cause these delaminations and cracking to propagate unstably in the bottom ply in the fiber direction. This unstable growth of delaminations and propagation of the two dominant cracks result in the massive back face spalling action. During the back face spalling action, curved trajectory of the 8th ply center strip (formed by the two dominant cracks in the 8th ply) running under the load point in the fiber direction changes virtually to a straight line between the load

*The number in brackets indicate references.

ORIGINAL PAGE IS
OF POOR QUALITY

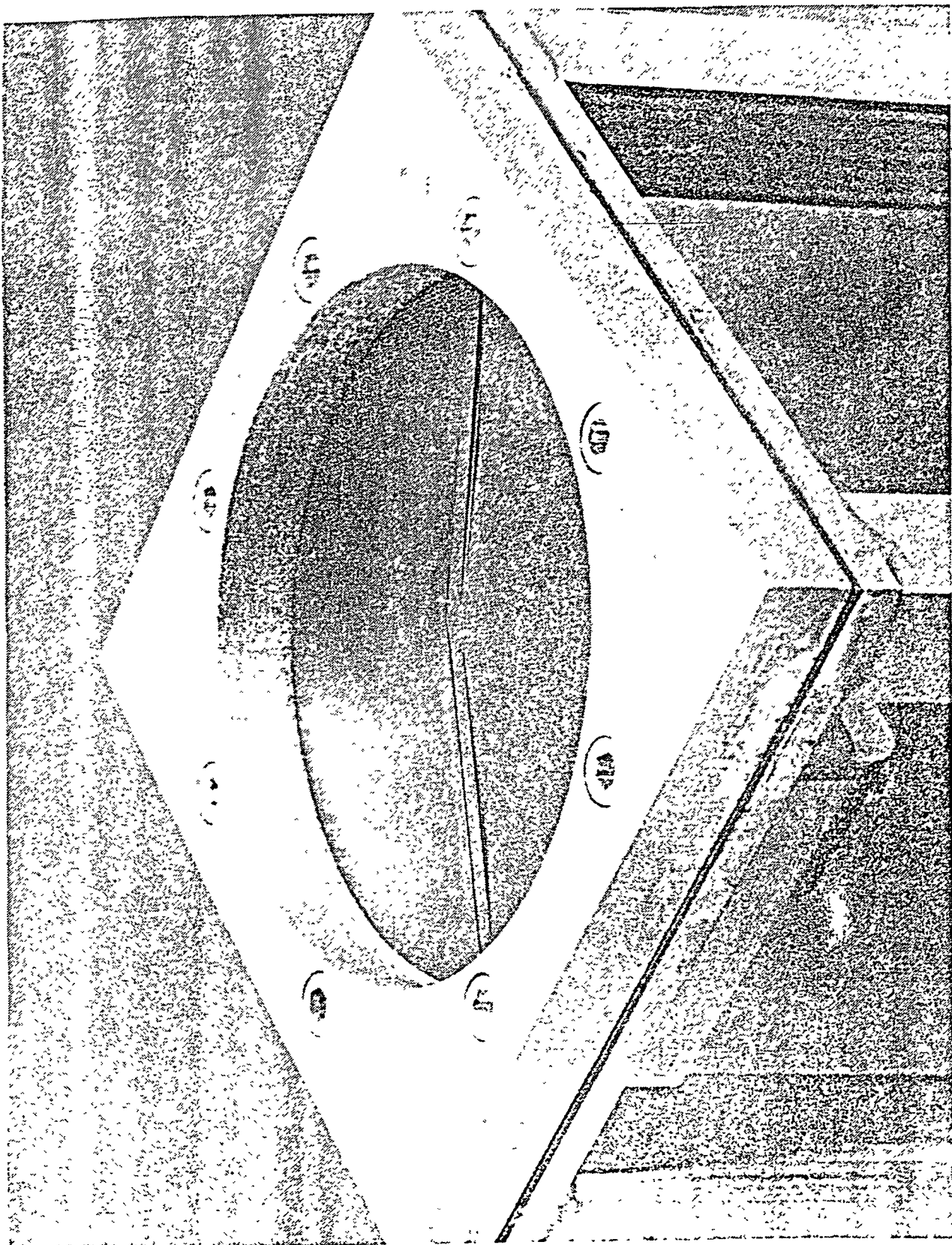


Fig. 1.1 Back Face Spalling in a Composite Plate

point and the support (Fig. 1.1). Several investigators [9-12] have also reported back face spalling damages in composite laminates under low velocity impact type point loads. While considerable experimental observations have been made on the back face spalling, a theoretical understanding of the deformation mechanics and the back face spalling phenomenon is not fully known. The present study was undertaken to develop analytical models, to understand the deformation mechanics, and to explain the back face spalling phenomenon, in thin composite laminates. These models will be particularly helpful to quantify the impact mechanics and to produce composites with improved resistance to the back face spalling and impact damage.

1.2 Scope and Objectives

Impact events are characterized into three velocity domains:

1. High velocity or ballistic impact where the velocity, $v > 600$ m/sec.
2. Intermediate velocity impact ($30 \text{ m/sec} < v < 600 \text{ m/sec}$), such as foreign object damage (F.O.D.) impact on turbine fan blades, ground debris thrown up by wheels, etc.
3. Low velocity impacts ($v < 30 \text{ m/sec}$) are represented by handling damage such as dropping tools, foot steps and similar events.

In this study, the effect of low velocity impact on composites is addressed. Many low velocity impact situations that an aircraft component is exposed to include: dropped tools, runway stones, tire blow out debris, ground collisions, etc. Due to low velocity impact,

composite laminates suffer both visible and invisible damage. To improve the material performance in impact requires a better understanding of the deformation and damage mechanics under low velocity type impact loading. Therefore, the specific objectives of this study are:

1. To develop an analytical model to understand the deformation mechanics in thin composite laminates under low velocity type impact loading.
2. To develop an analytical model to explain the back face spalling phenomenon in thin composite laminates under low velocity type impact loading.
3. To verify these analytical models by conducting experiments on thin composite laminates.

For both the analytical and the experimental purpose quasi-isotropic laminates of T300/5208 graphite/epoxy material with stacking sequence of $[45/0/-45/90]_S$ are considered in this study.

1.3 Review of Earlier Work

The subject of impact related phenomena has been studied by many investigators utilizing many different approaches. Some of this work has been related to ballistic type impact, and hence, is not applicable here. The past studies indicate that considerable experimental investigations have been made to understand the low velocity impact problem in composite laminates. Literature review also indicates that theoretical investigations of the low velocity impact in composites are limited.

1.3.1 Experimental Studies

McQuillen and Gause [13] first studied the response of composite structural elements to low speed, transverse impact. They conducted series of experiments on graphite/epoxy composite laminates 76 mm wide, with a span 152 mm and with thickness of 2.13 mm. The laminates had ($\pm 45/0_2/\mp 45$)_s stacking sequences and were simply supported on two edges. McQuillen and Gause concluded that inplane stress wave effects in the low velocity regime are negligible. They observed that the dynamic failure mechanism is identical to the static failure mechanism. Rhodes et al. [12] investigated the effect of low velocity impact damage on the compressive strength of graphite/epoxy panels. They concluded that the compressive strength of graphite-epoxy components can be reduced significantly by the effects of low velocity impact damage. Similar observations were made by Gause and Huang [14]. They observed significant reduction in the static strength of graphite/epoxy panels, when panels were subjected to low velocity impact loads. They examined the damage mechanisms in graphite/epoxy panels under dynamic and static loading. They concluded that in graphite/epoxy panels the static and dynamic damage mechanisms are identical. Card and Rhodes [15] studied the effects of low velocity impact on the compressive strength of graphite/epoxy structures. They conducted extensive tests on sandwich beams, laminated plates and stiffened panels. They studied the damage patterns and suggested possible sequence for laminate damage due to low velocity impact and found that, there was no visible damage on the impact surface, however, the side opposite to impact surface suffered a visible damage in the form of back face spalling. Their observations were similar to the earlier observations made by

Cristescu et al. [16] with the 0-90° ply fiberglass/epoxy composite plates.

Gause [17] performed low speed, hard object impact on thick graphite/epoxy plates. He concluded that inplane wave effects are not important in low velocity impact on thick graphite/epoxy plates. He found that in thick composite plates the dominant damage mode is shear failure mode. He performed quasi-static tests on thick laminates and found that the damage mechanics in impact and quasi-static loading are identical. Gause et al. [18] studied the effect of low-velocity impact damage on the composite wing box. They identified that the first visible damage in composite skins occurs on the back surface (surface opposite to the impact point) in the form of spalling. Similar observations were made by Ramkumar [5], Bhatia [10], Hertzberg et al. [11].

1.3.2 Theoretical Studies

As pointed out earlier only a few theoretical investigations were made. Some of the earlier work is discussed here. A theoretical model to study the damage and deformation mechanics due to low velocity impact problem in composites was developed by Lloren [19]. He developed a theoretical model for a rectangular composite plate subjected to a quasi-static load equivalent to the impact load. Dobyns and Porter [20] and Dobyns [21] and Hayes and Rybicki [22] performed similar analysis for simply supported composite plates and Greszczuk [23] performed a quasi-static analysis for circular composite plates. However, all these analyses were based on the linear plate bending theory.

Recent studies by Bostaph and Elber [24], Elber [8], Lal [25] and Shivakumar et al. [26], have shown that the laminates undergo large

deformation when the impact occurs at low velocity. Hence, it is necessary to develop a more general analysis that includes large deflection effects. These types of analyses will help to predict accurately the deformations and failures in composite plates subjected to low velocity type impact loading.

Bostaph and Elber [24] performed quasi-static impact tests on thin composite laminates. They used superposition approach to match the plate bending solution and a membrane solution under the load points. By using this superposition approach they obtained load-deflection behavior of circular composite plates undergoing large deformations. Shivakumar et al. [26] analyzed the impact damage problem using the Ritz technique and the large deformation theory for the circular thin quasi-isotropic laminates. The classical solution method used by Shivakumar et al. [26], Timoshenko [27], Washizu [28], to obtain the large deformation solutions of thin plates under the point loads is based on the Ritz technique, and only represents a membrane correction to the plate stiffness. Further the classical solution assumes that the functional form of the deformed shape of the plate is identical to the functional form of the deformed shape of the plate determined by the small deflection solution. The functional form of the deformed shape of the plate, however, is not identical for different load levels. Because at higher load levels the plate undergoes large deformations and the external load is partly equilibrated by the membrane action, the deformed shape of the plate can not be identical at all load levels.

Accurate prediction of the deformed shapes are necessary to obtain accurate stresses in the plate. The plate analysis based on the classical solution, which assumes the functional form of the deformed

shape to be identical for all load levels, would incorrectly predict the stresses. One of the objectives, therefore, was to develop simple analytical models to predict the accurate large deformation shapes of thin circular laminates under quasi-static point loads. To obtain accurate large deformation shapes of these thin circular laminates, a finite difference and a finite element model is proposed in this thesis. As discussed earlier, several investigators have shown that the damages in thin composite laminates due to low velocity impact loads are similar to the damages due to equivalent quasi-static loads, therefore in both the models proposed here, low velocity impact loads are replaced by equivalent quasi-static loads. These models are briefly discussed in the following section.

1.4 Proposed Methods of Analyses

In the present work an attempt was made to obtain simple analytical models for the large deflection analysis of thin circular quasi-isotropic laminates under the quasi-static point loads. The first model proposed here is a plate-membrane coupling model. This model does not have the constraining assumption that the deformed shape of the plate should be identical to the deformed shape of the plate determined by the small deflection plate solution. The plate-membrane coupling model proposed here assumes that the effect of flexural anisotropy of the axially quasi-isotropic laminates is small and the plate behaves flexurally isotropic.

1.4.1 Plate-Membrane Coupling Model

A thin plate undergoing large deformations can be decomposed into two problems. First, a plate with shear and flexural stiffnesses but no

mid-plane extensional stiffness. Second, a plate with extensional stiffness, but no shear and flexural stiffnesses (membrane). Solutions of these two problems when coupled together will yield complete knowledge of displacements in quasi-isotropic laminates undergoing large deformations.

Solution of the first problem is the well known small deflection plate analysis [27]. The second problem which is the analysis of circular membrane subjected to axisymmetric loading is more complex in nature, as it involves geometrical nonlinearity. The problem of circular membrane subjected to surface and edge loads has been studied by many investigators. Hencky [29], Dickey [30], and Shaw and Perrone [31] determined the deflections of a uniformly loaded membrane. Goldberg and Pifko [32] and Weinitzschke [33,34] employed power series approaches to obtain the solutions of annular membranes. In addition to power series method Weinitzschke [33,34] presented an integral equation approach to the solution of annular membranes subjected to surface and edge loads. Callegari and Reiss [35] studied the axisymmetric deformations of circular membranes subjected to uniform normal pressure by using the shooting method. The literature review indicates that limited numerical solutions are available for the nonlinear membrane problems. Furthermore these solutions are limited to the circular membranes subjected to uniform load.

In the present work a more general formulation for the analysis of circular isotropic membranes subjected to arbitrary axisymmetric loading is presented. In this formulation a single nonlinear governing equation in terms of radial stress is used. The nonlinear governing differential equation is replaced by a set of nonlinear algebraic equations using

finite difference technique. These nonlinear algebraic equations are numerically solved to obtain stresses and displacements.

By using the small deflection plate solution and the large deformation membrane solution in conjunction with the plate-membrane coupling model, the large deformation solution of the clamped circular quasi-isotropic plate subjected to quasi-static center point load is obtained.

The plate-membrane coupling model uses a finite difference technique. A second analytical model is proposed in this work, to obtain the large deformation solutions of circular laminates uses a finite element method. The finite element formulation presented here is based on an appropriate linearization of strain displacement relations and uses an iterative method of solution. The formulation includes the effects of geometric nonlinearity.

To study the geometric nonlinear problems many investigators [36-44], used the energy approach, in which the nonlinear strain displacement relation is linearized by equivalent linearization technique. However, earlier investigators have ignored the effects of inplane displacements in the formulation. This discrepancy was pointed out by Prathap and Vardan [45], Sarma and Vardan [46], Prathap and Bashyam [47], and Prathap [48]. However, so far no attempt has been made to include the inplane displacements in the finite element formulation of the circular plate subjected to a center point load and undergoing the large deformations.

The reason for ignoring the effects of mid-plane displacements by earlier investigators may have been due to complexity of the nonlinear

finite element formulation. In the present finite element formulation the discrepancy of ignoring inplane displacements is removed and a complete finite element formulation which includes inplane displacements is presented. The large deformation solutions of clamped circular plates subjected to central point loads obtained by using the plate-membrane coupling model, and the finite element model, are compared. Experimental verification of the plate-membrane coupling model and the finite element model is also presented.

The second objective of this research is to develop a theoretical model to study the back face spalling phenomenon in thin composite laminates under low-velocity impact type point loads. Elber [8] conducted series of tests on thin eight ply T300/5208 quasi-isotropic graphite/epoxy laminates. He showed that the damage mode, in actual impact tests at velocities around 5 m/s, was very similar to the damage made in the static tests. He postulated that the massive back face spalling which often is the first visible sign of damage in laminates is related to the low peel-mode fracture toughness in brittle resins and that it is trackable by static analysis. In the present work, this phenomenon of the back face spalling is explained by developing a simple analytical model based on the quasi-static analysis. The model uses the large deformation shapes of the circular laminates in conjunction with the fracture mechanics principles. This model is verified by conducting the back face spalling experiments on thin composite laminates.

1.5 Layout of Presentation

In Chap. 1, the problem of low velocity impact in graphite/epoxy composites is discussed. The phenomenological aspects of the problem,

such as the large deformation behavior, the back face spalling etc. are introduced. The relevant literature on the study of the low velocity impact problem emphasizing the deformation mechanics and the back face spalling phenomenon, is reviewed. Against this background the present methods of analyses to study the deformation mechanics and the back face spalling phenomenon in thin composite laminates under quasi-static point loads are proposed.

Chapter 2 presents a small deflection plate analysis for a clamped circular quasi-isotropic plate. A method for modeling flexurally anisotropic quasi-isotropic plate as an isotropic plate having the flexural stiffness components equivalent to the flexural stiffness components of the quasi-isotropic plate is presented. A finite difference method for computing displacements is described. The numerical results for the plate deformations, obtained by using the finite difference method are compared with the exact solution.

In Chap. 3, a general analysis of circular isotropic membranes with clamped peripheral edges, subjected to arbitrary axiymmetric loading is presented. A single governing equation in terms of radial stress is derived. The solution of this nonlinear governing equation is presented by using the finite difference method in conjunction with Newton-Raphson method.

Chapter 4 presents the plate-membrane coupling model to study the large deformation behavior of clamped circular plates. The model uses the plate solution (Chap. 2) and the membrane solution (Chap. 3), in conjunction with a coupling principle. The numerical results obtained by using the plate-membrane coupling model for clamped circular

laminates undergoing the large deformations are presented. These numerical results are compared with the classical solution.

In Chap. 5, a finite element model which uses appropriate linearization of strain-displacement relations is presented. The model is based on a variational technique and uses the principle of minimum potential energy. The finite element model is then used to obtain the large deformation solution of clamped circular laminates subjected to central point loads. The solutions obtained by the finite element model and the plate-membrane coupling model are compared.

In Chap. 6, plate mechanics experiments are described. The experimentally obtained large deformation shapes and the load-deflection curves of thin quasi-isotropic clamped circular laminates are compared with those obtained by using the plate-membrane coupling model (Chap. 4) and the finite element model (Chap. 5).

Chapter 7 presents the back face spalling model. The back face spalling model is developed by using the large deformation shapes of thin circular laminates in conjunction with fracture mechanics principles. The analytical back face spalling model is verified by conducting back face spalling experiments on thin composite laminates. Several alternative approaches to reduce the back face spalling in composite plates are discussed.

Finally, in Chap. 8, a summary of the highlights of the present work and some possible directions for further study of low velocity impact in composites are presented.

Chapter 2

SMALL DEFLECTION PLATE ANALYSIS

2.1 Introduction

In Chap. 1, a plate-membrane coupling model was introduced to obtain the large deformation behavior of quasi-isotropic laminates. The plate-membrane coupling model requires a small deflection plate solution and a large deflection membrane solution. In this chapter the small deflection plate analysis for a clamped circular quasi-isotropic plate is presented. To develop a simple one dimensional analytical model, quasi-isotropic plate is modeled as an isotropic plate with the flexural stiffness components equivalent to the flexural stiffness components of the quasi-isotropic plate. A finite difference method for computing displacements is described. A study to establish the convergence characteristics of the finite difference method is then presented. The numerical results for the plate deformations, obtained by using the finite difference method are compared with the exact solution.

2.2 Plate Configuration

Figure 2.1 shows an axisymmetrically loaded clamped circular plate, with thickness h and radius a . The plate was a quasi-isotropic laminate of T300/5208 graphite/epoxy material with stacking sequence $[45/0/-45/90]_S$. The material properties of the laminate are given in Table 2.1.

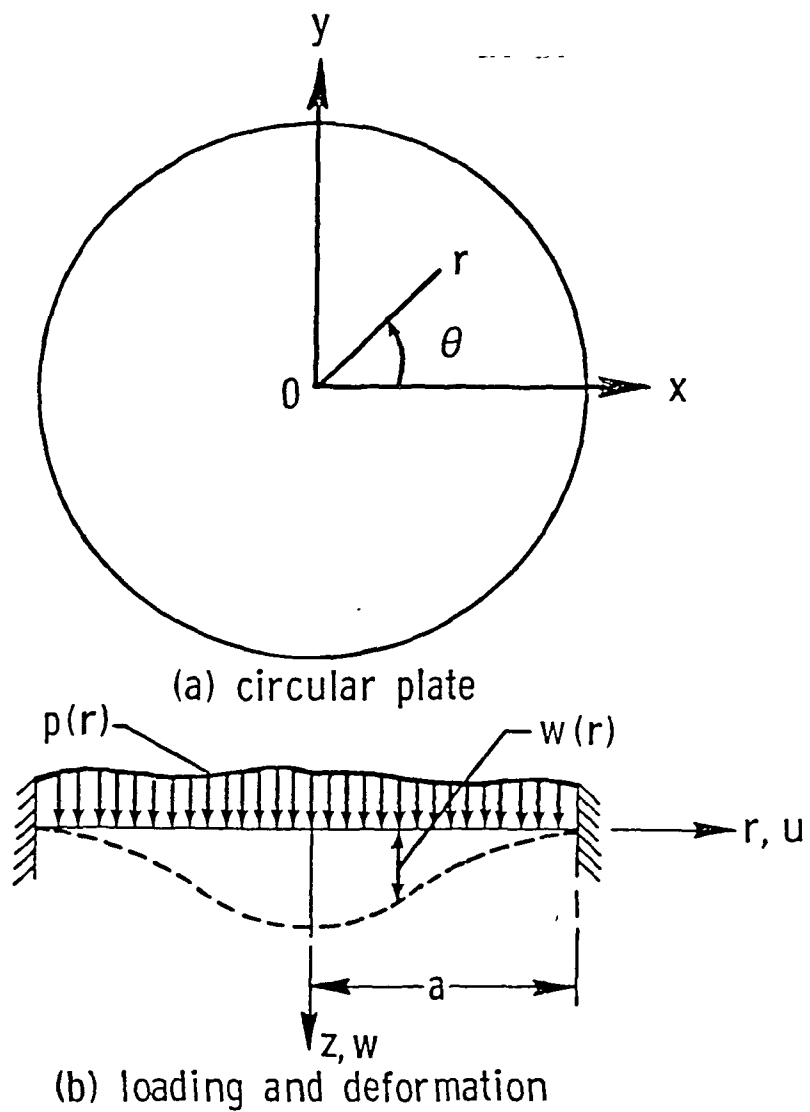


Fig. 2.1 Plate Configuration

2.3 Assumptions

The small deflection plate theory, generally attributed to Kirchhoff and Love [49], is used here with the following assumptions:

1. The plate is initially flat, i.e. the plate has no initial curvature.
2. The thickness of the plate is small compared to its other dimensions.
3. The deflections are small compared to the plated thickness.
(Maximum deflection-to-plate thickness ratios of 1/15 to 1/10 are considered small)
4. The slopes of the deflected middle surface are small compared to unity. (This follows from the assumption 3 above)
5. The deformations are such that, straight lines initially normal to the middle surface, remain straight and normal to the middle surface. (i.e. transverse shear strains are not permitted)
6. The material has the same elastic modulus in tension and in compression.
7. The component of stress normal to the midsurface, σ_z , is negligible
8. The strains in the middle surface, produced by inplane forces, are neglected.
9. The plate is assumed to be flexurally isotropic, even through a quasi-isotropic plate is anisotropic in flexure.

2.4 The Governing Differential Equation

In this section the governing differential equation for axisymmetrical bending of a clamped circular plate subjected to arbitrary axisymmetric loading and undergoing small deformation is presented.

Figure 2.2 shows an infinitesimal element abcd cut out from the plate by two cylindrical sections ab and cd and by two radial sections ad and bc. Consider the equilibrium of an element abcd. The couple acting on the side cd of the element is

$$M_r r d\theta \quad (2.1)$$

where M_r is the radial moment per unit length. The corresponding couple on the side ab is

$$(M_r + \frac{dM_r}{dr} dr) (r + dr) d\theta \quad (2.2)$$

Couples on the sides ad and bc of the element are each $M_\theta dr$ where M_θ is the tangential moment per unit length. The components of these couples in plane rz are each $M_\theta dr \sin(\frac{d\theta}{2})$ and for small $d\theta$, $\sin(\frac{d\theta}{2}) = \frac{d\theta}{2}$. Therefore, these couples give a resultant couple in the plane rz equal to

$$M_\theta dr d\theta \quad (2.3)$$

Denoting $Q(r)$ as the shearing force per unit length of the cylindrical section of radius r , the total shearing force acting on the side cd of the element is $Q(r) r d\theta$, and the corresponding force on the side ab is $[Q(r) + \frac{dQ(r)}{dr} dr] (r + dr) d\theta$, these forces give a couple in the rz plane equal to

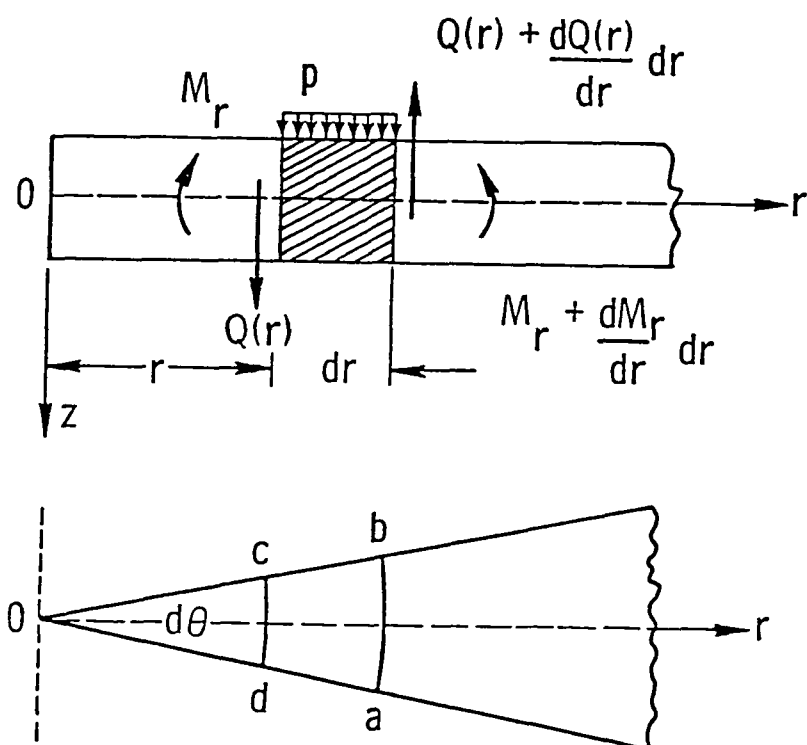


Fig. 2.2 Equilibrium of the Plate Element

$$Q(r) r d\theta \frac{dr}{2} + \left(Q(r) + \frac{dQ(r)}{dr} \right) (r + dr) d\theta \frac{dr}{2} \quad (2.4)$$

Neglecting the third and higher order terms in Eq. (2.4) the resultant couple in the rz plane equal to

$$Q(r) r d\theta dr \quad (2.5)$$

Summing up the moments, the equation of equilibrium of the element abcd:

$$(M_r + \frac{dM_r}{dr} dr) (r+dr) d\theta - M_r r d\theta - M_\theta dr d\theta + Q(r) r d\theta dr = 0 \quad (2.6)$$

neglecting the third and higher order terms, one has,

$$M_r + \frac{dM_r}{dr} r - M_\theta + Q(r) r = 0 \quad (2.7)$$

Relations between curvatures and moments for pure bending, in cylindrical co-ordinate system are given by [27],

$$M_r = -D \left[\frac{d^2 w}{dr^2} + \frac{\nu}{r} \frac{dw}{dr} \right] \quad (2.8)$$

$$M_\theta = -D \left[\frac{1}{r} \frac{dw}{dr} + \nu \frac{d^2 w}{dr^2} \right] \quad (2.9)$$

where D is a flexural modulus of the isotropic plate and is given by

$$D = \frac{Eh^3}{12(1-\nu^2)} \quad (2.10)$$

where E is the Young's Modulus and ν is the Poisson's ratio of the isotropic plate.

Substituting Eqs. (2.8) and (2.9) into Eq. (2.7), the governing differential equation for the circular plate subjected to axisymmetric loading is

$$\frac{d^3 w}{dr^3} + \frac{1}{r} \frac{d^2 w}{dr^2} - \frac{1}{r^2} \frac{dw}{dr} = \frac{Q(r)}{D} \quad (2.11)$$

Equation (2.11) is a governing differential equation for the circular isotropic plate with the flexural modulus D and subjected to arbitrary axisymmetric loading. Denoting D_{eq} as a flexural modulus of the quasi-isotropic circular plate the governing differential Eq. (2.11) for the quasi-isotropic circular plate was written as:

$$\frac{d^3 w}{dr^3} + \frac{1}{r} \frac{d^2 w}{dr^2} - \frac{1}{r^2} \frac{dw}{dr} = \frac{Q(r)}{D_{eq}} \quad (2.12)$$

where $Q(r)$ is a shear force per unit length at any radius r and can be obtained as (Fig. 2.3)

$$2 \pi r Q(r) = \int_0^r 2 \pi \xi p(\xi) d\xi \quad (2.13)$$

where $p(\xi)$ is the intensity of loading at any radius ξ . D_{eq} in Eq. (2.12), is an equivalent flexural modulus for the quasi-isotropic laminate. The equivalent modulus D_{eq} , can be obtained by equating bending energy of the quasi-isotropic laminate and an equivalent isotropic plate. A detail derivation to determine the equivalent flexural modulus D_{eq} , is presented in the next section.

2.5 Derivation of the Equivalent Flexural Modulus D_{eq}

Laminate extensional, coupling, and bending stiffnesses were calculated by using classical laminate plate theory [50] for a $[45/0/-45/90]_S$ quasi-isotropic laminate with elastic properties given in Table 2.1. The extensional stiffness is independent of the polar angle θ (see Fig. 2.1) and is constant over the entire plate domain. This indicates that the laminate behaves perfectly isotropic for membrane and

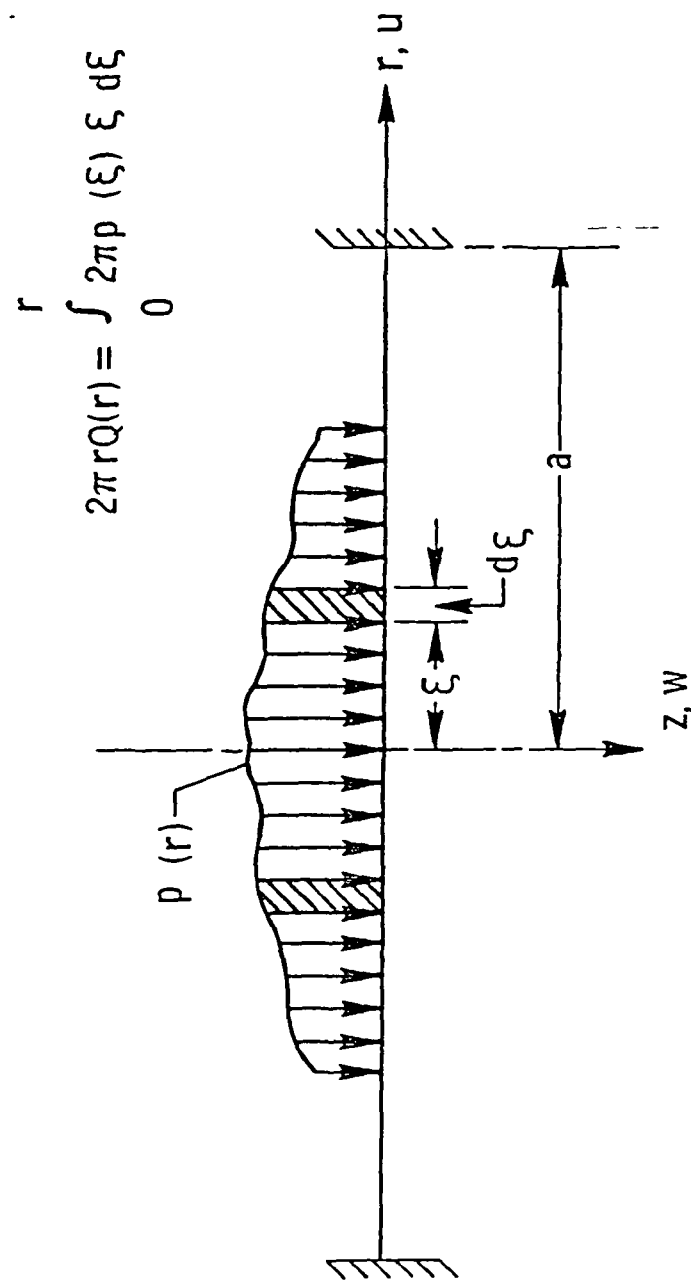


Fig. 2.3 Arbitrary Axisymmetrically Loaded Circular Plate

inplane loadings.

Since the laminate is symmetric, the coefficients of the coupling stiffness are found to be zero. The laminate bending stiffness depends on θ . However, an equivalent bending stiffness which is independent of θ can be determined by equating the flexural strain energies of the clamped circular quasi-isotropic laminate and an equivalent circular isotropic plate.

For a circular quasi-isotropic laminate the total strain energy in bending is

$$U_b = \frac{1}{2} \int_0^{2\pi} \int_0^a \{M\}^T \{\kappa\} r dr d\theta \quad (2.14)$$

where

$$\{M\} = \begin{Bmatrix} M_r \\ M_\theta \\ M_{r\theta} \end{Bmatrix} \quad \text{and} \quad \{\kappa\} = \begin{Bmatrix} \kappa_r \\ \kappa_\theta \\ \kappa_{r\theta} \end{Bmatrix}$$

M_r , M_θ , and $M_{r\theta}$ are moments and κ_r , κ_θ , and $\kappa_{r\theta}$ are the corresponding curvatures. For the quasi-isotropic laminate the moments and curvatures are related as

$$\{M\} = [D] \{\kappa\} \quad (2.15)$$

where

$$[D] = \begin{bmatrix} D_{11} & D_{12} & D_{16} \\ D_{21} & D_{22} & D_{26} \\ D_{61} & D_{62} & D_{66} \end{bmatrix} \quad (2.16)$$

substitution of Eq. (2.15) into Eq. (2.14) yields,

$$U_b = \frac{1}{2} \int_0^{2\pi} \int_0^a \{\kappa\}^T [D] \{\kappa\} r dr d\theta \quad (2.17)$$

Equation (2.17) can be expanded as

$$\begin{aligned} U_b = & \frac{1}{2} \int_0^{2\pi} \int_0^a [\kappa_r^2 D_{11} + 2 \kappa_r \kappa_\theta D_{12} + 2 \kappa_r \kappa_\theta D_{16} \\ & + 2 \kappa_r \kappa_\theta D_{26} + \kappa_\theta^2 D_{22} \\ & + \kappa_{r\theta}^2 D_{66}] r dr d\theta \end{aligned} \quad (2.18)$$

The coefficients D_{11} , D_{12} , D_{16} , D_{26} , and D_{66} in the Eq. (2.18) are all known functions of θ [50]. Assuming that the curvatures are functions of r alone, then the integration over θ in Eq. (2.18) can be carried out and Eq. (2.18) can be written as

$$\begin{aligned} U_b = & \frac{2\pi}{2} \int_0^a [\kappa_r^2 D_{11}^1 + 2 \kappa_r \kappa_\theta D_{12}^1 + 2 \kappa_r \kappa_\theta D_{16}^1 \\ & + 2 \kappa_r \kappa_\theta D_{26}^1 + \kappa_\theta^2 D_{22}^1 \\ & + \kappa_{r\theta}^2 D_{66}^1] r dr \end{aligned} \quad (2.19)$$

where

$$D_{ij}^1 = \frac{1}{2\pi} \int_0^{2\pi} D_{ij} d\theta; i, j = 1, 2, \text{ and } 6$$

The bending energy of an isotropic plate with a flexural modulus D_{eq} , a Poisson's ratio of ν_{eq} and curvatures, κ_r , κ_θ , and $\kappa_{r\theta}$ (same as that of the quasi-isotropic laminates) can be written as

$$U_b (\text{isotropic plate}) = \frac{1}{2} \int_0^a \int_0^{2\pi} [\kappa_r^2 D_{eq} + 2 \kappa_r \kappa_\theta \nu_{eq} D_{eq}] r dr d\theta$$

$$+ \kappa_r^2 D_{eq} + \kappa_{r\theta}^2 \left(\frac{1-v_{eq}}{2}\right) D_{eq}] r dr d\theta \quad (2.20)$$

The flexural modulus D_{eq} and the Poisson's ratio v_{eq} are independent of θ . Hence integrations on θ can be carried out and Eq. (2.20) can be written as,

$$U_b \text{ (isotropic plate)} = \frac{2\pi}{2} \int_0^a [\kappa_r^2 D_{eq} + 2 \kappa_r \kappa_\theta v_{eq} D_{eq} \\ + \kappa_\theta^2 D_{eq} + \kappa_{r\theta}^2 \left(\frac{1-v_{eq}}{2}\right) D_{eq}] r dr \quad (2.21)$$

For the same arbitrary curvatures, κ_r , κ_θ , and $\kappa_{r\theta}$ on the composite laminate and the isotropic plate, the bending strain energies must be the same because of the assumed energy equivalence. Hence comparing curvature coefficient of Eqs. (2.19) and (2.21) equivalent bending stiffness D_{eq} and v_{eq} Poisson's ratio can be determined as,

$$D_{eq} = \frac{1}{2\pi} \int_0^{2\pi} D_{11} d\theta \quad (2.22)$$

$$v_{eq} D_{eq} = \frac{1}{2\pi} \int_0^{2\pi} D_{12} d\theta \quad (2.23)$$

$$D_{eq} = \frac{1}{2\pi} \int_0^{2\pi} D_{22} d\theta \quad (2.24)$$

$$\left(\frac{1-v_{eq}}{2}\right) D_{eq} = \frac{1}{2\pi} \int_0^{2\pi} D_{66} d\theta \quad (2.25)$$

If circular quasi-isotropic laminates were flexurally isotropic, then integrals

$$\frac{1}{2\pi} \int_0^{2\pi} D_{16} d\theta \text{ and } \frac{1}{2\pi} \int_0^{2\pi} D_{26} d\theta \quad (2.26)$$

would be equal to zero. However, in the circular quasi-isotropic laminate under consideration, integrals represented by Eq. (2.26) were nonzero. However, for the material properties presented in Table 2.1, integrals were found to be about 2.5 percent of $\frac{1}{2\pi} \int_0^{2\pi} D_{11} d\theta$ and hence neglected in this analysis.

Equations (2.22) through (2.25) represent four equations, with two unknowns, D_{eq} and v_{eq} . The first two equations, Eqs. (2.22) and (2.23), are sufficient to evaluate the two unknowns D_{eq} and v_{eq} . The third equation, Eq. (2.24), is essentially the same as Eq. (2.22) because of symmetries. For the material properties in Table 2.1, the value of D_{eq} and v_{eq} were found to be 5.688 N-m, and 0.31, respectively. These values of D_{eq} and v_{eq} , when substituted into the last equation, Eq. (2.25), satisfied the equation exactly.

For those ply properties mentioned in Table 2.1, the value of equivalent Young's modulus E_{eq} was obtained from an equivalent flexural modulus D_{eq} as

$$E_{eq} = \frac{D_{eq} \cdot 12 \cdot (1-v_{eq}^2)}{h^3} \quad (2.27)$$

and was found to be 53.3 GPa. This value of E_{eq} is exactly the same as the inplane Young's modulus of the laminate obtained by using the ply properties in Table 2.1 and the classical laminate theory.

2.6 Solution Method

The solution of the clamped circular plate problem via the

classical method [27], is limited to relatively simple plate load conditions. In simple loading cases shear force $Q(r)$ can be directly expressed as a function of r and since the governing equation, Eq. 2.12 is Euler equation, it can be solved to obtain a closed form solution for the transverse displacement w . However, if loading conditions are more complex, the analysis becomes increasingly tedious. In such cases numerical methods are used to obtain the solution of the problem. Among the numerical techniques presently available, the finite difference method and the finite element method are most commonly used. In the present analysis the finite difference method is used. The solution of the plate problem using the finite element method is described later in Chap. 5. In the finite difference method, the derivatives in the governing differential equation are replaced by difference quantities at selected points, called nodes. The details of the finite difference method are as follows:

The basic finite difference expressions follow logically from the fundamental rules of calculus [51]. For a continuous function $w = f(r)$ (Fig. 2.4), the first, second and third derivatives of the displacement at any node n can be written by using the central difference method [52] as:

$$\frac{dw}{dr}(n) = \frac{w(n+1) - w(n-1)}{2 \cdot \Delta r} \quad (2.28)$$

$$\frac{d^2w}{dr^2}(n) = \frac{w(n+1) - 2w(n) + w(n-1)}{(\Delta r)^2} \quad (2.29)$$

$$\frac{d^3w}{dr^3}(n) = \frac{w(n+2) - 2w(n+1) + 2w(n-1) - w(n-2)}{2 \cdot (\Delta r)^3} \quad (2.30)$$

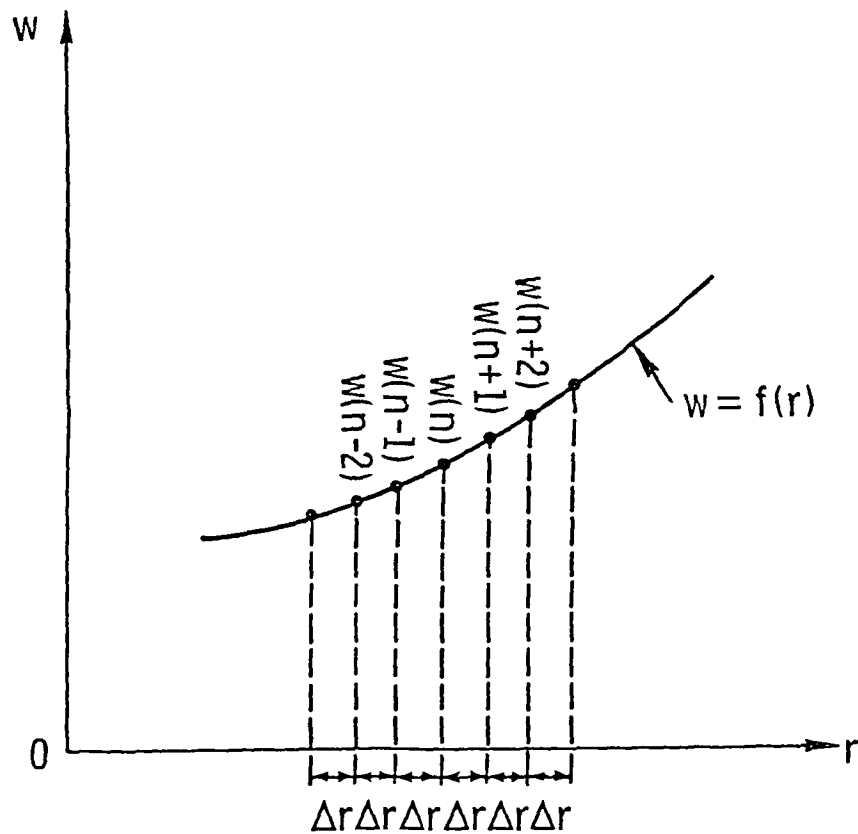


Fig. 2.4 Finite Differences for a Continuous Function $w = f(r)$

The governing differential equation is then transformed to an algebraic equation, by substituting the appropriate finite difference expressions. The solution of the differential equation thus reduces to the simultaneous solution of a set of linear, algebraic equations, written for every nodal point.

2.6.1 Application of the Finite Difference Method for the Solution of Arbitrarily Loaded Clamped Circular Plate

To solve the governing Eq. (2.12), the solution domain was discretized into m regions and $(m + 1)$ nodes. Denoting $w(n)$, $\frac{dw}{dr}(n)$, $\frac{d^2w}{dr^2}(n)$, and $\frac{d^3w}{dr^3}(n)$ as the first, second, and third derivatives of the displacement at the n node, the governing Eq. (2.12) was written as, at any node n :

$$\begin{aligned} \frac{d^2w}{dr^3}(n) + \frac{1}{r_n} \frac{d^2w}{dr^2}(n) - \frac{1}{r_n^2} \frac{dw}{dr}(n) \\ = \int_0^{r_n} \frac{p(\xi) \xi d\xi}{D_{eq}} \end{aligned} \quad (2.31)$$

First, second, and third derivatives of the transverse displacement w from the governing Eq. (2.31), were replaced by finite difference quantities given by Eqs. (2.28), (2.29), and (2.30).

To simplify the evaluation of the integral in the above equation the following assumption was made. Consider an i^{th} region with $r_{i-1} < r < r_i$. Although the applied load varies within the region $r_{i-1} < r < r_i$, the load will be assumed to be uniform in this region with a value p_i . The magnitude of p_i is assumed to be equal to the value of the load at the mid-point of this region, i.e., at $r = (r_i +$

$r_{i-1})/2$. As the number of regions in the model become large, the size of each region decreases and hence the variation of the load within each region becomes insignificant. With this assumption the governing Eq. (2.31), reduces to

$$\frac{d^3 w}{dr^3} (n) + \frac{1}{r_n} \frac{d^2 w}{dr^2} (n) - \frac{1}{r_n^2} \frac{dw}{dr} (n) = \frac{\sum_{i=1}^n p_i (r_i^2 - r_{i-1}^2)}{2 r_n D_{eq}} \quad (2.32)$$

2.6.2 Boundary Conditions

For the circular plate with axisymmetric loading the boundary conditions were

- (a) Both the transverse displacement w and the slope dw/dr equal zero at the clamped edge ($r = a$).
- (b) The slope dw/dr equal zero at the center ($r = 0$).

Using the governing Eq. (2.32) in the form of finite difference quantities at each node and transforming the above boundary conditions into finite difference quantities, a set of simultaneous algebraic equations were obtained. This set contained number of unknowns that are equal to number of nodes in the solution domain. These algebraic equations were solved simultaneously, to obtain the transverse displacement at each node. To illustrate the method, a very simple 4 region idealization was chosen. The details of the method are presented in the following section, for this simple idealization.

2.7 Illustrative Example

Consider a clamped circular quasi-isotropic plate with radius a

and thickness h . The plate is subjected to a uniform loading over the region $0 < \frac{r}{a} < 0.5$. The objective is to obtain the plate displacements using the finite difference method.

2.7.1 Problem Formulation

The solution domain $0 < \frac{r}{a} < 1.0$ is discretized into 4 regions and 5 nodes (see Fig. 2.5). At the node 0, the boundary condition is slope $\frac{dw}{dr} = 0$. This conditions can be transformed into the finite difference form as follows:

By using Taylor's series expansion, the displacements at the nodes (1) and (2) can be written as

$$w(1) = w(0) + \frac{\Delta r}{1!} \frac{dw}{dr}(0) + \frac{\Delta r^2}{2!} \frac{d^2 w}{dr^2}(0) \dots \quad (2.33)$$

$$w(2) = w(0) + \frac{2\Delta r}{1!} \frac{dw}{dr}(0) + \frac{(2\Delta r)^2}{2!} \frac{d^2 w}{dr^2}(0) \quad (2.34)$$

From the Eqs. (2.33) and (2.34) by eliminating terms $\frac{d^2 w}{dr^2}(0)$ and using boundary condition, the slope $\frac{dw}{dr}$ equal zero at $r = 0$ or $\frac{dw}{dr}(0) = 0$, Eq. (2.34) is written as:

$$4 w(1) - w(2) - 3 w(0) = 0 \quad (2.35)$$

The governing differential equation at any node n for the quasi-isotropic plate is (Eq. (2.32))

$$\frac{d^3 w}{dr^3}(n) + \frac{1}{r_n} \frac{d^2 w}{dr^2}(n) - \frac{1}{r_n^2} \frac{dw}{dr}(n) = \sum_{i=1}^n \frac{p_i (r_i^2 - r_{i-1}^2)}{2 r_n D_{eq}}$$

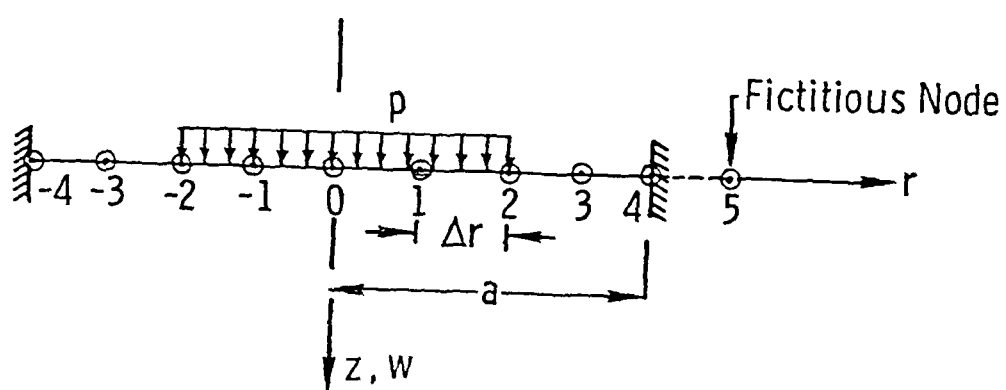


Fig. 2.5 Four Region Idealization for the Plate Uniformly Loaded Over the Region $0 \leq r/a \leq 0.5$

For the node no. 1 the first and second derivatives can be expressed in the finite difference form, by using central difference Eqs. (2.28) and (2.29) as:

$$\frac{dw}{dr} (1) = \frac{w(2) - w(0)}{2 \cdot \Delta r} \quad (2.36)$$

$$\frac{d^2 w}{dr^2} (1) = \frac{w(2) - 2 w(1) + w(0)}{(\Delta r)^2} \quad (2.37)$$

The third derivative i.e. $\frac{d^3 w}{dr^3} (1)$ can be obtained as follows:

By using Taylor's series expansion the displacements at the nodes (2) and (3) are written as

$$w(2) = w(1) + \frac{\Delta r}{1!} \frac{dw}{dr} (1) + \frac{\Delta r^2}{2!} \frac{d^2 w}{dr^2} (1) + \frac{\Delta r^3}{3!} \frac{d^3 w}{dr^3} (1) \quad (2.38)$$

$$w(3) = w(1) + \frac{2\Delta r}{1!} \frac{dw}{dr} (1) + \frac{(2\Delta r)^2}{2!} \frac{d^2 w}{dr^2} (1) + \frac{(2\Delta r)^3}{3!} \frac{d^3 w}{dr^3} (1) \quad (2.39)$$

Eliminating $\frac{dw}{dr} (1)$ from the Eqs. (2.38) and (2.39) the following equation is obtained

$$2 w(2) - w(3) = w(1) - (\Delta r)^2 \frac{d^2 w}{dr^2} (1) - (\Delta r)^3 \frac{d^3 w}{dr^3} (1) \quad (2.40)$$

But from the Eq. (2.37)

$$\frac{d^2 w}{dr^2} (1) = \frac{w(2) - 2 w(1) + w(0)}{(\Delta r)^2}$$

Substituting Eq. (2.37) into Eq. (2.40), equation for $\frac{d^3 w}{dr^3}(1)$ is obtained as follows:

$$\frac{-3w(2) + w(3) + 3w(1) - w(0)}{(\Delta r)^3} = \frac{d^3 w}{dr^3}(1) \quad (2.41)$$

Using Eqs. (2.36), (2.37), and (2.41) in Eq. (2.32), at node no. 1, the governing Eq. (2.32) is

$$w_0 \left[\frac{1}{2 r_1^2 (\Delta r)} + \frac{1}{r_1 (\Delta r)^2} - \frac{1}{(\Delta r)^3} \right] + w_1 \left[-\frac{2}{r_1 (\Delta r)^2} + \frac{3}{(\Delta r)^3} \right] + w_2 \left[-\frac{1}{2 r_1^2 (\Delta r)} + \frac{1}{r_1 (\Delta r)^2} - \frac{3}{(\Delta r)^3} \right] + w_3 \left[\frac{1}{(\Delta r)^3} \right] = \frac{p(r_1^2 - r_0^2)}{2 r_1 D_{eq}} \quad (2.42)$$

Using the central differences (Eqs. (2.28)-(2.30)), at the node no. 2, the governing Eq. (2.32) is,

$$w_0 \left[-\frac{1}{2 (\Delta r)^3} \right] + w_1 \left[\frac{1}{2 r_2^2 (\Delta r)} + \frac{1}{r_2 (\Delta r)^2} + \frac{1}{(\Delta r)^3} \right] + w_2 \left[-\frac{2}{r_2 (\Delta r)^2} \right] + w_3 \left[-\frac{1}{2 r_2^2 (\Delta r)} + \frac{1}{r_2 (\Delta r)^2} - \frac{1}{(\Delta r)^3} \right] + w_4 \left[\frac{1}{2 (\Delta r)^3} \right] = \frac{p(r_2^2 - r_0^2)}{2 r_2 D_{eq}} \quad (2.43)$$

and at the node no. 3, using Eqs. (2.28)-(2.30), the governing Eq. (2.32) is,

$$w_1 \left[-\frac{1}{2 (\Delta r)^3} \right] + w_2 \left[\frac{1}{2 (r_3)^2 \Delta r} + \frac{1}{r_3 (\Delta r)^2} + \frac{1}{(\Delta r)^3} \right] + w_3 \left[-\frac{2}{r_3 (\Delta r)^2} \right]$$

$$\begin{aligned}
 & + w_4 \left[-\frac{1}{2 r_3^2 (\Delta r)} + \frac{1}{r_3 (\Delta r)^2} - \frac{1}{(\Delta r)^3} \right] + w_5 \left[\frac{1}{2(\Delta r)^3} \right] \\
 & = \frac{p (r_2^2 - r_0^2)}{2 r_3 D_{eq}} \tag{2.44}
 \end{aligned}$$

w_5 in the Eq. (2.44) is a displacement at fictitious node 5 (Fig. 2.5). The boundary conditions at $r = a$ are, $(\frac{dw}{dr}) = 0$ and $w = 0$ and can be expressed in the finite difference form as

$$\frac{dw}{dr}(4) = \frac{w(5) - w(3)}{2 (\Delta r)} = 0 \tag{2.45}$$

or

$$w(5) = w(3) \tag{2.46}$$

By using the Eq. (2.46), Eq. (2.44) is written as

$$\begin{aligned}
 & w_1 \left[-\frac{1}{2(\Delta r)^3} \right] + w_2 \left[\frac{1}{2 r_3^2 (\Delta r)} + \frac{1}{r_3 (\Delta r)^2} + \frac{1}{(\Delta r)^3} \right] \\
 & + w_3 \left[-\frac{2}{r_3 (\Delta r)^2} + \frac{1}{2 (\Delta r)^3} \right] + w_4 \left[\frac{1}{2 r_3^2 (\Delta r)} + \frac{1}{r_3 (\Delta r)^2} - \frac{1}{(\Delta r)^3} \right] \\
 & = \frac{p (r_2^2 - r_0^2)}{2 r_3 D_{eq}} \tag{2.47}
 \end{aligned}$$

Lastly at the node no. 4 the displacement $w = 0$. Therefore

$$w(4) = 0 \tag{2.48}$$

Thus Eqs. (2.35), (2.42), (2.43), (2.47), and (2.48) contains five

unknowns, $w(0)$, $w(1)$, $w(2)$, $w(3)$, and $w(4)$ and can be solved simultaneously to obtain the unknown displacements. A simple example problem is presented here to illustrate the above method.

Consider a clamped circular plate of radius 25.4 mm and thickness 1.05 mm. Let flexural modulus D_{eq} , of the plate is 5.688 N.m. The displacements in the plate under uniform loading of intensity 100,000 N/m² over the region $0 < r < 12.7$ mm can be obtained as follows:

Since the plate radius is 25.4 mm Δr is $(25.4/4) = 6.35$ mm. Also r_1 , r_2 , r_3 , and r_4 are 6.35 mm, 12.70 mm, 19.05 mm, and 25.4 mm respectively. Substitution of these values in Eqs. (2.35), (2.42), (2.43), (2.47), and (2.48), gives five simultaneous equations, which can be expressed in the matrix form as

$$\begin{bmatrix} -3 & 4 & 1 & 0 & 0 \\ 1 & 2 & -5 & 2 & 0 \\ -4 & 13 & -8 & -5 & 4 \\ 0 & -9 & 25 & -3 & -13 \\ 0 & 0 & 0 & 0 & 1 \end{bmatrix} \begin{Bmatrix} w(0) \\ w(1) \\ w(2) \\ w(3) \\ w(4) \end{Bmatrix} = \frac{p(\Delta r)^4}{D_{eq}} \begin{Bmatrix} 0 \\ 1 \\ 8 \\ 12 \\ 0 \end{Bmatrix} \quad (2.49)$$

or in concise form

$$[A] \{w\} = [F] \quad (2.50)$$

where

$$p = 100,000 \text{ N/m}^2$$

$$\Delta r = 6.35 \text{ mm, and } D_{eq} = 5.688 \text{ N-m}$$

From equation (2.50) $\{w\}$ is

$$\{w\} = [A]^{-1} [F] \quad (2.51)$$

Solving equation (2.51) for $\{w\}$, the nodal displacement are found to be: $w(0) = 0.076226 \text{ mm}$, $w(1) = 0.06677 \text{ mm}$, $w(2) = 0.038410 \text{ mm}$, $w(3) = 0.005434 \text{ mm}$, and $w(4) = 0.0 \text{ mm}$.

2.8 Convergence Study

To study the convergence of this method, the circular plate was idealized into m number of regions with $(m + 1)$ nodes. A systematic convergence study was then made by doubling the number of regions. The number of regions m , used in this convergence study were 4, 8, 16, 32, 60, and 64. Figures 2.6 and 2.7 present the relative errors in the maximum deflections normalized with respect to the exact central displacement, for the two different cases: case (i) uniformly loaded plate and case (ii) a plate loaded uniformly over the regions $0 < \frac{r}{a} < 0.5$. The analysis indicated that about 60 regions were necessary for a plate loaded uniformly over the region $0 < \frac{r}{a} < 0.5$ and for a uniformly loaded plate to yield a solution which is within 0.1 percent of the exact solution.

2.9 Results and Discussion

In this section the central displacements obtained by using the finite difference method are compared with the exact solution. Next deflected shapes of the plate obtained by using the finite difference method, are compared with the exact solution.

The comparison of the central displacements obtained by using the finite difference method and the exact solution is shown in Table 2.2. The percentage errors in the central displacements obtained by using the

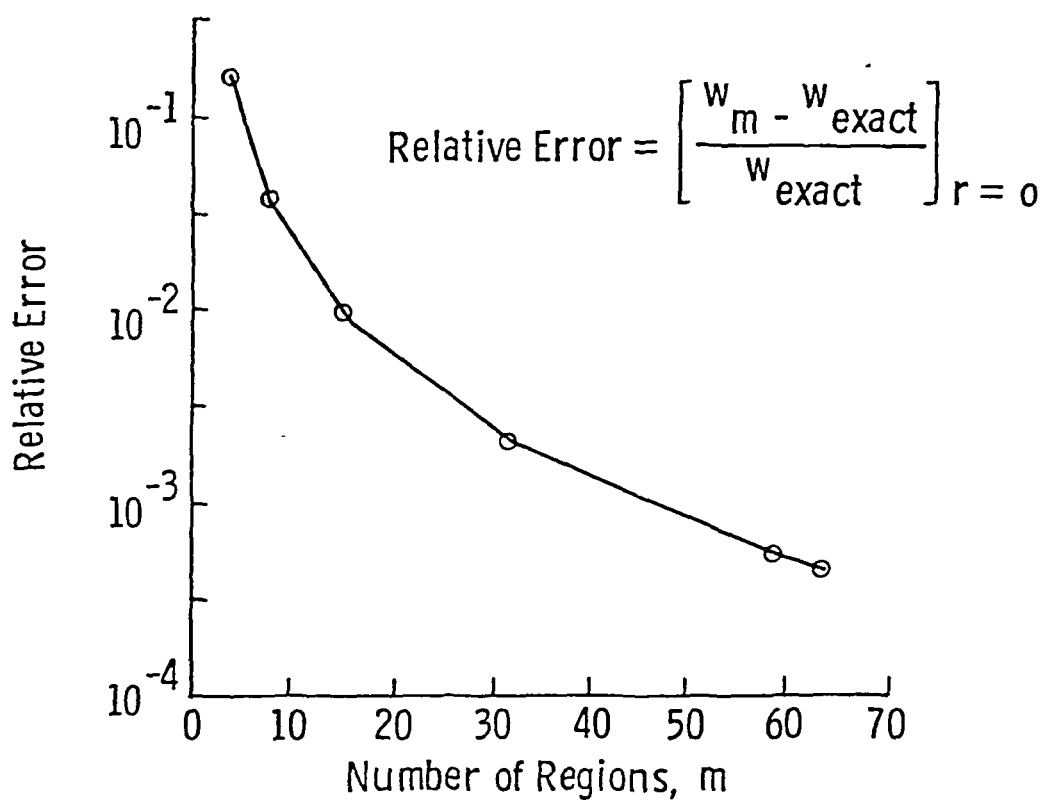


Fig. 2.6 Convergence Study for the Uniformly Loaded Plate

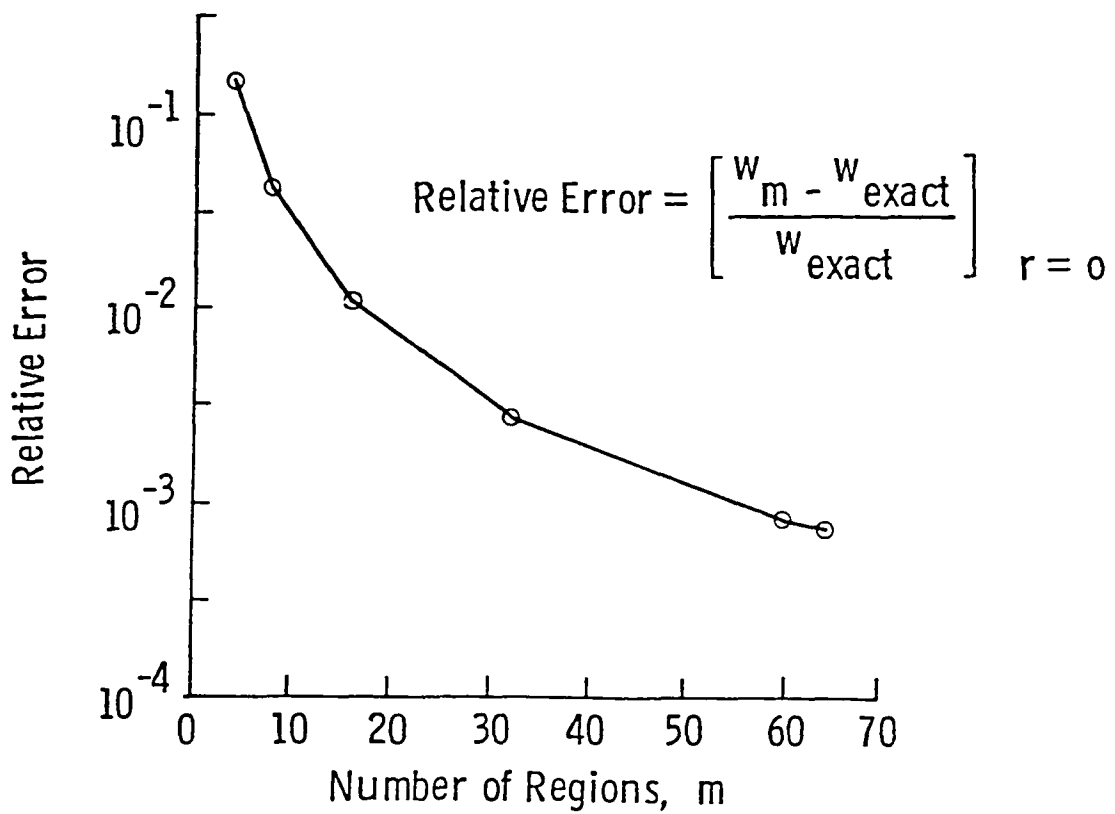


Fig. 2.7 Convergence Study for the Plate Uniformly Loaded Over the Region $0 \leq r/a \leq 0.5$

finite difference method relative to the exact solution were found to be 0.055 percent and 0.072 percent for the uniformly loaded plate and for a plate loaded uniformly over the region $0 < \frac{r}{a} < 0.5$ respectively. Figures 2.8 and 2.9 show the percentage relative errors in the deflected shapes obtained by using the finite difference method and the exact solution, for the uniformly loaded plate and the plate loaded uniformly over the region $0 < \frac{r}{a} < 0.5$. In both the cases maximum percentage error is within 0.1 percent of the exact solution and occur at the center of the plate.

2.10 Concluding Remarks

In this chapter a numerical solution method to obtain the small deflection plate solution for a clamped circular quasi-isotropic plate was developed. The quasi-isotropic plate was modeled as an isotropic plate having the flexural stiffness components equivalent to those of a quasi-isotropic plate. By using a finite difference method, the plate governing differential equation was replaced by a set of algebraic equations. These algebraic equations were solved simultaneously to obtain the transverse displacements for arbitrarily axisymmetrically loaded clamped circular quasi-isotropic laminates. The numerical solution was found to be within 0.1 percent of the exact solution for a uniformly loaded plate and for a plate loaded uniformly over the region $0 < \frac{r}{a} < 0.5$ by using 60 region idealization.

In order to study the large deformation behavior of the quasi-isotropic plate, membrane effects should be incorporated in the small deformation solution. The following chapter presents the large deflection membrane analysis.

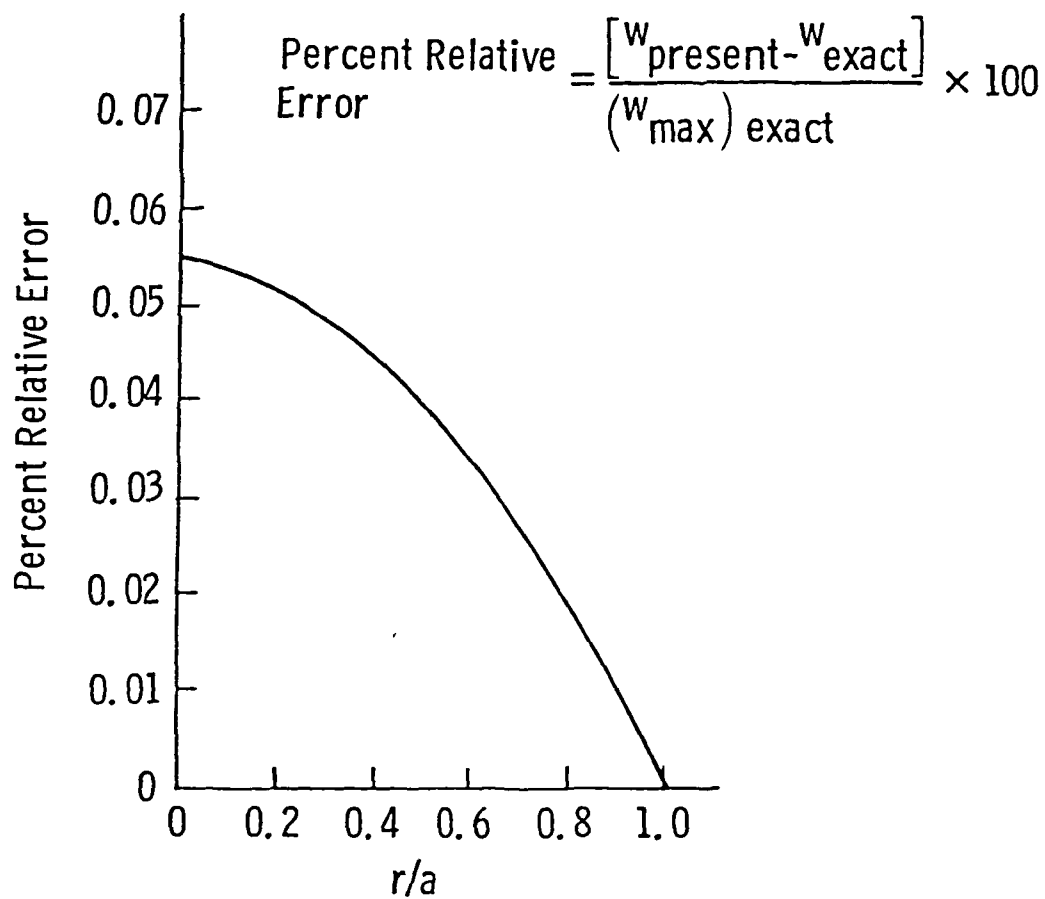


Fig. 2.8 Comparison of the Deflected Shape Obtained by Using the Finite Difference Method and the Exact Deflected Shape for the Uniformly Loaded Plate

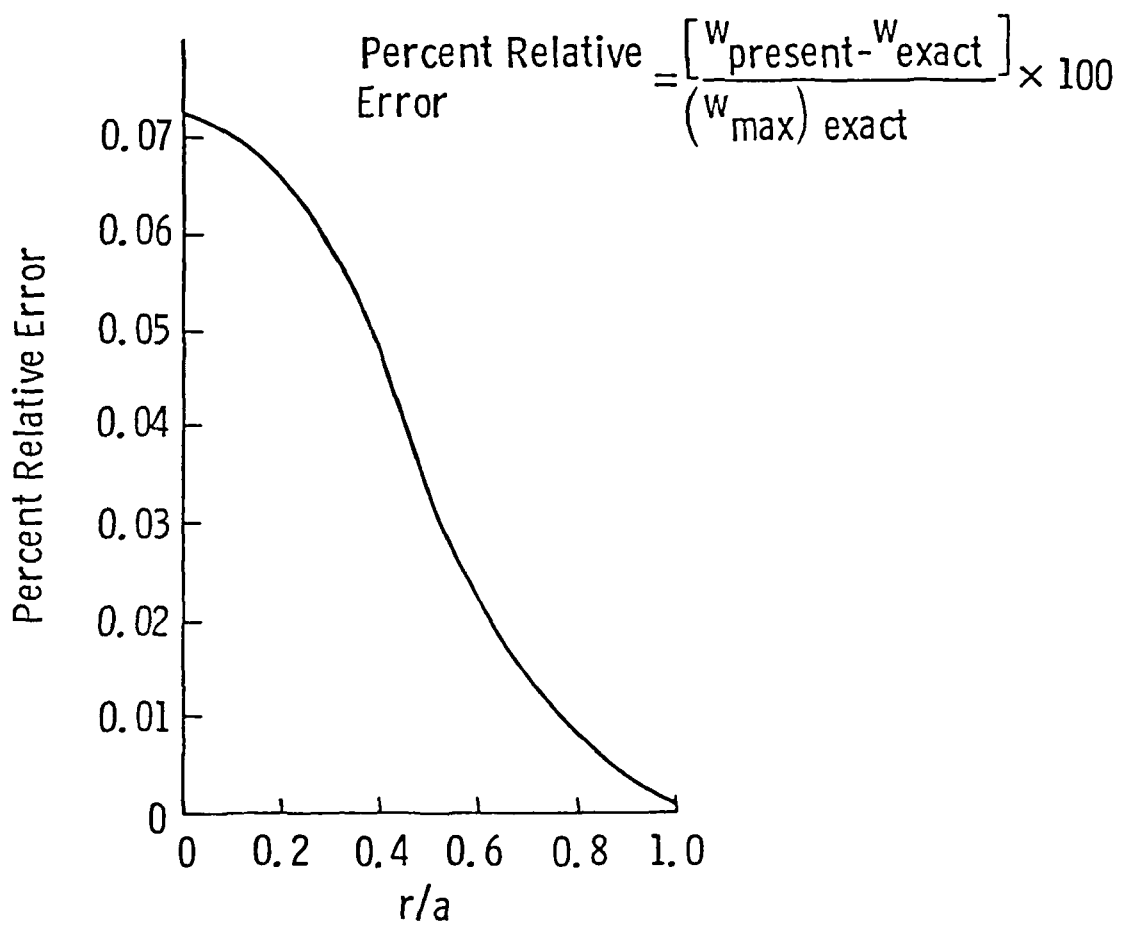


Fig. 2.9 Comparison of the Deflected Shape Obtained by Using the Finite Difference Method and the Exact Deflected Shape for the Plate Uniformly Loaded Over the Region $0 \leq r/a \leq 0.5$

Table 2.1 - Elastic Properties of the Plate

Material	<u>Modulus GPa</u>			Poisson ratio
	E_{11}	E_{22}	G_{12}	
Gr/Ep lamina	131.0	13.0	6.4	0.34

Number of plies = 8

Laminate thickness = 1.05 mm

Stacking sequence: [45/0/-/45/90]_s

(Subscripts 11 and 22 correspond to the longitudinal and transverse direction of fiber)

Table 2.2 - Comparison of Maximum Center Displacements for Uniformly Loaded Plate and for a Plate Uniformly Loaded Over the Region $0 < \frac{r}{a} < 0.5$

Central transverse displacement w , at $r = 0$.		
Type of loading	Present* solution	Exact solution (ref. 27)
Uniform loading	$0.015633 \frac{pa^4}{D_{eq}}$	$0.015625 \frac{pa^4}{D_{eq}}$
Uniform load over the region $0 < \frac{r}{a} < 0.5$	$0.009994 \frac{pa^4}{D_{eq}}$	$0.009987 \frac{pa^4}{D_{eq}}$

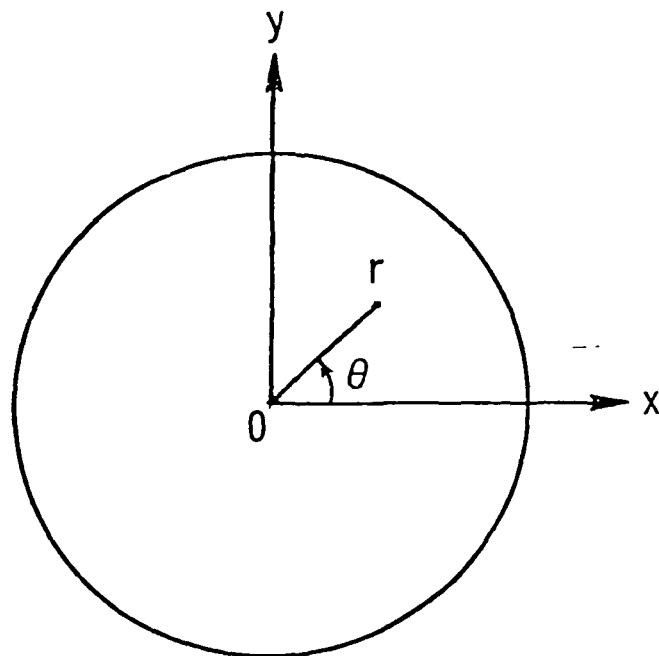
*Obtained by using 60 regions idealization

Chapter 3

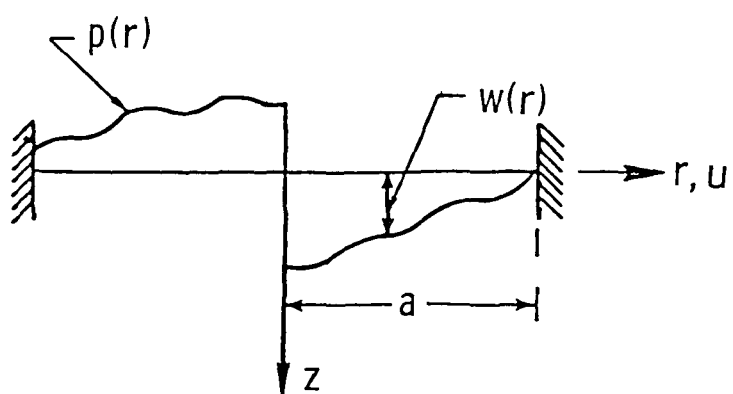
LARGE DEFLECTION MEMBRANE ANALYSIS

3.1 Introduction

In Chap. 1, a plate-membrane coupling model was proposed to obtain the large deformation behavior of quasi-isotropic laminates under point loads simulating low-velocity impact. This model requires a small deflection plate solution and a large deflection membrane solution. In the previous chapter a numerical method to obtain a small deformation solution for a clamped circular quasi-isotropic plate, subjected to arbitrary axisymmetric loading was developed. In this chapter a numerical method is developed to obtain a large deflection membrane solution. Again a quasi-isotropic circular laminate is considered in the membrane analysis. This quasi-isotropic laminate has only extensional stiffness but no shear and flexural stiffnesses. As pointed out in the previous chapter, quasi-isotropic T300/5208 circular laminates with the stacking sequence of $[45/0/-45/90]_S$ are axially isotropic, i.e., extensional stiffness of these laminates is independent of the polar angle (Fig. 3.1). Hence, these circular laminates, with only extensional stiffness, can be modeled as circular isotropic membranes. In this chapter, a general analysis of circular isotropic membranes with clamped peripheral edges, subjected to arbitrary axisymmetric loading is presented. A single governing equation in terms of radial stress is developed. The solution of this nonlinear governing



(a) Circular Membrane



(b) Loading and deformations

Fig. 3.1 Membrane Configuration

equation is presented by using the finite difference method in conjunction with Newton-Raphson method. Three loading cases namely (a) uniformly loaded membrane, (b) a membrane with uniform load over an inner portion, and (c) a membrane with ring load are analyzed and the results are compared with the classical solution.

3.2 Membrane Configuration and Strain-Displacement Relations

Figure 3.1(a) shows an axisymmetrically loaded clamped membrane with thickness h and radius a . Since the deflection surface is axisymmetrical, the displacement can be resolved into two components: (1) a component u in the radial direction, and (2) a component w perpendicular to the plane of the membrane. From large deflection theory [27], strain-displacement relations for an isotropic membrane are obtained as follows:

Consider an element AB of length dr as shown in Fig. 3.2. The radial strain ϵ_r from Fig. 3.2 can be expressed as

$$\epsilon_r = \frac{(u + \frac{du}{dr} dr) - u}{dr} + \frac{ds - dr}{dr} \quad (3.1)$$

but

$$\frac{ds - dr}{dr} = \sqrt{1 + (\frac{dw}{dr})^2} - 1 \approx \frac{1}{2} (\frac{dw}{dr})^2 \quad (3.2)$$

Substituting Eq. (3.2) into Eq. (3.1)

$$\epsilon_r = \frac{du}{dr} + \frac{1}{2} (\frac{dw}{dr})^2 \quad (3.3)$$

The tangential strain ϵ_θ from the Fig. 3.3 is

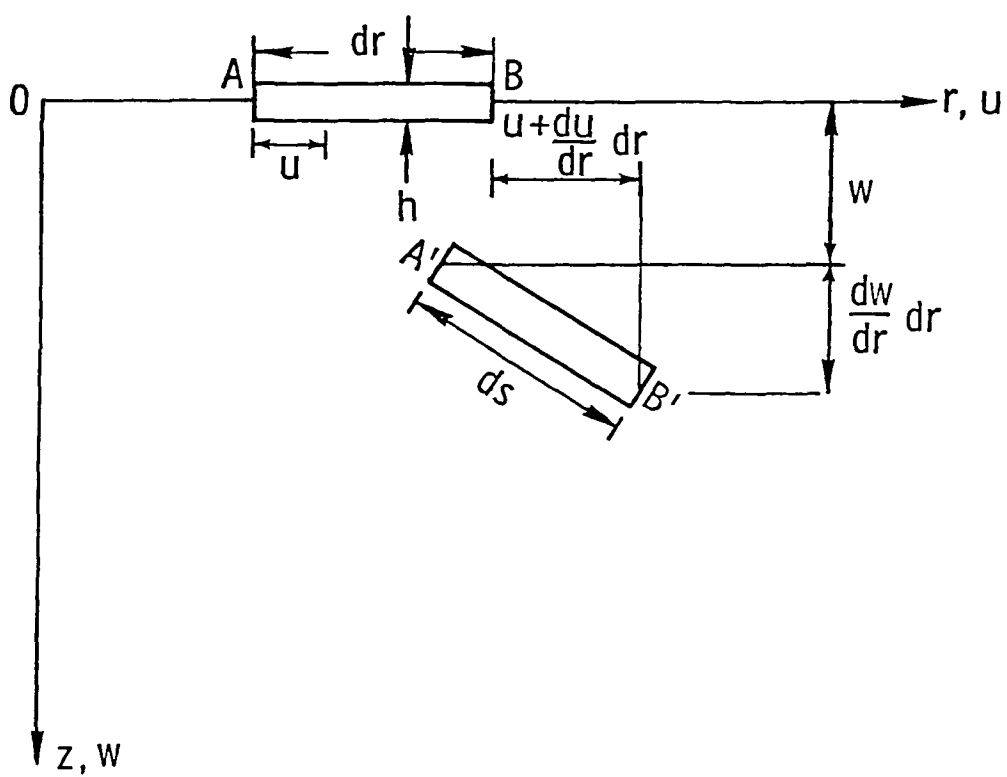


Fig. 3.2 Radial Strain Due to Large Deflections

$$\epsilon_{\theta} = \frac{(r + u) \frac{d\theta}{dr} - r \frac{d\theta}{dr}}{rd\theta} = \frac{u}{r} \quad (3.4)$$

By using Eqs. (3.3) and (3.4), the radial and tangential stresses are:

$$\sigma_r = \frac{E_{eq}}{(1-v_{eq})^2} \left[\frac{du}{dr} + \frac{1}{2} \left(\frac{dw}{dr} \right)^2 + v_{eq} \frac{u}{r} \right] \quad (3.5)$$

$$\sigma_{\theta} = \frac{E_{eq}}{(1-v_{eq})^2} \left[\frac{u}{r} + v_{eq} \frac{du}{dr} + \frac{v_{eq}}{2} \left(\frac{dw}{dr} \right)^2 \right] \quad (3.6)$$

where E_{eq} and v_{eq} are the equivalent Young's modulus and Poisson's ratio of the isotropic membrane and were calculated by using the technique presented in Chap. 2.

Note that the assumption of large deflection but with small strains is made in this formulation.

3.2.1 Equilibrium Equations

The equation of equilibrium in the radial direction is obtained as follows:

Consider stresses on an infinitesimal element abcd of unit thickness as shown in Fig. 3.3. Summing the forces in the radial direction along the radial line $(\theta + \frac{d\theta}{2})$ one has

$$\begin{aligned} & (\sigma_r + \frac{d\sigma_r}{dr} dr) (r + dr) d\theta - \sigma_r r d\theta - \sigma_{\theta} dr \sin \frac{d\theta}{2} \\ & - (\sigma_{\theta} + \frac{d\sigma_{\theta}}{d\theta} d\theta) dr \sin \frac{d\theta}{2} = 0 \end{aligned} \quad (3.7)$$

Since $d\theta$ is small, $\sin(\frac{d\theta}{2})$ may be replaced by $(\frac{d\theta}{2})$. By neglecting higher order terms the equation of equilibrium in radial

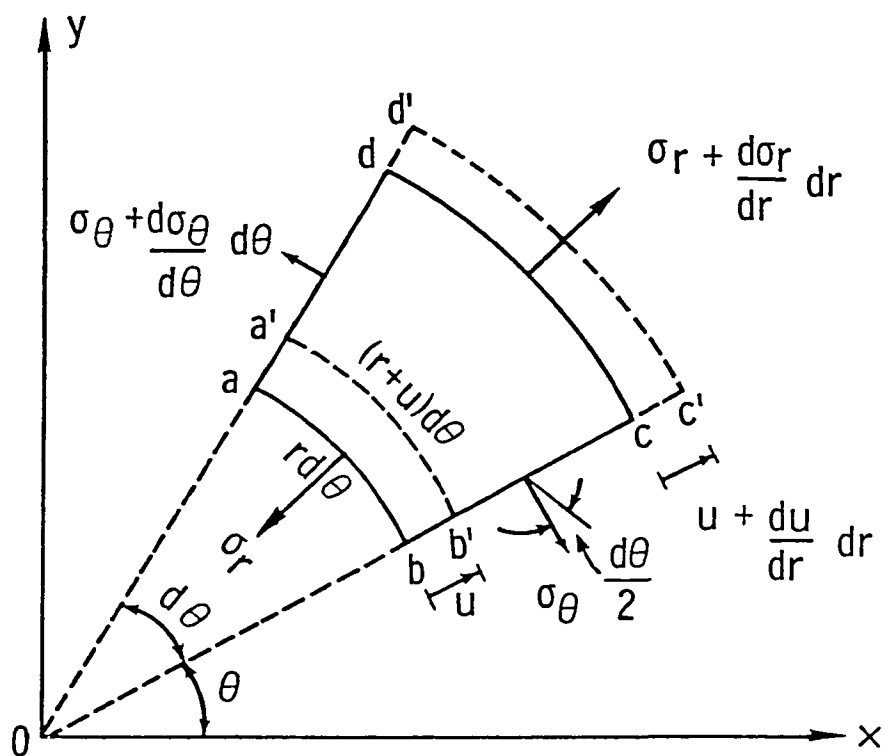


Fig. 3.3 State of Stress on the Membrane Element

direction is

$$\sigma_r - \sigma_\theta + r \frac{d\sigma_r}{dr} = 0 \quad (3.8)$$

The equation of equilibrium in the direction perpendicular to the plane of the membrane, with general axisymmetric loading $p(r)$ is obtained as follows:

Consider a stretched circular membrane element with general axisymmetric loading $p(r)$ as shown in the Fig. 3.4. Consider the free body equilibrium of the deflected membrane, i.e. the vertical component of the reaction must equal the total load. Therefore from Fig. 3.4

$$2\pi r h \sigma_r \sin \alpha - \int_0^r p(\xi) 2\pi \xi d\xi = 0 \quad (3.9)$$

For small α , $\sin \alpha = \tan \alpha = \frac{dw}{dr}$

Therefore the equation of equilibrium in the direction perpendicular to the plane of the membrane with general axisymmetric loading $p(r)$ is

$$2\pi r h \sigma_r \frac{dw}{dr} - \int_0^r p(\xi) 2\pi \xi d\xi = 0 \quad (3.10)$$

The stress and strain displacement relations (Eqs. (3.3)-(3.6)) and equilibrium Eq. ((3.8) and (3.10)) when combined form four nonlinear partial differential equations with four unknowns σ_r , σ_θ , u , and w .

To obtain a numerical solution of these governing equations the conventional approach is to reduce these four nonlinear equations to two equations containing only u and w displacements. This conventional approach is applicable when u and w displacements are of the same order of magnitude, for example, a case of uniformly loaded membrane as shown

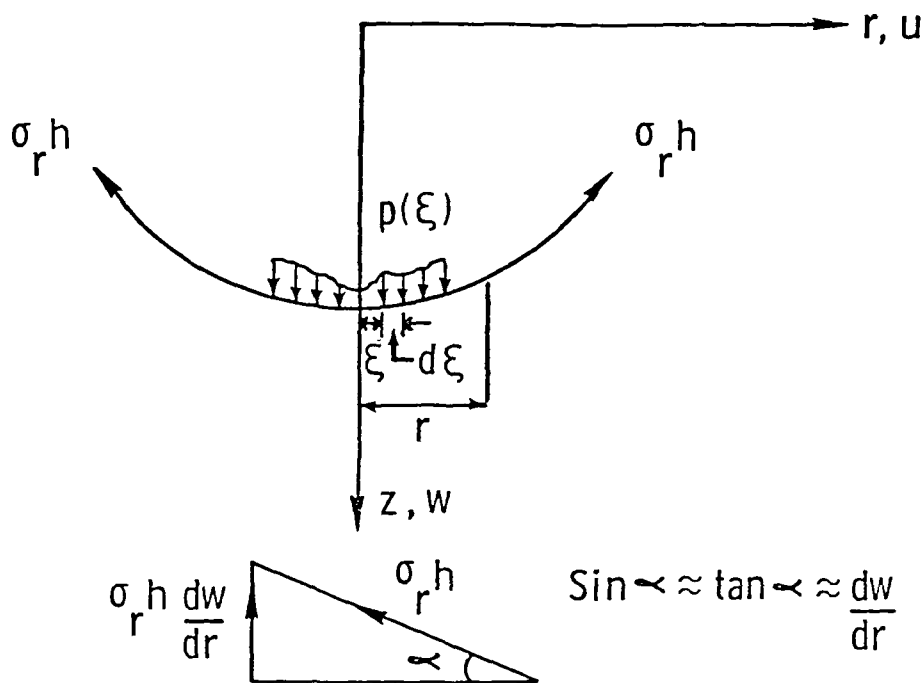


Fig. 3.4 Stretched Circular Membrane

by Shaw and Perrone [31], and Kao and Perrone [53]. However, the numerical solution of arbitrary axisymmetrically loaded membranes cannot be obtained by using the conventional approach because of the large differences in magnitudes of u and w displacements. Due to these large differences the two governing equations involving u and w displacements are difficult to satisfy. Hence an alternate formulation of the membrane problem is presented below.

3.2.2 Derivation of a Governing Equation

Using the stress and strain displacement relations (Eqs. (3.3)-(3.6)), the radial displacement u was expressed as

$$u = \frac{r}{E_{eq}} (\sigma_\theta - v_{eq} \sigma_r) \quad (3.11)$$

The term $\frac{du}{dr}$ was obtained by differentiating the radial displacement u , with respect to r .

$$\frac{du}{dr} = \frac{1}{E_{eq}} (\sigma_\theta - v_{eq} \sigma_r) + \frac{r}{E_{eq}} \left(\frac{d\sigma_\theta}{dr} - v_{eq} \frac{d\sigma_r}{dr} \right) \quad (3.12)$$

The strain in the radial direction ϵ_r was expressed in terms of the radial and tangential stresses and by using the strain-displacement relations (Eqs. (3.3) and (3.4)),

$$\epsilon_r = \frac{1}{E_{eq}} (\sigma_r - v_{eq} \sigma_\theta) = \left[\frac{du}{dr} + \frac{1}{2} \left(\frac{dw}{dr} \right)^2 \right] \quad (3.13)$$

By using $\frac{du}{dr}$ from Eq. (3.12) in equation (3.13) the following relationship was obtained:

$$(\sigma_\theta - \sigma_r) \left(\frac{1 + v_{eq}}{E_{eq}} \right) + \frac{r}{E_{eq}} \left[\frac{d\sigma_\theta}{dr} - v_{eq} \frac{d\sigma_r}{dr} \right] + \frac{1}{2} \left(\frac{dw}{dr} \right)^2 = 0 \quad (3.14)$$

From the equation of equilibrium in radial direction (Eq. (3.8)),

$(\frac{d\sigma_r}{dr})$ was written as

$$\frac{d\sigma_r}{dr} = \frac{1}{r} (\sigma_r - \sigma_\theta) \quad (3.15)$$

Substituting Eq. (3.15) in Eq. (3.14) and rearranging the terms the following relationship was obtained:

$$\frac{r}{E_{eq}} \left(\frac{d\sigma_\theta}{dr} + \frac{d\sigma_r}{dr} \right) + \frac{1}{2} \left(\frac{dw}{dr} \right)^2 = 0 \quad (3.16)$$

Further, $\frac{d\sigma_\theta}{dr}$ was obtained by differentiating the equation of equilibrium (Eq. (3.8)) in radial direction with respect to r , as

$$\frac{d\sigma_\theta}{dr} = 2 \frac{d\sigma_r}{dr} + r \frac{d^2\sigma_r}{dr^2} \quad (3.17)$$

Substituting this value of $(\frac{d\sigma_\theta}{dr})$ in governing Eq. (3.16), the following relationship was obtained:

$$\frac{r}{E_{eq}} \left(3 \frac{d\sigma_r}{dr} + r \frac{d^2\sigma_r}{dr^2} \right) + \frac{1}{2} \left(\frac{dw}{dr} \right)^2 = 0 \quad (3.18)$$

By using equation of equilibrium (Eq. (3.10)) in the direction perpendicular to the plane of membrane, $(\frac{dw}{dr})^2$ was written as

$$\left(\frac{dw}{dr} \right)^2 = \left[\frac{\int_0^r p(\xi) 2 \pi \xi d\xi}{2 \pi r h \sigma_r} \right]^2 \quad (3.19)$$

Substituting this value of $(\frac{dw}{dr})^2$ in the governing equation, Eq. (3.18) gives

$$\frac{r}{E_{eq}} \left(3 \frac{d\sigma_r}{dr} + r \frac{d^2\sigma_r}{dr^2} \right) + \frac{1}{2} \left[\frac{\int_0^r p(\xi) \xi d\xi}{r h \sigma_r} \right]^2 = 0 \quad (3.20)$$

Equation (3.20) is a nonlinear differential equation in terms of the radial stress that governs the large deflection response of the membrane with arbitrary axisymmetric loading. Several investigators obtained the governing equation in terms of the radial stress σ_r , similar to Eq. (3.20). Dickey [30] and Weinitzschke [33] presented the differential equation for uniformly distributed load. Callegari and Reiss [35] obtained the differential equation for a membrane with an arbitrary axisymmetric loading.

3.3 Solution Method

To solve the governing equation (3.20) for the radial stress, Dickey [30] used integral equation method, Weinitzschke [33] used integral equation and power series approaches and Callegari and Reiss [35] used the shooting method. In contrast, here a numerical method of solution is proposed. The nonlinear differential equation was replaced by a set of nonlinear algebraic equations using difference quotients. Then using the Newton-Raphson method [52], these nonlinear algebraic equations were solved numerically to obtain the stresses and displacements. The details of the solution method are as follows:

The solution domain was discretized into m regions and $(m + 1)$ nodes. Denoting $\sigma_r(n)$ as the radial stress at the n th node, the governing equation, Eq. (3.20) was rewritten as, at any node n :

$$\frac{r_n}{E_{eq}} \left[3 \frac{d\sigma_r}{dr}(n) + r_n \frac{d^2\sigma_r}{dr^2}(n) \right] + \frac{1}{2} \left[\frac{\int_0^{r_n} p(\xi) \xi d\xi}{r_n h \sigma_n(n)} \right]^2 = 0 \quad (3.21)$$

To simplify the evaluation of the integral in the above equation, the same assumption as discussed in previous chapter will be made. Consider an i th region with $r_{i-1} < r < r_i$. Although the applied load varies within the region $r_{i-1} < r < r_i$, the load will be assumed to be uniform in this region with a value of p_i . The magnitude of p_i is assumed equal to the value of the load at the midpoint of this region, i.e., at $r = (r_i + r_{i-1})/2$. As the number of regions in the model become large, the size of each region reduces and hence the variation of the load within each region also becomes insignificant. With this assumption the governing equation, Eq. (3.21), reduces to

$$\frac{r_n}{E_{eq}} \left[3 \frac{d\sigma_r}{dr}(n) + r_n \frac{d^2\sigma_r}{dr^2}(n) \right] + \frac{1}{8} \left[\frac{1}{r_n h \sigma_r(n)} \sum_{i=1}^n p_i (r_i^2 - r_{i-1}^2) \right]^2 = 0 \quad (3.22)$$

First and second derivatives of the radial stress from the governing Eq. (3.22) were replaced by using the central finite differences as:

$$\frac{d\sigma_r}{dr}(n) = \frac{\sigma_r(n+1) - \sigma_r(n-1)}{2(\Delta r)}$$

and

$$\frac{d^2\sigma_r}{dr^2}(n) = \frac{\sigma_r(n+1) - 2\sigma_r(n) + \sigma_r(n-1)}{(\Delta r)^2}$$

3.3.1 Boundary Conditions

For the circular isotropic membrane with axisymmetric loading the boundary conditions were:

1. Both the radial displacement u and the transverse displacement w equal zero at the fixed edge ($r = a$).
2. The radial displacement u and the slope $\frac{dw}{dr}$ equal zero at the center ($r = 0$).

Since the governing equation, Eq. (3.20) was derived in terms of the radial stress, the transformation of boundary conditions was done by using stress and strain-displacement relations (Eqs. (3.3)-(3.6)) and equilibrium euqations, Eqs. (3.8) and (3.10). When $u = 0$ and $r = a$ are substituted into equation (3.11) for radial displacement, the boundary condition no. 1 above can be transformed to

$$\sigma_\theta = v_{eq} \sigma_r, \quad \text{at } r = a \quad (3.23)$$

Using this boundary condition in the equilibrium equation in the radial direction (Eq. (3.8)), Eq. (3.23), was further transformed to

$$\sigma_r (1-v_{eq}) + r \frac{d\sigma_r}{dr} = 0, \quad \text{at } r = a \quad (3.24)$$

The boundary condition (2) above is a statement of symmetry about $r = 0$, the center of the membrane. This symmetry condition can be expressed in terms of the radial stresses,

$$\frac{d\sigma_r}{dr} = 0, \quad \text{at } r = 0 \quad (3.25)$$

Using the governing equation, Eq. (3.22),

$$\frac{r_n}{E_{eq}} [3 \frac{d\sigma_r}{dr} r(n) + r_n \frac{d^2\sigma_r}{dr^2}(n)] + \frac{1}{8} \left\{ \sum_{i=1}^n \frac{p_i (r_i^2 - r_{i-1}^2)}{r_n h \sigma_r(n)} \right\}^2 = 0$$

and boundary conditions (Eqs. (3.24) and (3.25)) in the form of finite difference quotients at each node, $m + 1$, nonlinear algebraic equations were obtained. These algebraic equations contained $m + 1$ unknowns, viz., $\sigma_r(0) \dots \sigma_r(m)$. By using the Newton-Raphson technique as described in Appendix A, these $(m+1)$ equations were solved to obtain the radial stress at each node.

Once the radial stresses were known, at each node, the $\frac{d\sigma_r}{dr}$ at each node was calculated by using the finite difference method. Using these values of σ_r and $\frac{d\sigma_r}{dr}$ in Eq. (3.8), the tangential stress σ_θ at each node was obtained. By using Eq. (3.11), the radial displacement u at each node, was obtained. The slope $\frac{dw}{dr}$ at any node was obtained using Eq. (3.19). Then using the boundary conditions,

$$w = 0 \text{ at } r = a,$$

$$\frac{dw}{dr} = 0 \text{ at } r = 0,$$

and the finite difference representation of the slope, $\frac{dw}{dr}$, at each node, $(m + 1)$ simultaneous equations with $w(0) \dots w(m)$ unknowns, were obtained. These $(m + 1)$ equations were then solved to obtain transverse displacement w at each node. The details for a simple four region idealization to obtain radial stresses at each node are presented next:

3.3.2 Illustrative Example

Consider a clamped circular membrane with radius a and thickness h .

The membrane is subjected to a uniform loading over the region $0 < \frac{r}{a} < 0.5$. The objective is to obtain the membrane displacements using the finite difference method.

The solution domain $0 < \frac{r}{a} < 1.0$ is discretized into 4 regions and 5 nodes (Fig. 3.5). At the node 0, the boundary condition is $\frac{d\sigma_r}{dr} = 0$ (Eq. (3.25)). This boundary condition can be written in the finite difference form using Eq. (2.35) as

$$4 \sigma_r(1) - 3 \sigma_r(0) - \sigma_r(2) = 0 \quad (3.26)$$

The governing differential equation at any node n for the membrane is (Eq. (3.22))

$$\frac{r_n}{E_{eq}} [3 \frac{d^2 \sigma_r}{dr^2}(n) + r_n \frac{d^2 \sigma_r}{dr^2}(n)] + \frac{1}{8} \left\{ \sum_{i=1}^n \frac{p_i (r_i^2 - r_{i-1}^2)}{r_n h \sigma_r(n)} \right\}^2 = 0$$

For the nodes 1, 2 and 3 the first and second derivatives can be expressed in the finite difference form, and by using central difference equations, Eqs. (2.28) and (2.29), Eq. (3.22) is

At the node 1:

$$\begin{aligned} -0.5 \sigma_r(0) \sigma_r^2(1) - 2 \sigma_r^3(1) + 2.5 \sigma_r(2) \sigma_r^2(1) \\ = - \frac{p^2 a^2 E_{eq}}{128 h^2} \end{aligned} \quad (3.27)$$

At the node 2:

$$\begin{aligned} \sigma_r(1) \sigma_r^2(2) - 8 \sigma_r^3(2) + 7 \sigma_r(3) \sigma_r^2(2) \\ = - \frac{p^2 a^2 E_{eq}}{32 h^2} \end{aligned} \quad (3.28)$$

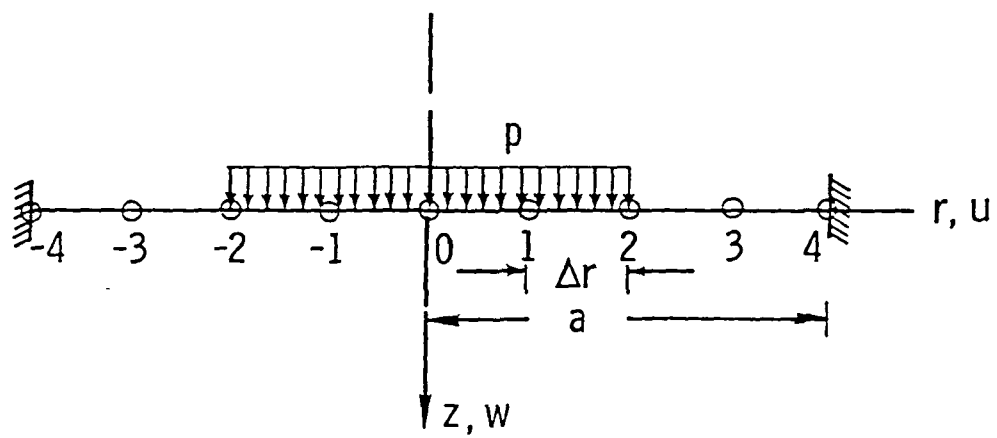


Fig. 3.5 Four Region Idealization for the Membrane
Uniformly Loaded Over the Region $0 \leq r/a \leq 0.5$

At the node 3:

$$1.5 \sigma_r(2) \sigma_r^2(3) - 6 \sigma_r^3(3) + 4.5 \sigma_r(4) \sigma_r^2(3) \quad (3.29)$$

$$= - \frac{p^2 a^2 E_{eq}}{216 h^2}$$

At the node 4, the boundary condition (Eq. 3.24)) needs to be satisfied. This condition is

$$\sigma_r(4) (1 - v_{eq}) + r_4 \frac{d\sigma_r}{dr}(4) = 0 \quad (3.30)$$

The $\frac{d\sigma_r}{dr}(4)$ in the Eq. (3.30) can be obtained as follows:

Using the Taylor's series expansion $\sigma_r(3)$ and $\sigma_r(2)$ can be written as:

$$\sigma_r(3) = \sigma_r(4) - \frac{(\Delta r)}{1!} \frac{d\sigma_r}{dr}(4) + \frac{(\Delta r)^2}{2!} \frac{d^2\sigma_r}{dr^2}(4) \quad (3.31)$$

$$\sigma_r(2) = \sigma_r(4) - \frac{2\Delta r}{1!} \frac{d\sigma_r}{dr}(4) + \frac{(2\Delta r)^2}{2!} \frac{d^2\sigma_r}{dr^2}(4) \quad (3.32)$$

By eliminating $\frac{d^2\sigma_r}{dr^2}(4)$ terms from the Eqs. (3.31) and (3.32) and solving for $\frac{d\sigma_r}{dr}(4)$, the $\frac{d\sigma_r}{dr}(4)$ is obtained as follows:

$$\frac{-4 \sigma_r(3) + \sigma_r(2) + 3 \sigma_r(4)}{2 \cdot (\Delta r)} = \frac{d\sigma_r}{dr}(4) \quad (3.33)$$

Substituting Eq. (3.33) into Eq. (3.30) the equation at the node 4 is

$$2 \sigma_r(2) - 8 \sigma_r(3) + \sigma_r(4) (6 + (1 - v_{eq})) = 0 \quad (3.34)$$

Equation (3.26), (3.27), (3.28), (3.29), and (3.34) are the five nonlinear algebraic equations and they contain five unknowns $\sigma_r(0)$, $\sigma_r(1)$, $\sigma_r(2)$, $\sigma_r(3)$, and $\sigma_r(4)$. These nonlinear algebraic equations are solved by using Newton-Raphson's method (see Appendix A) to obtain the unknown radial stress at each node. As discussed earlier, once the radial stresses were known at each node, the equation of equilibrium in the radial direction (Eq. (3.8)), was used to obtain the tangential stress, σ_θ , at each node. The radial displacement, u , and the slope, $\frac{dw}{dr}$, at any node were obtained by using Eqs. (3.11) and (3.18), respectively, and the σ_r and σ_θ values at that node. Then using the boundary conditions,

$$w = 0 \text{ at } r = a,$$

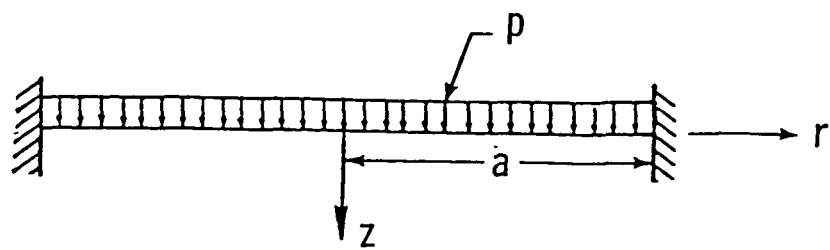
$$\frac{dw}{dr} = 0 \text{ at } r = 0$$

and the finite difference representation of the slope, $\frac{dw}{dr}$, at all the nodes, the transverse displacements, w , were determined.

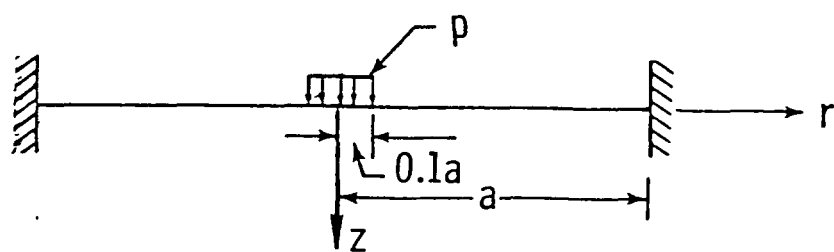
3.4 Convergence Study

In this section, first a convergence study for the above outlined method is presented. Then, the present method is illustrated for circular membranes with different loadings, shown in Fig. 3.6.

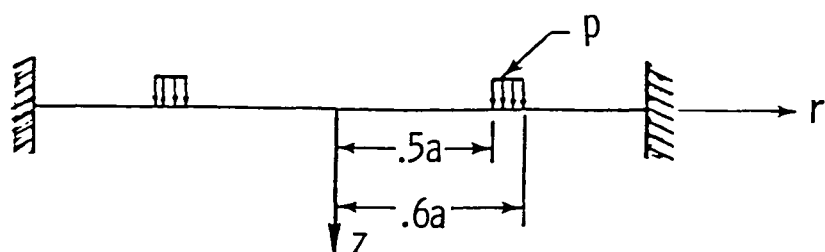
1. Uniformly loaded circular membrane.
2. A membrane with uniformly distributed load over the inner portion.



(a) Uniform loading



(b) Uniform load over inner portion



(c) Ring loading

Fig. 3.6 Types of Loading on the Membrane

3. A membrane with a ring load.

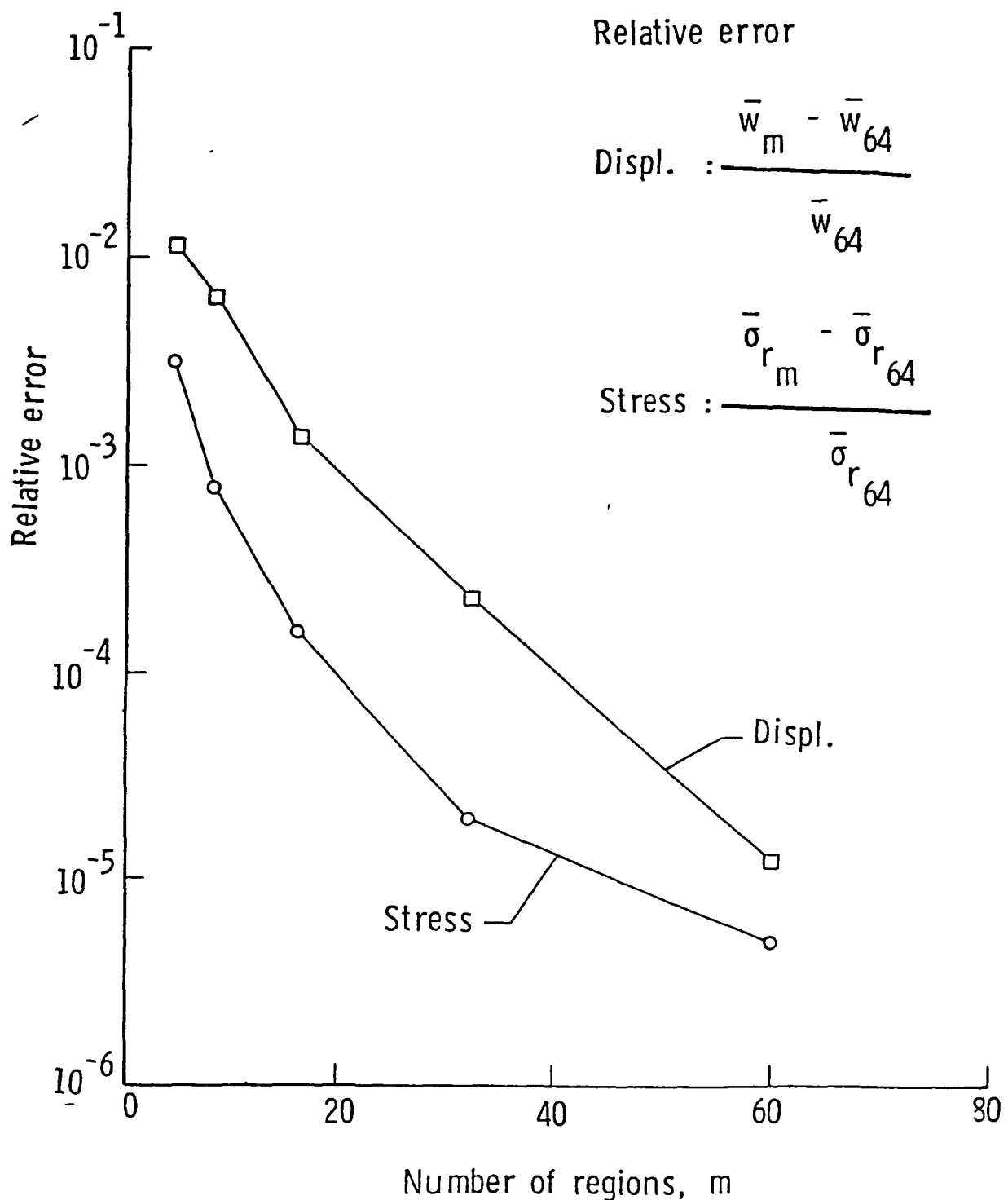
The stresses and displacements were expressed in dimensionless forms, using Hencky's normalized formulation as,

$$\bar{u} = \frac{u}{a \left(\frac{pa}{E_{eq} h} \right)^{2/3}} \quad \bar{w} = \frac{w}{a \left(\frac{pa}{E_{eq} h} \right)^{1/3}}$$

$$\bar{\sigma}_r = \frac{\sigma_r}{\left(\frac{p^2 a^2}{h^2} \frac{E_{eq}}{E_{eq}} \right)^{1/3}} \quad \bar{\sigma}_\theta = \frac{\sigma_\theta}{\left(\frac{p^2 a^2}{h^2} \frac{E_{eq}}{E_{eq}} \right)^{1/3}}$$

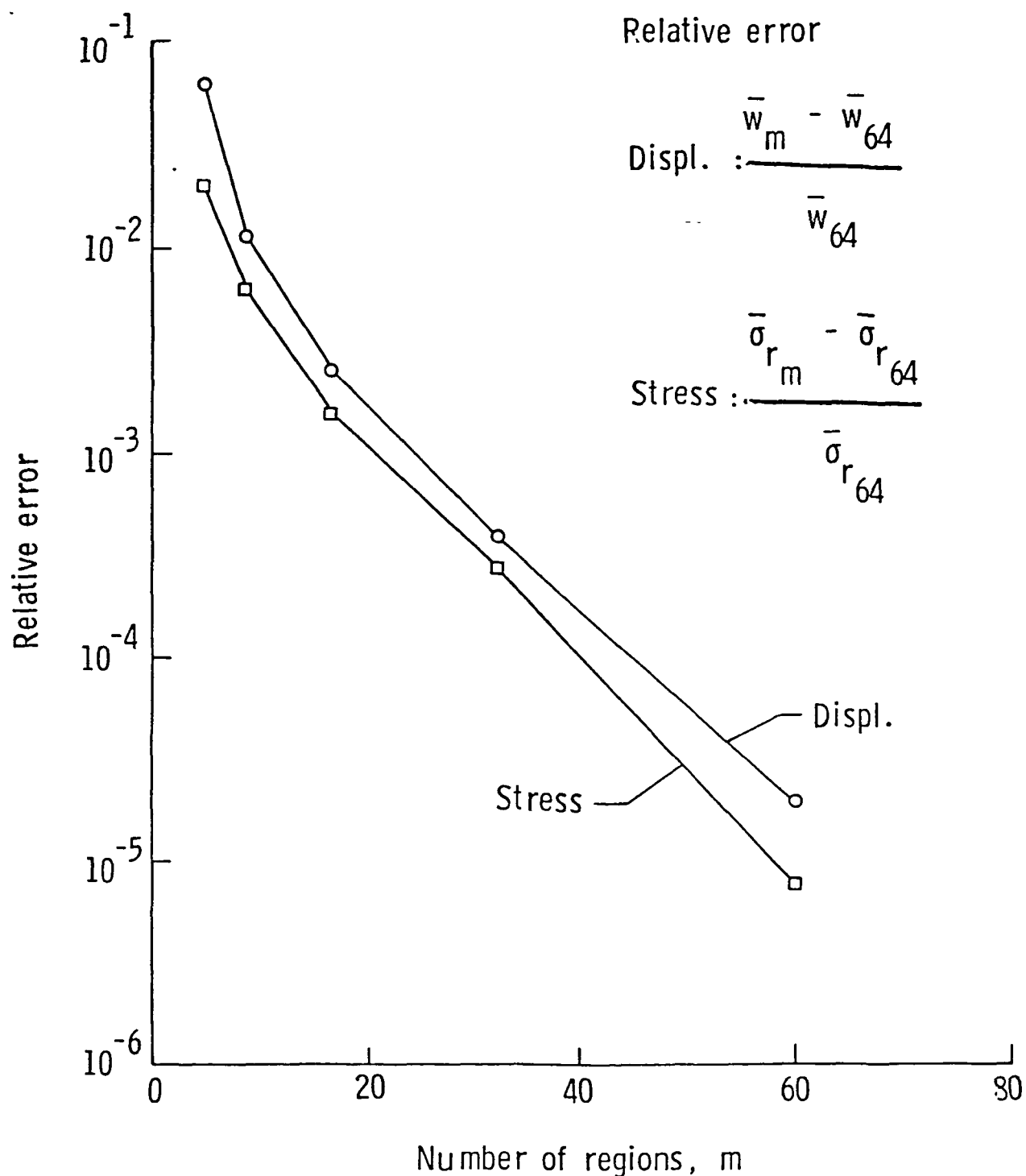
To study the convergence of the present method, the circular membrane was idealized into m number of regions with $(m + 1)$ nodes, (where nodes are numbered from the center to the outside). The number of regions, m , used in this convergence study were 8, 16, 32, 60, and 64. Figures 3.7(a) and 3.7(b) present the relative errors in the normalized maximum deflections and stresses, for a uniformly loaded membrane and for a membrane loaded uniformly over the region $0 < \frac{r}{a} < 0.5$. The solution shows rapid convergence and about 60 regions were found to be necessary for a membrane loaded uniformly over the region $0 < \frac{r}{a} < 0.5$, to yield a solution which is within 0.001 percent of the converged solution. In contrast much fewer than 60 regions were necessary for the uniformly loaded membrane. However, a 60 region idealization is used in the analysis and all the results are presented for this idealization.

The Newton-Raphson method used here needs initial $\bar{\sigma}_r$ values for



(a) Uniform Loading

Fig. 3.7 Convergence Study for the Membrane



(b) Uniform Loading Over the Region $0 \leq r/a \leq 0.5$

Fig. 3.7 Convergence Study for the Membrane

the iterative process. The sensitivity of the present method to these initial values was studied. Table 3.1 presents the number of iterations needed to achieve convergence for a range of initial $\bar{\sigma}_r$ values for the three configurations studied. The initial $\bar{\sigma}_r$ values were as low as three orders of magnitude smaller than the maximum converged value of $\bar{\sigma}_r$ and as high as three orders of magnitude higher. For the uniformly loaded membrane with each of these initial values the present method converged to the same solution. The other two configurations showed similar convergence, thus showing insensitivity to the initial $\bar{\sigma}_r$ values. When the initial $\bar{\sigma}_r$ values were farther away from the converged values the number of iterations needed were around 40 compared to about 8 when the initial $\bar{\sigma}_r$ values were closer to the converged $\bar{\sigma}_r$ values.

3.4.1 Uniformly Loaded Circular Membrane

The first problem analyzed was that of a uniformly loaded circular membrane, for which classical solution [29] exists. The uniform loading was represented by setting the magnitude of loading terms p_1 through p_{60} equal to unit values. Using these values in Eq. (3.22), the governing equation for the membrane was solved by using the procedure outlined earlier. The values of \bar{u} and \bar{w} displacements and stresses $\bar{\sigma}_r$ and $\bar{\sigma}_\theta$ are presented in Figs. 3.8 and 3.9, respectively. A comparison of the present solution with Hencky's classical solution [29] and Kao and Perrone [53] nonlinear relaxation method solution is shown in Table 3.2. The central displacement as well as central and edge radial stresses obtained by the present method are in excellent agreement with the earlier reported results as shown in Table 3.2.

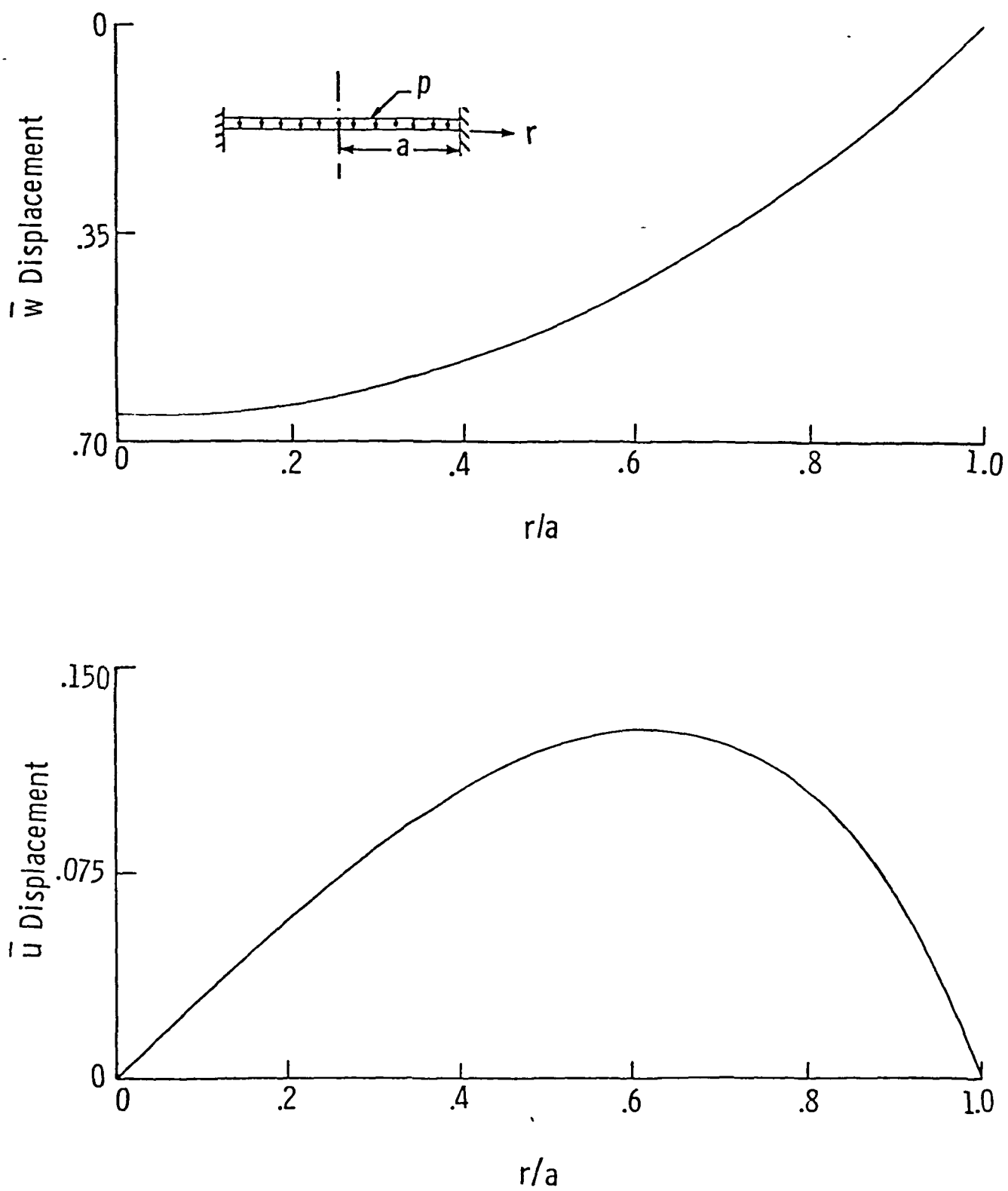


Fig. 3.8 Normalized Displacements for Uniformly Loaded Membrane

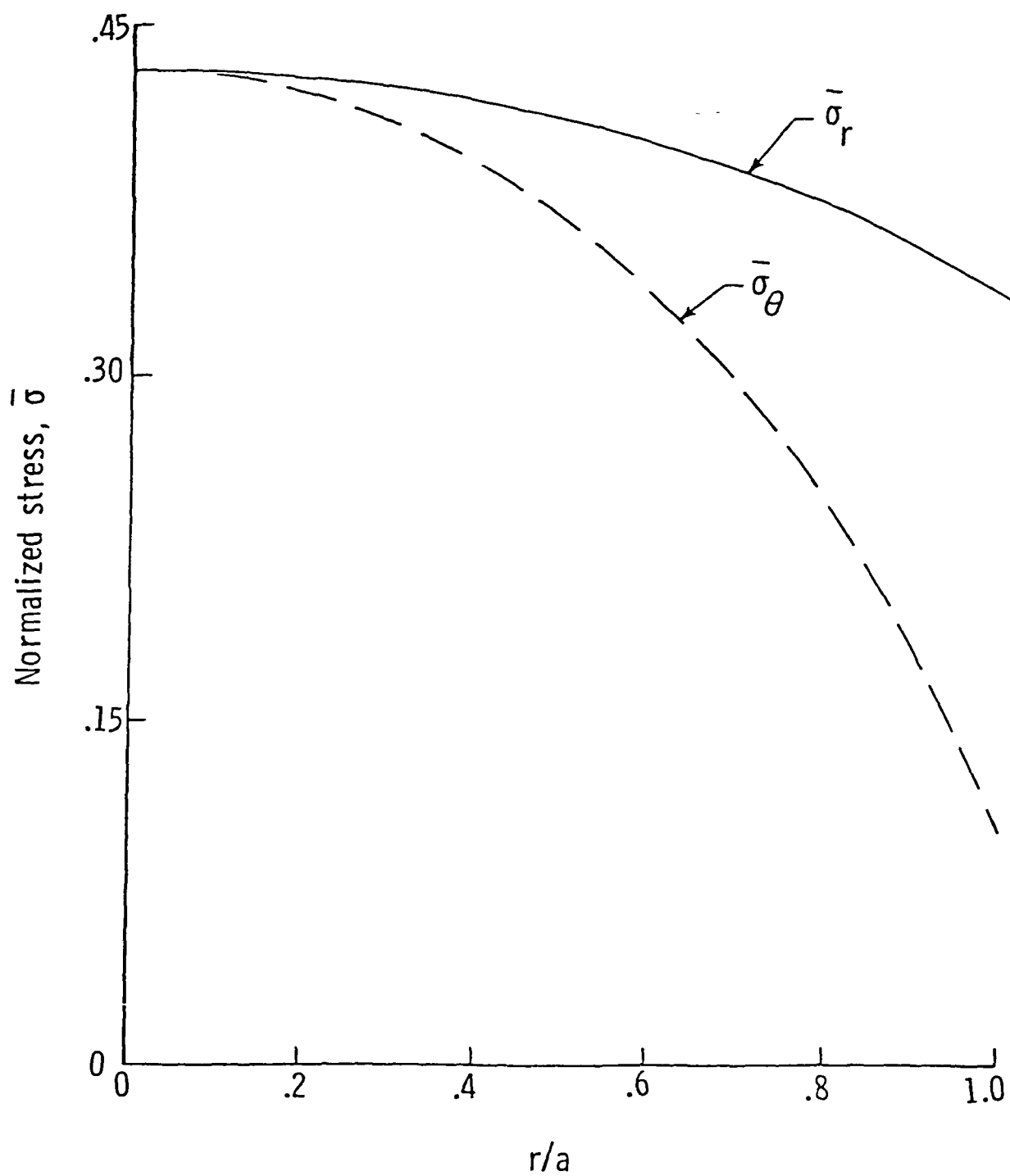


Fig. 3.9 Normalized Stresses for Uniformly Loaded Membrane

3.4.2 A Membrane With Uniformly Distributed Load Over the Inner Portion

The second example is that of a membrane with uniformly distributed load over an inner portion. A particular case of loading over the region $0 < \frac{r}{a} < 0.1$ was analyzed. In the corresponding solution, this loading was represented by setting the magnitude of loading terms p_1 through p_6 equal to unit values and terms p_7 through p_{60} equal to zero. Again using the governing Eq. (3.22) with the loading terms discussed before, the solution was obtained for stresses and displacements at each node. The corresponding values of \bar{u} and \bar{w} displacements and $\bar{\sigma}_r$ and $\bar{\sigma}_\theta$ stresses are shown in Figs. 3.10 and 3.11 respectively.

3.4.3 A Membrane With a Ring Load

The last problem considered here is one where the membrane carried a uniformly distributed ring load. As a specific case the ring load was assumed to be spread over the region $0.5 < \frac{r}{a} < 0.6$. Since loading was considered over the region $0.5 < \frac{r}{a} < 0.6$ in the corresponding solution, this loading was represented by setting the magnitude of loading terms p_1 through p_{30} equal to zero, p_{31} through p_{36} equal to unit values; and p_{37} through p_{60} equal to zero. Using these values in Eq. (3.22), the governing equation for the membrane with the ring load was solved by using the procedure outlined earlier.

The corresponding values of \bar{u} and \bar{w} displacements are presented in Fig. 3.12 and stresses $\bar{\sigma}_r$ and $\bar{\sigma}_\theta$ are presented in Fig. 3.13. Figure 3.12 shows that the transverse displacement w is constant up to the ring load and then starts decreasing and becomes zero at the clamped edge. In contrast, the radial displacement u is zero at the center,

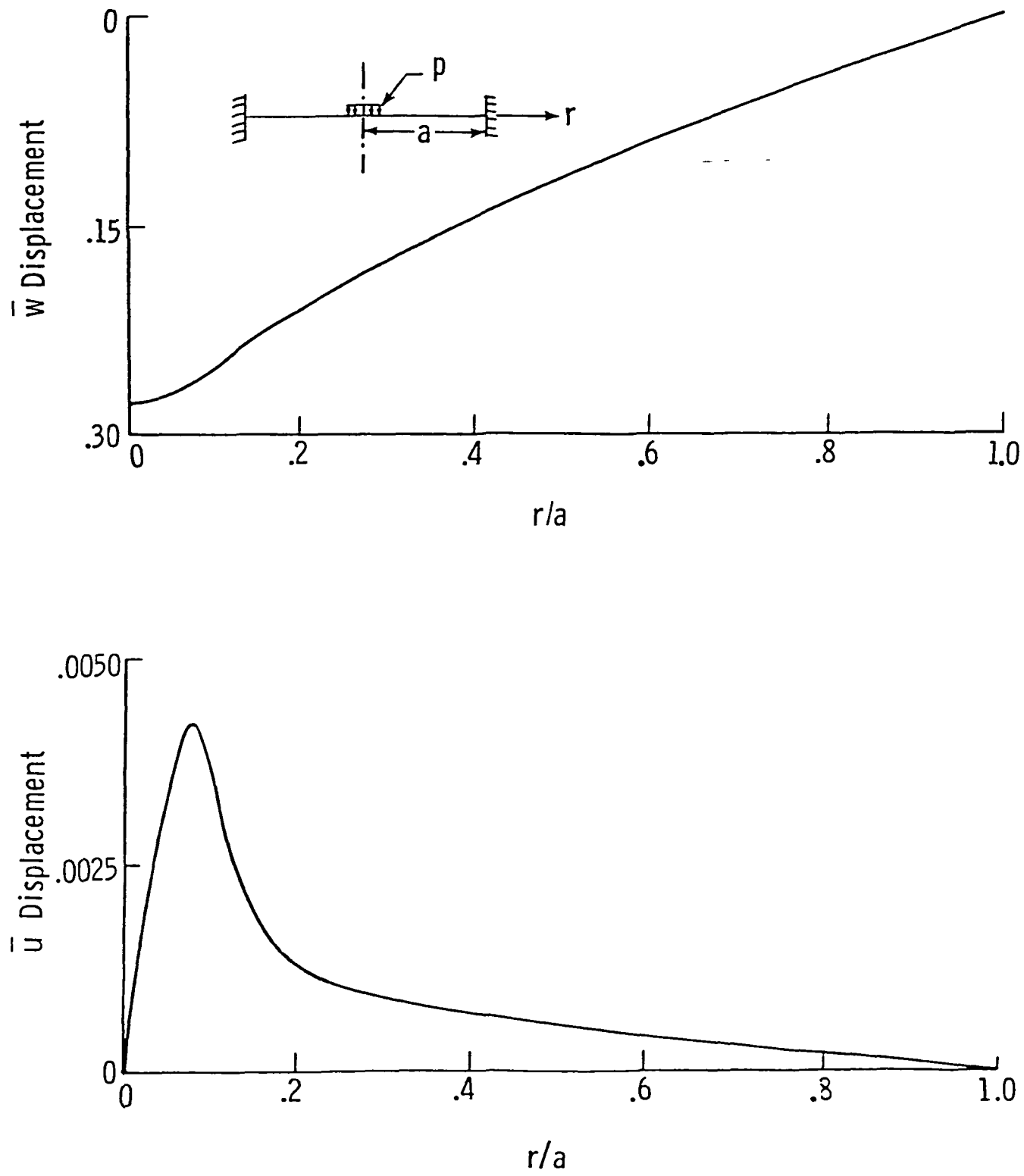


Fig. 3.10 Normalized Displacements in a Membrane Uniformly Loaded Over the Inner Prtion $0 \leq r/a \leq 0.1$

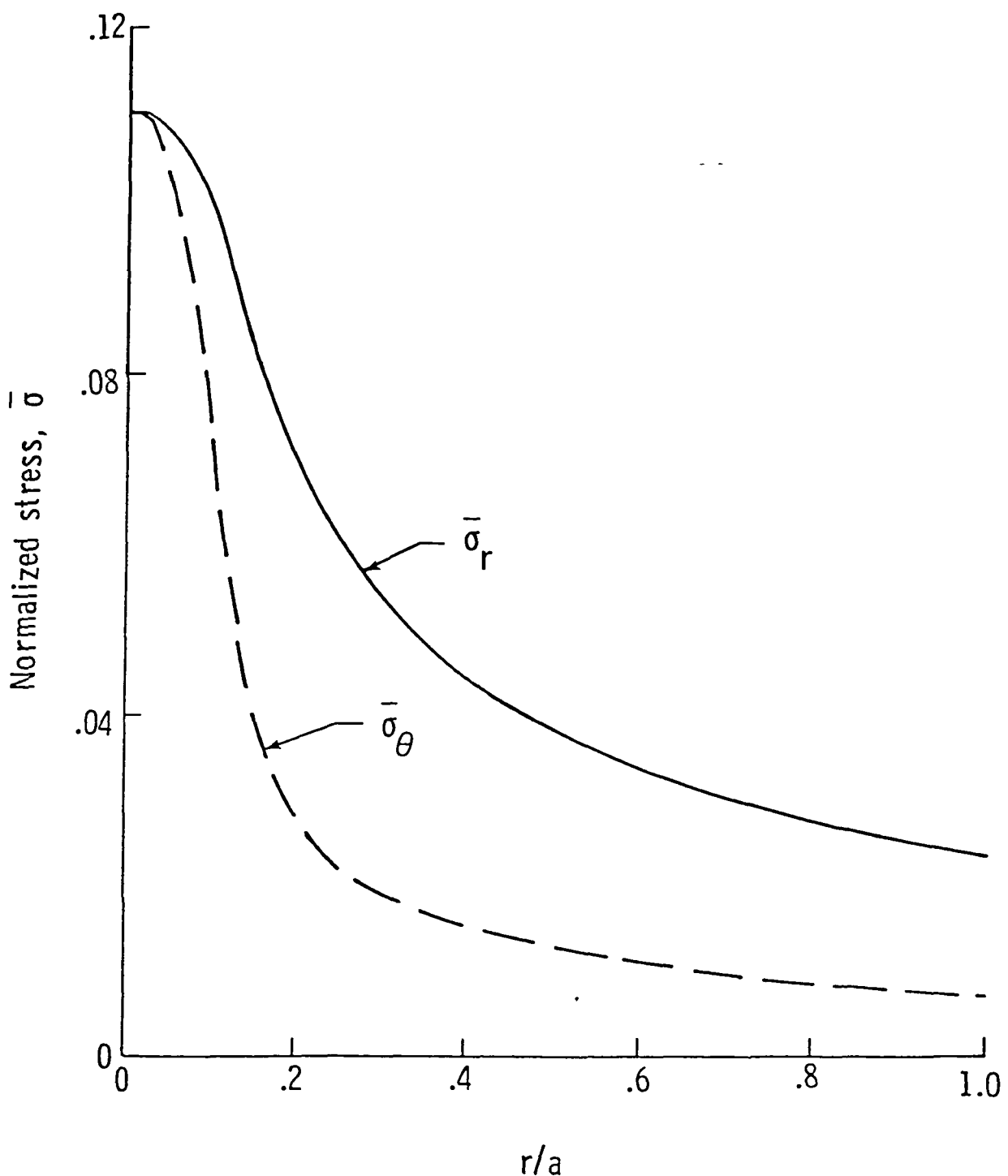


Fig. 3.11 Normalized Stresses in a Membrane Uniformly Loaded Over the Inner Portion $0 \leq r/a \leq 0.1$

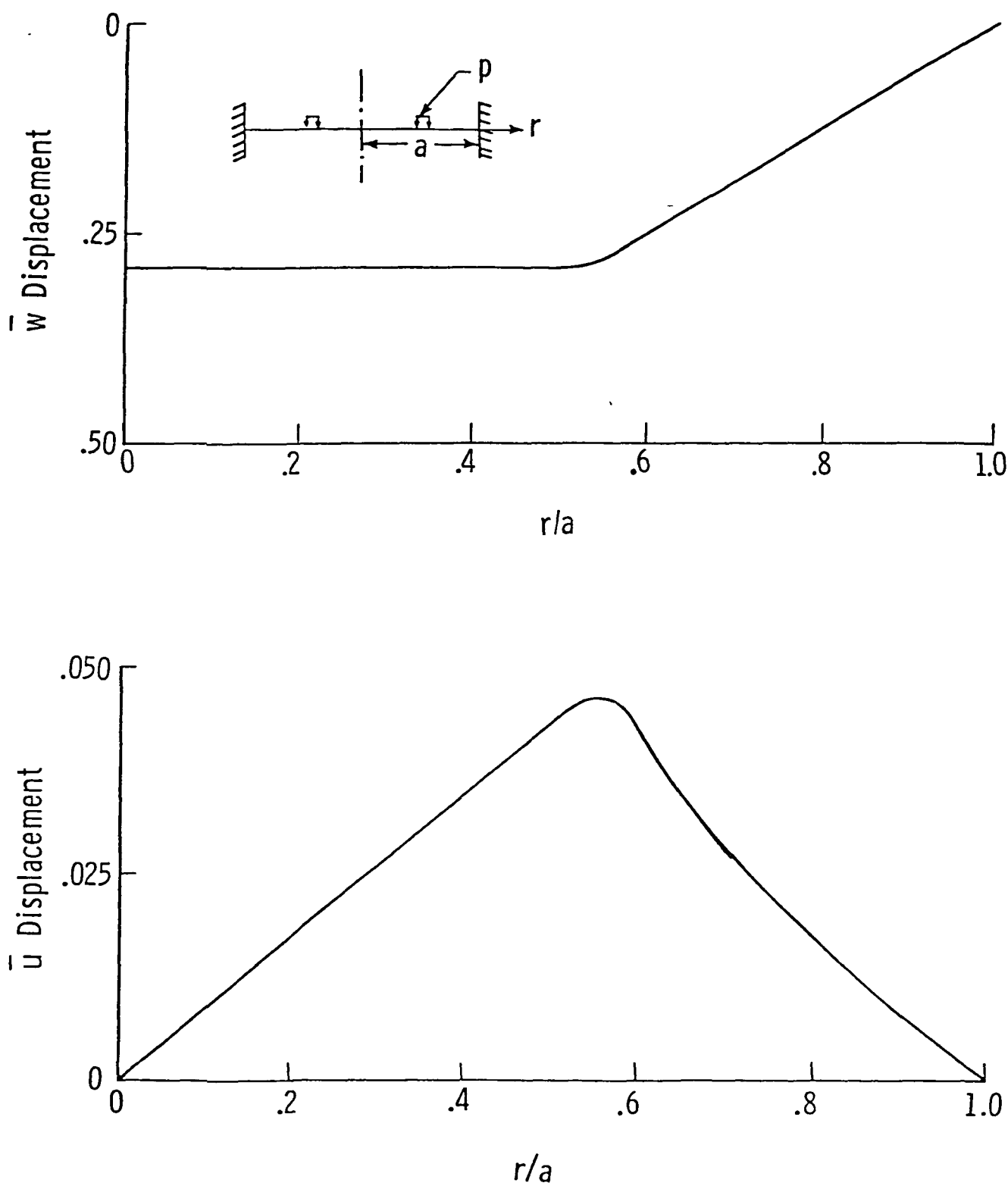


Fig. 3.12 Normalized Displacements in a Membrane with Ring Loading Over the Region $0.5 \leq r/a \leq 0.6$

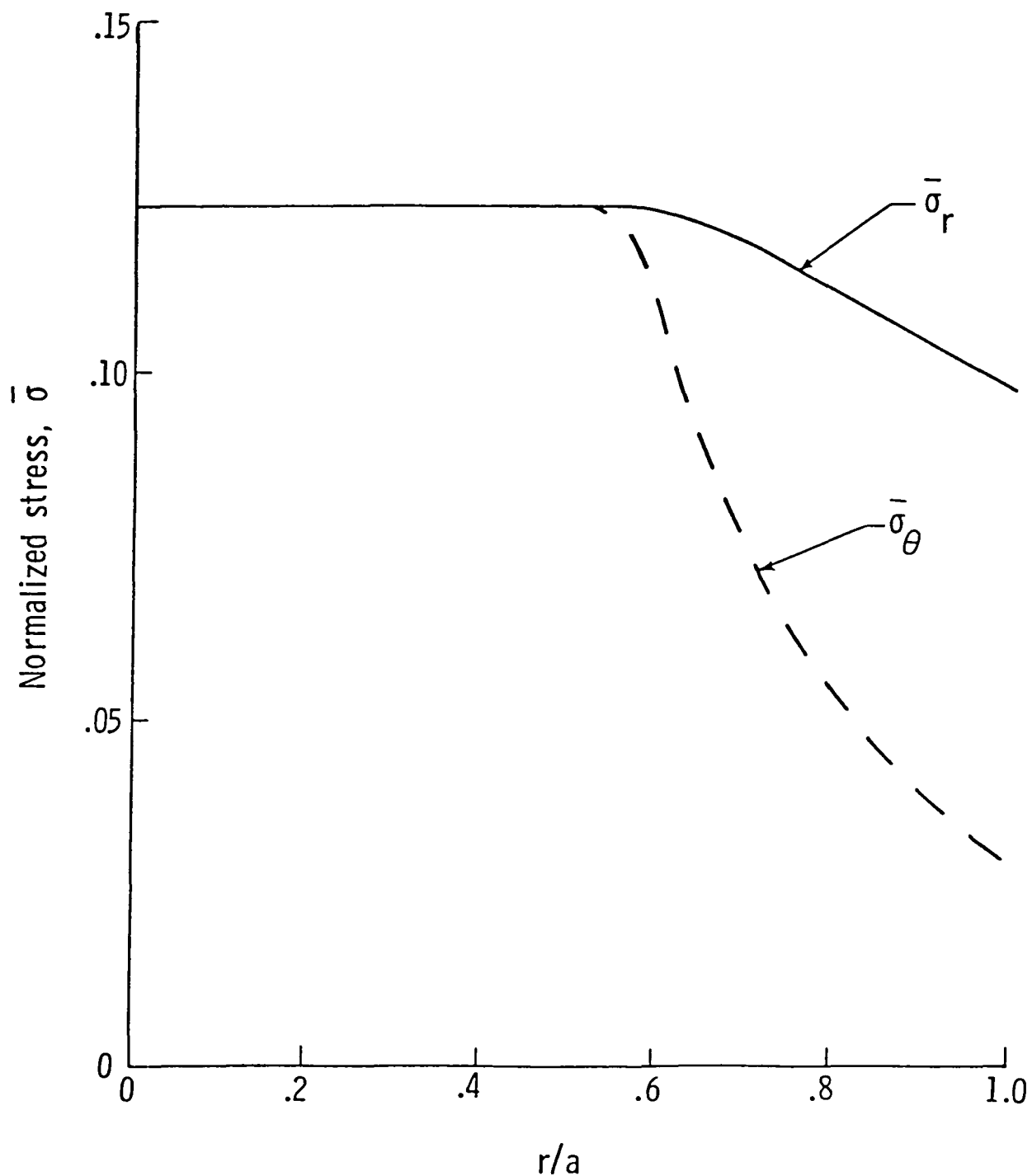


Fig. 3.13 Normalized Stresses in a Membrane with Ring Loading Over the Region $0.5 \leq r/a \leq 0.6$

increases gradually until it reaches the peak value in the loading region and then starts decreasing and becomes zero at the fixed edge. On the other hand, the normalized stresses $\bar{\sigma}_r$ and $\bar{\sigma}_\theta$ are of the identical magnitude in the unloaded region $0 < \frac{r}{a} < 0.5$ and then decrease for larger values of r .

3.5 Discussion

As pointed out earlier, when inplane and transverse displacements differ by large amounts a simultaneous method of solution presents difficulties. As the present method does not use \bar{u} and \bar{w} as parameters, rather uses a single parameter $\bar{\sigma}_r$ these difficulties are avoided. Therefore, it is interesting to compare the differences in magnitudes of \bar{u} and \bar{w} values for various problems analyzed. For a membrane with uniformly distributed load \bar{u} and \bar{w} are of the same magnitude (Fig. 3.8), whereas in the case of membrane loaded over an inner portion and for the ring loaded membrane, the displacements differ by two (Fig. 3.10) and one (Fig. 3.12) order of magnitude, respectively. Because \bar{u} and \bar{w} do not differ by large amounts in the case of uniformly loaded membrane, one would expect the simultaneous solution to be efficient and feasible. Indeed, it is so as demonstrated by Kao and Perrone [53]. Because \bar{u} and \bar{w} differ by large amounts for the arbitrarily loaded membranes, one would expect difficulties with simultaneous solution method. This may be the reason for the limited numerical solutions for these two loading cases. The present method on the other hand avoided these problems by using a governing equation in a single parameter, the radial stress. The present method shows good convergence characteristics for all the problems studied and converges

to the correct solution even when the initial values are unrealistically large or small. Therefore, the nonlinear governing equation in terms of the radial stress and the Newton-Raphson technique appear to be the ideal choice for large deflection problems of arbitrarily loaded membranes.

3.6 Concluding Remarks

In this chapter the quasi-isotropic circular laminate with only extensional stiffness but no shear and flexural stiffnesses were modeled as circular isotropic membranes. A single nonlinear differential equation which governs the response of these circular clamped isotropic membranes under arbitrary axisymmetric loading was developed. This nonlinear equation was solved by using the finite difference method in conjunction with Newton-Raphson method. The numerical studies on the large deflection membrane analysis show that the present method of analysis yields accurate solutions for inplane and transverse deflections and stresses for the arbitrarily axisymmetrically loaded circular membranes.

In the next chapter a plate-membrane coupling model, which uses the small deflection plate solution obtained in Chap. 2 and the large deflection membrane solution obtained in this chapter, is presented to predict the large deformation behavior of thin circular quasi-isotropic laminates under point loads.

Table 3.1 - Sensitivity of the Present Method of the Initial
Values of $\bar{\sigma}_r^a$

Initial $\bar{\sigma}_r$ values ^b	Number of iterations required for convergence		
	Uniform loading over the region		
	$0 < \frac{r}{a} < 1$	$0 < \frac{r}{a} < 0.1$	$0.5 < \frac{r}{a} < 0.6$
0.0001	25	22	23
0.001	20	16	17
0.01	14	10	11
0.1	8	8	5
1.0	9	19	15
10.0	20	27	26
100.0	31	41	37
Converged $\bar{\sigma}_r$ ($r = 0$)	0.4310	0.1104	0.1237
Converged $\bar{\sigma}_r$ ($r = a$)	0.3329	0.0235	0.0971

^aMembrane idealized with 60 regions

^bConstant radial stress $\bar{\sigma}_r$ was assumed at all 61 nodes.

Table 3.2 - Comparison of Normalized Displacements and Stresses
for Uniformly Loaded Membrane

	Central transverse deflection w at $r = 0$	Central radial stress $\bar{\sigma}_r$ at $r = 0$	Edge Radial stress $\bar{\sigma}_r$ at $r = a$
Hencky* (ref. 29)	0.6536	0.4310	0.3280
Kao and Perrone (ref. 53)	0.6541	0.4289	0.3306
Present Results	0.6534	0.4310	0.3329

*Values taken from reference 53.

Chapter 4

PLATE-MEMBRANE COUPLING MODEL

4.1 Introduction

In Chapters 2 and 3, numerical solution methods to analyze the small deformation behavior of circular quasi-isotropic plates and the large deflection behavior of circular isotropic membranes are described. In this chapter, a plate-membrane coupling model to study the large deformation behavior of clamped circular plates is developed. The model developed herein uses the plate and membrane solutions in conjunction with a coupling principle. A numerical solution method to analyze the clamped circular quasi-isotropic laminates under point load, using plate-membrane coupling model is presented.

4.2 Analysis

In the plate-membrane coupling model two different plate problems are analyzed. First, a thin plate with shear and flexural stiffnesses but no mid-plane extensional stiffness under point load is considered. The deflected shape of the plate is then obtained by using the classical small deformation theory. Second, a plate with mid-plane extensional stiffness, but no shear and flexural stiffnesses, i.e., a membrane is considered. The deformed plate shape obtained in the plate problem is used in the membrane problem. For this deformed shape membrane loads are calculated by using a nonlinear membrane theory. Large deformation

solutions of thin plates are then obtained by coupling these solution of plate and membrane problems. The details of the plate-membrane coupling model are given below:

4.2.1 Plate Configuration

Consider a clamped circular plate of thickness h and radius a , subjected to a central point load P as shown in Fig. 4.1. The plate is a quasi-isotropic laminate of T300/5208 graphite/epoxy material with stacking sequence $[45/0/-45/90]_S$ and material properties given in Table 2.1.

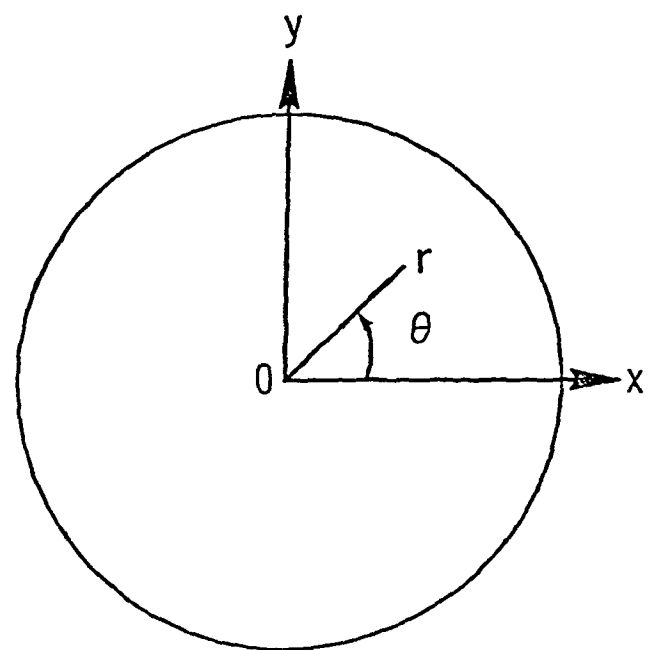
To analyze this quasi-isotropic clamped circular plate for large deformation behavior, first a circular plate with a prescribed central deflection w_0 is considered. The objective of the analysis is to determine the large deformation shape of the plate $w(r)$ and the central concentrated load P .

This problem as mentioned earlier, can be decomposed into two component problems: problem-1 is a plate with shear and flexural stiffnesses but no mid-plane extensional stiffness, problem-2 is a plate with mid-plane extensional stiffness but no shear and flexural stiffnesses, i.e., a membrane.

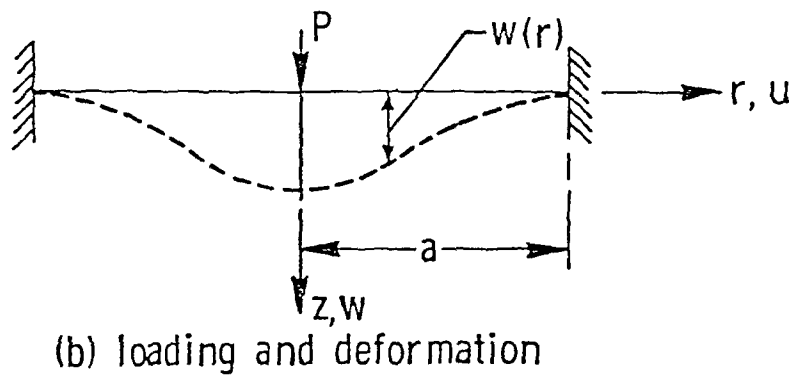
4.2.2 Problem-1: Plate Problem

In problem-1 the plate was assumed to be flexurally isotropic even though a quasi-isotropic plate is anisotropic in flexure. (This assumption was experimentally verified and will be discussed in detail in Chap. 6.)

From Chap. 2, the governing differential equation for axisym-



(a) circular plate



(b) loading and deformation

Fig. 4.1 Plate Configuration

metrical bending of a clamped circular plate subjected to arbitrary axisymmetric loading and undergoing small deformation is (Eq. (2.12))

$$\frac{d^3 w}{dr^3} + \frac{1}{r} \frac{d^2 w}{dr^2} - \frac{1}{r^2} \frac{dw}{dr} = \frac{Q(r)}{D_{eq}} \quad (4.1)$$

where $Q(r)$ is a shear force at any radius r and is given by (Eq. (2.13))

$$2 \pi r Q(r) = \int_0^r 2 \pi \xi p(\xi) d\xi \quad (4.2)$$

where $p(\xi)$ is the intensity of loading at any radius ξ .

In equation (4.1), D_{eq} is an equivalent flexural modulus for the quasi-isotropic laminate. As discussed in Chap. 2, the equivalent modulus D_{eq} was obtained by equating bending energies of the quasi-isotropic laminates and an equivalent isotropic plate. Equation (4.1) can be solved to obtain the deformed shape of the plate for a given intensity of load $p(r)$.

4.2.3 Problem-2: Membrane Problem

In problem-2, a plate with mid-plane extensional stiffness but no shear and flexural stiffness, i.e., a membrane is analyzed. Since the quasi-isotropic laminates are axially isotropic, the governing differential equations for these laminates are essentially the same as that for a circular isotropic membrane. From Chap. 3, the governing equations for the large deflections of circular isotropic membranes subjected to arbitrary axisymmetric loading are (Eqs. (3.18) and (3.19))

$$\frac{2r}{E_{eq}} \left[3 \frac{d\sigma_r}{dr} + r \frac{d^2 \sigma_r}{dr^2} \right] + \left(\frac{dw}{dr} \right)^2 = 0 \quad (4.3)$$

and

$$\left(\frac{dw}{dr}\right)^2 = \left[\frac{\int_0^r p(\xi) \xi d\xi}{r h \sigma_r}\right]^2 \quad (4.4)$$

where σ_r is the radial stress. If the displacement w is known, the rotation $(\frac{dw}{dr})$ is known and hence the radial stress can be determined by integrating Eq. (4.3). With this radial stress σ_r distribution, the loading $p(r)$ on the membrane can be determined by using equation (4.4).

4.2.4 Coupling of the Two Problems

The large deformation solution for quasi-isotropic clamped circular laminate with the prescribed central point deflection w_0 can be obtained by using the governing equations, Eqs. ((4.1)-(4.4)) and by the appropriate coupling of plate and membrane problems as shown in a flow chart of the Fig. 4.2. This procedure is outlined in Fig. 4.3, and is as follows:

The central point load P and the deformed shape $w(r)$ for a clamped circular plate were obtained by using the prescribed central deflection w_0 and the governing equation, Eq. (4.1) (steps 1 and 2 in Figs. 4.2 and 4.3). This deformed shape $w(r)$ was used in the membrane problem, to determine the membrane loads $p(r)$ (step 3 in Figs. 4.2 and 4.3). The loads which are equal in magnitude to $p(r)$ but opposite in direction, and the point load P were applied to the plate problem (step 4 in Figs. 4.2 and 4.3). For this new loading the new deformed shape $w'(r)$ of the clamped circular plate was obtained by solving the plate problem (step 5 in Figs. 4.2 and 4.3). Since the membrane loads $p(r)$ were applied in the opposite direction, this caused reduction of the central deflection of the plate by an amount Δw_0 (step 6 in Fig. 4.2).

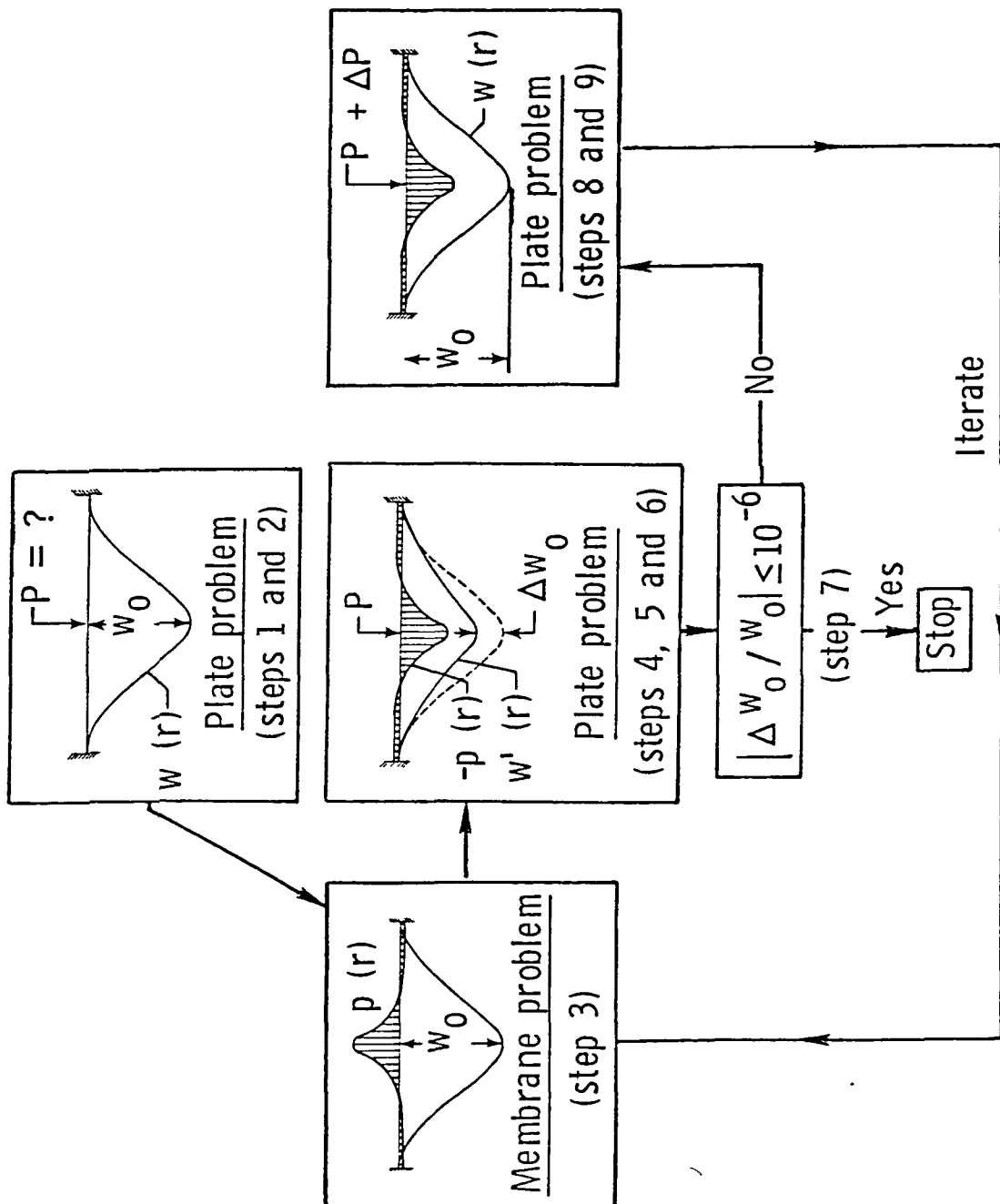


Fig. 4.2 Plate-Membrane Coupling Model

C-2

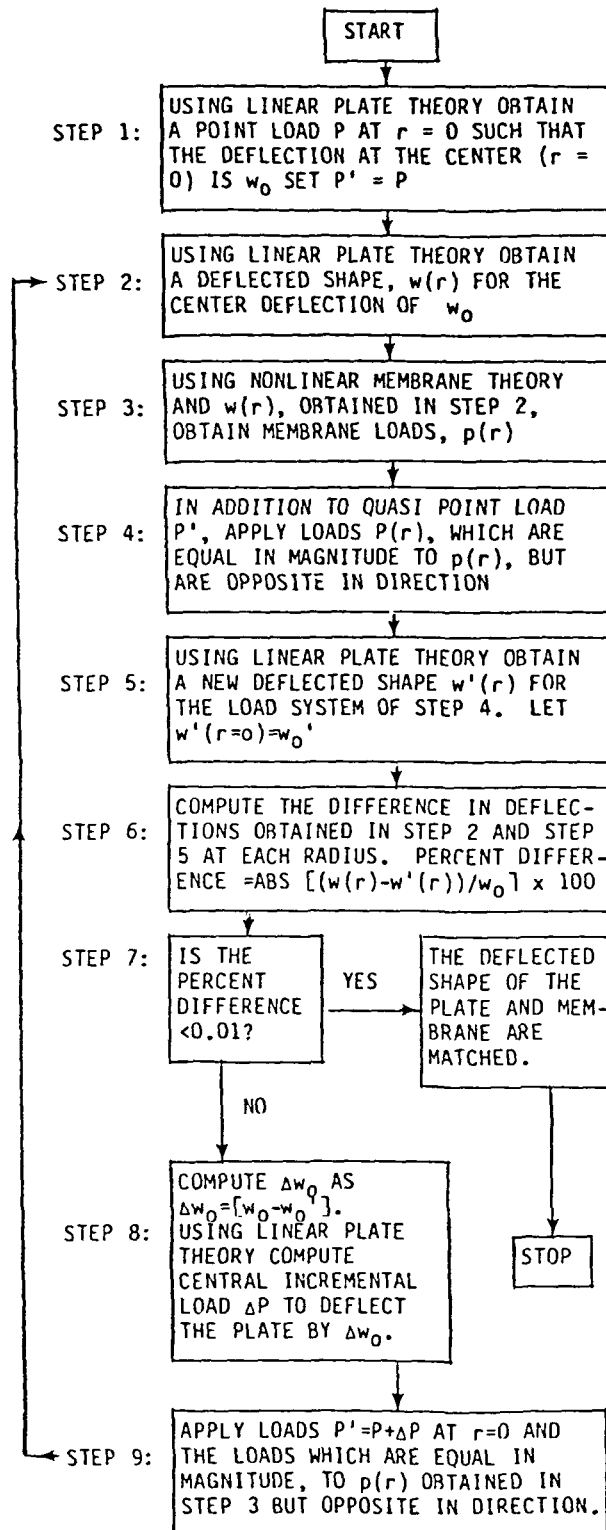


Fig. 4.3 Flow Chart for the Plate-Membrane Coupling Model

An incremental load ΔP is necessary to nullify the reduction of the central deflection, Δw_0 . The magnitude of the incremental load ΔP , is calculated by using Eq. (4.1) (step 8 of Fig. 4.3). This incremental load ΔP , together with the original point load P and the membrane loads which are equal in magnitude to $p(r)$ but opposite in the direction were applied to the plate problem (step 9 of Figs. 4.2 and 4.3). This load system yields a central deflection equal to w_0 , the original value. However, the new deflected shape $w(r)$, determined from Eq. (4.1) is in general different from the original deflection shape. This iterative procedure is repeated until the deflected shapes obtained in any two consecutive iterations are almost identical, i.e. step 7 in Fig. 4.3 is satisfied.

A complete solution can now be obtained by coupling the plate-membrane solutions. The coupled plate and the membrane are analogous to two coupled parallel springs, one with linear (plate) stiffness and other with a nonlinear (membrane) stiffness. If these springs undergo the same deflection w_0 then the unknown load P applied to this spring system is the sum of the loads carried in the two springs. Similarly in the present coupling model the deflected shapes of the plate and the membrane are identical and therefore the loads are additive.

When the deflected shapes obtained in any two consecutive iterations are nearly identical the plate carries a central point load and a distributive interactive load ($-p(r)$) and the matched membrane carries the opposite of distributive interactive loads $p(r)$. When the plate and membrane are coupled, interactive loads on the plate and membrane nullify each other and the total load is simply a single central point load on the plate. The complete plate-membrane solution

thus yields the large deflection shape of the plate and the magnitude of the central concentrated load, for a prescribed central deflection w_0 .

Instead of prescribing a central deflection w_0 , one could formulate the problem for a prescribed central point load P . The analysis procedure for this case is straight forward with minor differences and is as follows:

The problem as before, is also decomposed into two component problems. By using the center point load P in the plate problem, deflected shape $w(r)$ and the central deflection w_0 is obtained by using Eq. (4.1). Then steps 2 through 6 (Figs. 4.2 and 4.3) are repeated as done earlier. Since in step 4, the membrane load $p(r)$ is applied in the opposite direction, this causes a reduction in central deflection by Δw_0 (step 6 of Fig. 4.3). At this stage instead of incrementing the center point load P , the new membrane loads $p(r)$ are calculated by using the deformed shape $w'(r)$ obtained in step 5 (step 3 of Fig. 4.3). This procedure is repeated until the deflected shapes obtained in any two consecutive iterations are almost identical.

A complete solution can now be obtained by coupling the plate-membrane solutions. When the final plate and membrane solutions are coupled as before, the interactive loads on the plate and membrane nullify each other and the original prescribed central point load is left on the plate. The corresponding matched central deflection w_0 , and the deflection shape $w(r)$, are the large deformation solutions of the clamped circular plate subjected to a prescribed central point load.

The above procedure, although presented for a central concentrated load, can be applied in a similar manner to obtain the large deformation

solutions for arbitrarily axisymmetrically loaded clamped circular plates. If, on the other hand, the large deformation shape of the plate is known, it can be used in the linear plate theory to calculate the plate loads, and in the nonlinear membrane theory to calculate the membrane loads. The sum of these two loads gives the complete large deformation solution.

4.3 Solution Method

The plate governing equation, Eq. (4.1) for the deflection w , was solved by using finite difference method as described in Chap. 2. The ordinary differential Eq. (4.1), was replaced by a set of linear algebraic equations using finite difference quantities. These linear algebraic equations were solved numerically, to obtain rotations and displacements. The nonlinear governing equations, Eqs. (4.2) and (4.3) were replaced by a set of nonlinear algebraic equations using finite difference quantities. These nonlinear equations were solved by using a Newton-Raphson method in conjunction with the finite difference method, as described in Chap.3.

Using these plate and membrane solutions in conjunction with the plate-membrane coupling model discussed before, the large deformation shapes for the clamped circular quasi-isotropic laminates were obtained.

From the plate-membrane coupling model it was observed that as plate central deflection to plate thickness ratio increases, the number of iterations required to obtain the large deformation solution increases. Table 4.1 presents the number of iterations required to obtain the large deformation solution of the clamped circular quasi-isotropic laminates under point loads for $(\frac{w_0}{h})$ ratios ranging from 0.5 to 2.0.

4.4 Results and Discussion

In this section analytical deflected shapes obtained with the plate-membrane coupling model, for the central deflection to plate thickness ratios ($\frac{w_0}{h}$) ranging from 0.5 to 2.0 are presented. These analytical deflected shapes obtained by using the plate-membrane coupling model are compared with the deflected shapes obtained by using the classical solution [27]. Load-displacement curve obtained by using the plate-membrane coupling model is compared with the classical solution [27]. Figures 4.4 and 4.5 show the analytical deflected shapes obtained by using the plate-membrane coupling model; for ($\frac{w_0}{h}$) ratios of 0.5 to 1.0, and 1.5 and 2.0. Figures 4.4 and 4.5 indicate that the functional form of the deformed shapes of the plate is different for various ($\frac{w_0}{h}$) ratios.

To compare the plate-membrane coupling analysis, the classical solution [27] based on the energy method was considered. Appendix B presents the large deformation classical solution based on the energy method for a clamped circular plate subjected to the center point load P. The classical solution assumes that the functional form of the deformed shape of the plate is identical to the functional form of the deformed shape of the plate determined by the small deflection solution. Thus as per the classical solution [27], the large deformed shape of a clamped circular plate under center point load is given as:

$$w(r) = w_0 \left[1 - \left(\frac{r^2}{a^2} \right) + 2 \left(\frac{r^2}{a^2} \right) \ln \left(\frac{r}{a} \right) \right] \quad (4.5)$$

The transverse displacements w obtained by using the plate-membrane coupling model and the classical solution (Eq. (4.5)) for

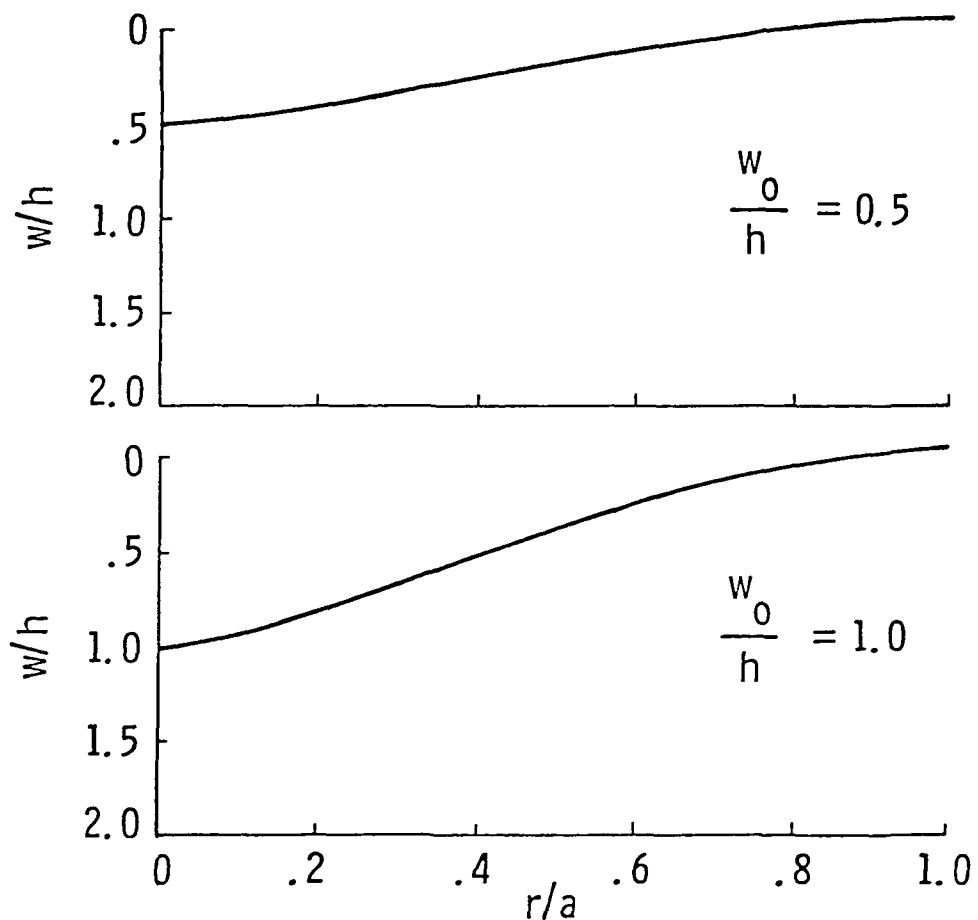


Fig. 4.4 Deflected Shapes for the Quasi-Isotropic Circular Plate Under Point Loads for $w_0/h = 0.5$ and 1.0

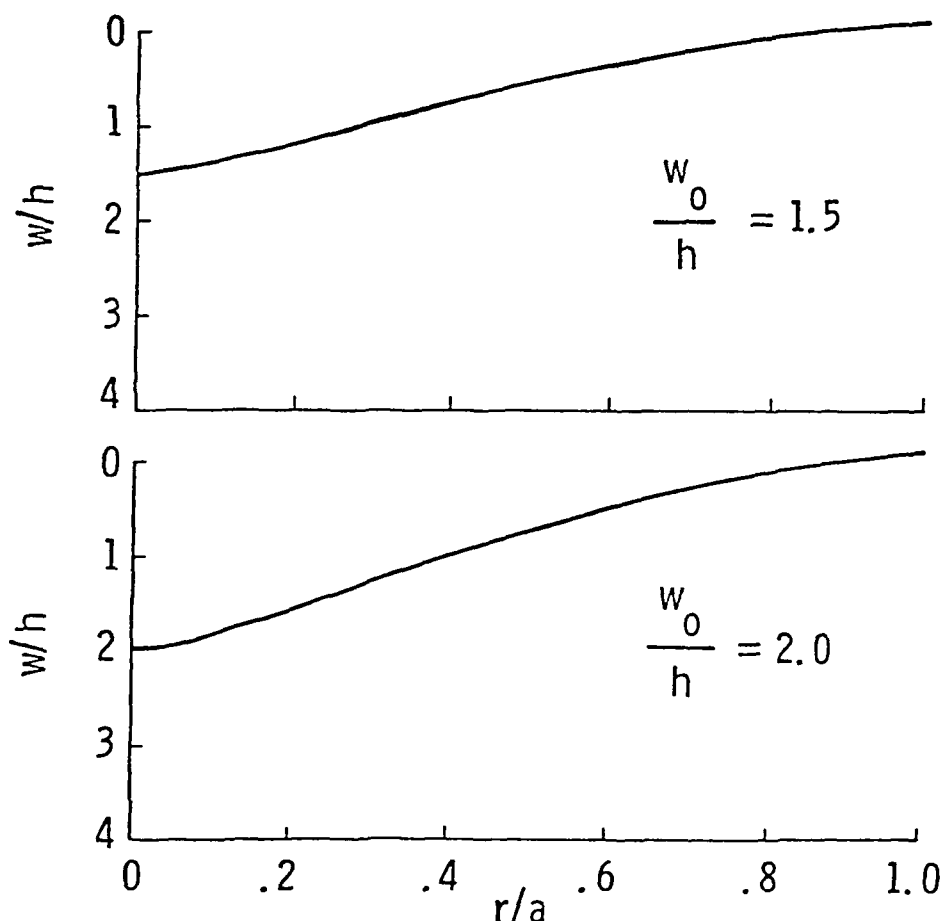


Fig. 4.5 Deflected Shapes for the Quasi-Isotropic Circular Plate Under Point Loads for $w_0/h = 1.5$ and 2.0

various $(\frac{w_0}{h})$ ratios ranging from 0.5 to 2.0 are presented in Table 4.2. The results obtained by using the plate-membrane coupling model show that the functional form of the deflected shapes for various $(\frac{w_0}{h})$ ratios is different. In contrast, as mentioned earlier the classical solution [27] based on energy method, assumes that the functional form of the deflected shape of the plate is identical for all $(\frac{w_0}{h})$ ratios. The deflected shapes obtained by using the plate-membrane coupling model are compared with those obtained by using the classical solution [27].

Figure 4.6 presents the percentage errors, in the deflected shape of the classical solution relative to the present solution, at various radii for $(\frac{w_0}{h})$ ratio of 2.0. It is observed that the maximum error is about 4 percent and occurs at $(\frac{r}{a}) = 0.233$. Although relative errors in the displacements are small, these errors get magnified if the curvatures obtained by the plate-membrane coupling model and the classical solution are compared. Figure 4.7 compares the curvatures obtained with the plate-membrane coupling model and the classical solution, for $(\frac{w_0}{h})$ ratio of 2.0. Figure 4.7 shows that the plate-membrane coupling model predicts higher values of curvatures than those obtained by using the classical solution up to $(\frac{r}{a})$ ratio of 0.4 and beyond $(\frac{r}{a}) = 0.9$. However, in the range $0.4 < \frac{r}{a} < 0.9$, the classical solution predicts higher values of curvatures. Since stresses are proportional to the curvatures even small differences in the curvature result in significant errors in stress predictions in the plate undergoing large deformation.

In the plate-membrane coupling model, another important point that was noticed was the movement of the radius of inflection (radius at which curvature is zero), as a function of the central deflection to the

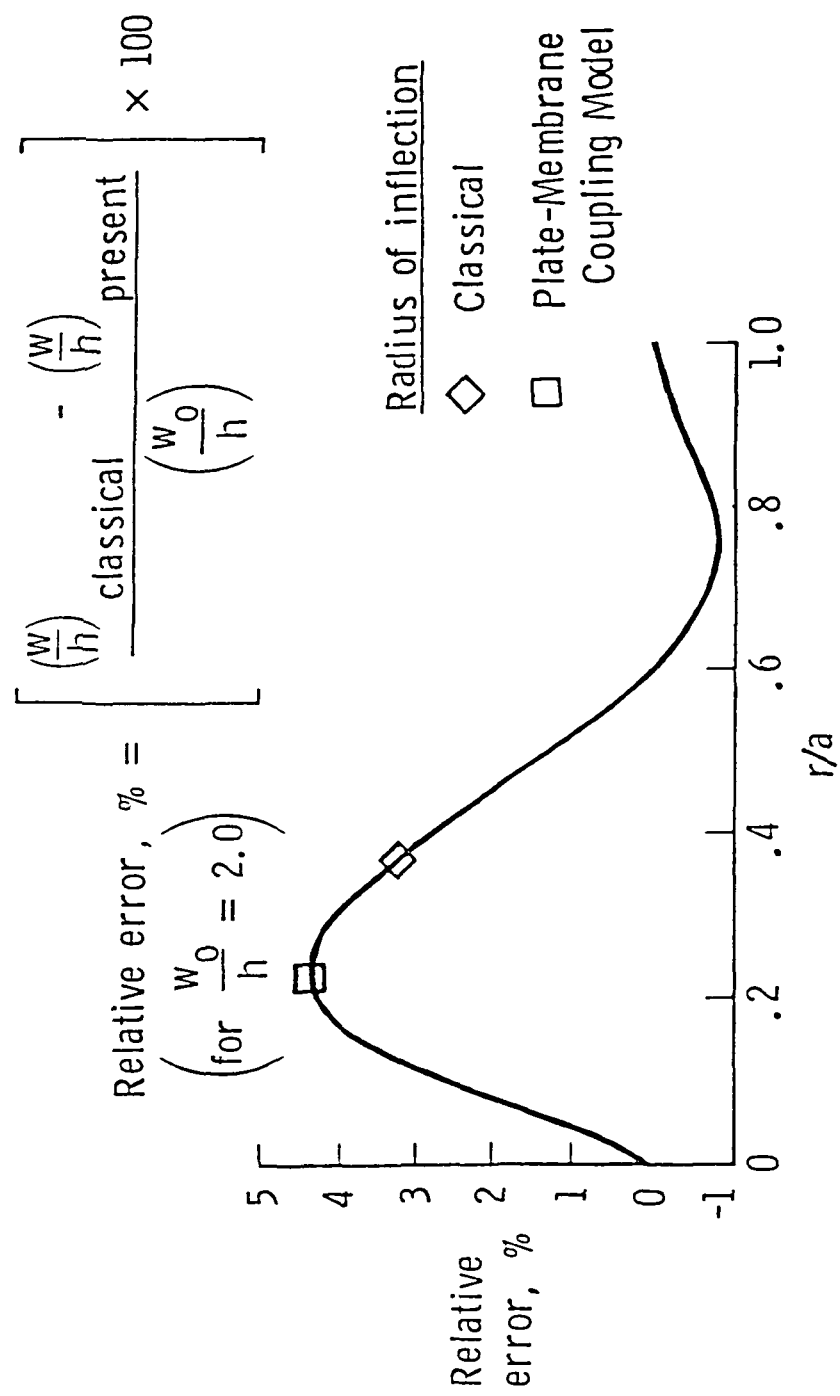


Fig. 4.6 Percentage Errors in the Classical Solution Relative to the Plate-Membrane Coupling Model Solution

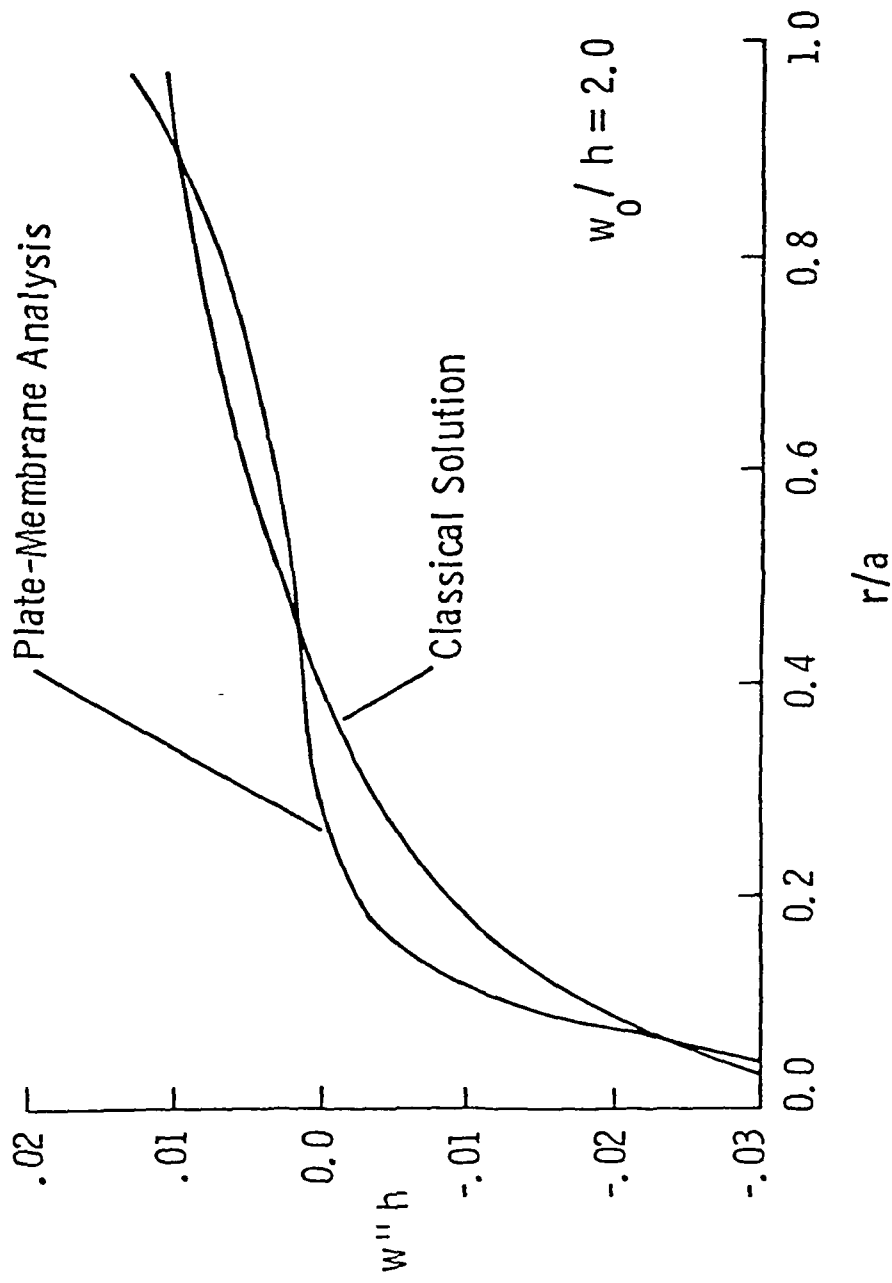


Fig. 4.7 Curvature Comparison for the Quasi-Isotropic Circular Plate Under Point Load

plate thickness ratios $(\frac{w_0}{h})$. The classical solution [27], assumes that the functional form of the deformed shape is identical for all $(\frac{w_0}{h})$ ratios, hence the radius of inflection shows no movement with the change in ratios and is located at $(\frac{r}{a}) = 0.3678$. (The detail derivation for the radius of inflection is presented in Appendix C.) The plate-membrane coupling model on the other hand does not make any assumption on the deformed shape of the plate and hence on the radius of inflection. The deformed shape and the radius of inflection are obtained as part of the solutions. Figure 4.8 shows the movement of the radius of inflection with the change in the central deflection to the plate thickness ratios $(\frac{w_0}{h})$. The symbols in Fig. 4.8 show the position of the point of inflection for different values of $(\frac{w_0}{h})$. For increasing central deflection the point of inflection moves toward the center of the plate ($r = 0$). The inward movement of the point of inflection with increasing $(\frac{w_0}{h})$ ratio occurs, since, as $(\frac{w_0}{h})$ ratio increases, the plate behaves more like a membrane than a flexural plate. That is as $(\frac{w_0}{h})$ ratio increases, the external load is equilibrated more and more in membrane action than in flexural action.

Figure 4.9 presents a comparison between the load-displacement curves obtained by using the plate-membrane coupling model and the classical solution [27]. This figure indicates that the classical solution based on the energy method predicts the load-displacement behavior accurately up to $(\frac{w_0}{h})$ ratio of 1.0. However for higher values of $(\frac{w_0}{h})$ ratios the classical solution yields lower displacements than the plate-membrane coupling solution.

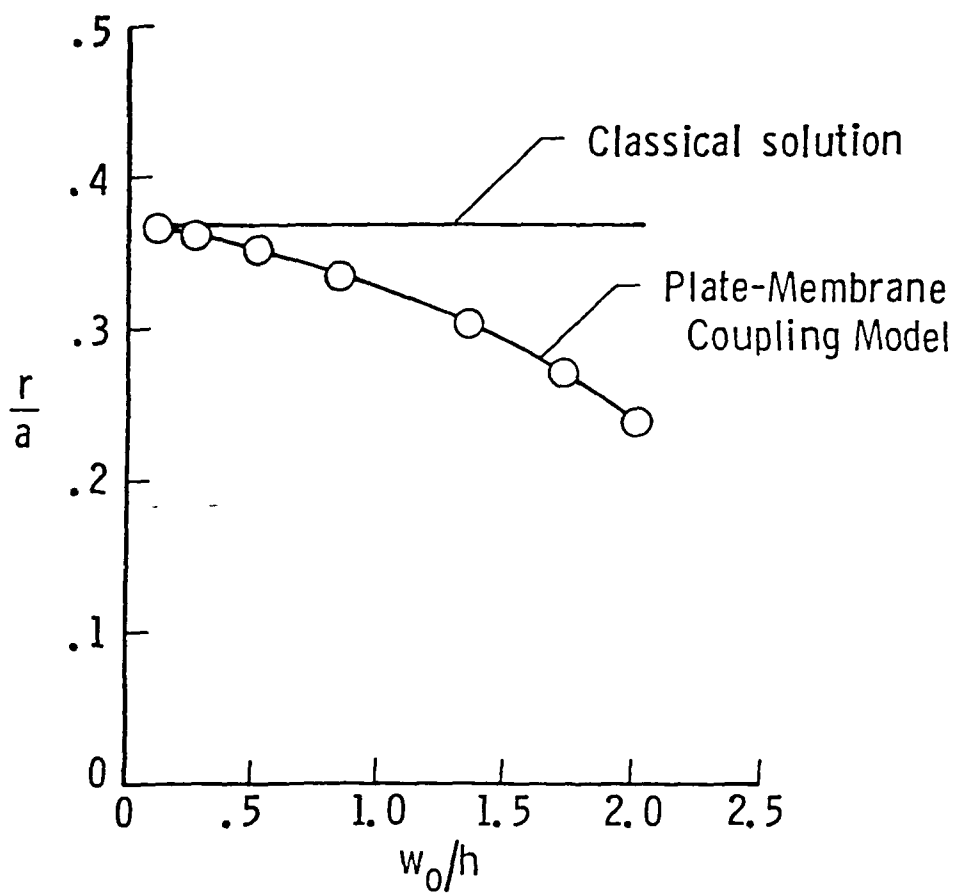


Fig. 4.8 Movement of Radius of Inflection as a Function of Center Deflection

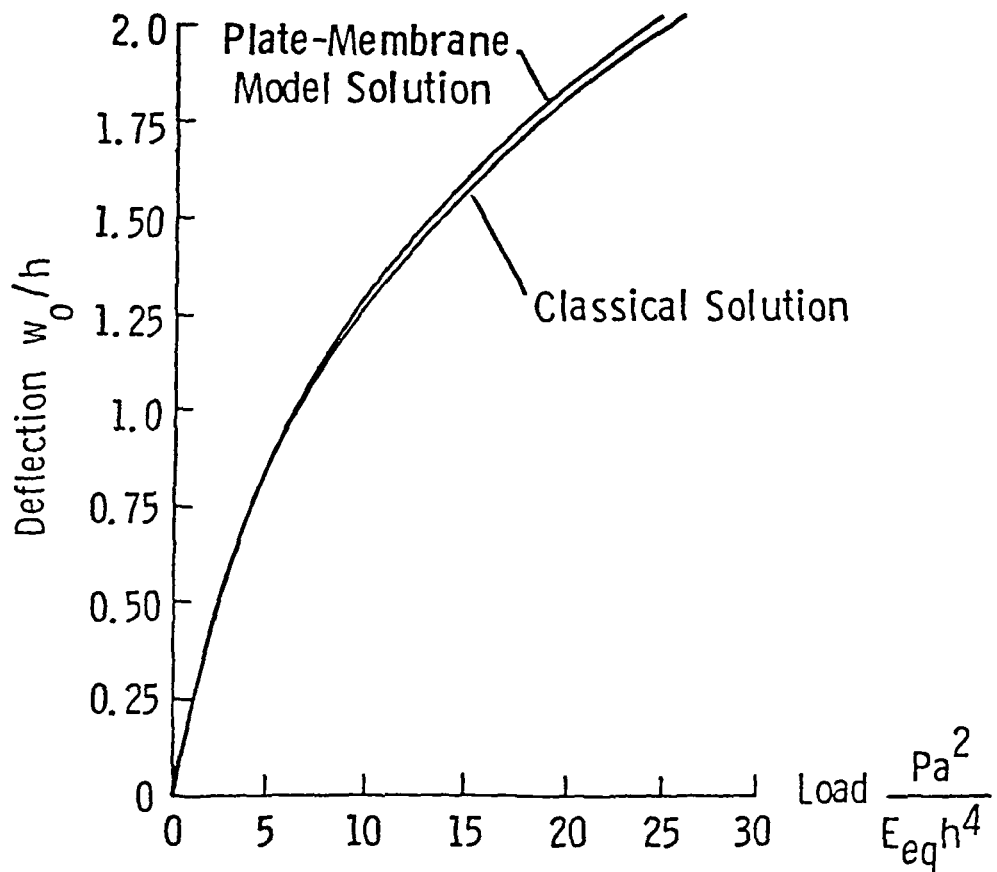


Fig. 4.9 Load-Deflection Curve Comparison

4.5 Concluding Remarks

In this chapter circular quasi-isotropic composite plates were analyzed to study the large deformation behavior under point loads. A plate-membrane coupling model was formulated and solved numerically to obtain the large deformation shapes for thin circular composite laminates under the point loads. These large-deformation shapes were compared with the large deformation shapes obtained by using the classical solution [27] which assumes that the functional form of the deformed shape of the plate is identical to the functional form of the deformed shape of the plate determined by the small deflection plate solution. The comparison shows that the functional form of the deformed shape of the plate undergoing large deformations is different from the small deflection plate solution in that the deformed shape is a function of the center point displacements and thus is different for different load levels. The classical solution and the plate membrane coupling solution are in good agreement up to the central deflection-to-plate thickness ratio of 1.0. For higher values of the center deflection-to-plate thickness ratios the classical solution yields lower displacements than the plate-membrane coupling solution. This plate membrane coupling model is experimentally verified in Chap. 6.

Table 4.1 - Number of Iterations to Obtain Large Deflection
Solution of a Clamped Circular Plate Under Central
Concentrated Load Using the Plate-Membrane Coupling
Model.

Plate center deflection to thickness ratio ($\frac{w_0}{h}$)	Number of iterations
0.5	9
1.0	11
1.5	14
2.0	21

Table 4.2(a) - Comparison of the Transverse Displacements w
 Obtained by Using the Plate-Membrane Model and the
 Classical Solution for $(\frac{w_0}{h})$ Ratios of 0.5 and 1.0.

r/a		Classical Solution	Plate-Membrane Coupling Model
$(\frac{w_0}{h}) = 0.5$	0.0	0.50000	0.50000
	0.1	0.47197	0.46764
	0.2	0.41562	0.40842
	0.3	0.34664	0.33791
	0.4	0.27339	0.26484
	0.5	0.20171	0.20311
	0.6	0.13610	0.13506
	0.7	0.08023	0.07762
	0.8	0.03719	0.03828
	0.9	0.00966	0.01001
$(\frac{w_0}{h}) = 1.0$	1.0	0.00000	0.00000
	0.0	1.00000	1.00000
	0.1	0.94394	0.93050
	0.2	0.83124	0.80831
	0.3	0.69328	0.66745
	0.4	0.54678	0.52491
	0.5	0.40342	0.39392
	0.6	0.27220	0.27028
	0.7	0.16046	0.16570
	0.8	0.07438	0.07719
	0.9	0.01932	0.02074
	1.0	0.00000	0.00000

Table 4.2(b) - Comparison of the Transverse Displacements w
 Obtained by Using the Plate-Membrane Model and the
 Classical Solution for $(\frac{w_0}{h})$ Ratios of 1.5 and 2.0.

r/a	Classical Solution	Plate-Membrane Coupling Model
$(\frac{w_0}{h}) = 1.5$	1.50000	1.50000
	1.41592	1.38595
	1.24686	1.19548
	1.03992	0.98512
	0.82018	0.78421
	0.60513	0.58841
	0.40830	0.40245
	0.24068	0.25309
	0.11156	0.12140
	0.02897	0.03286
1.0	0.00000	0.00000
$(\frac{w_0}{h}) = 2.0$	2.00000	2.00000
	1.88789	1.83399
	1.66248	1.57111
	1.38656	1.29297
	1.09357	1.02026
	0.80685	0.77129
	0.54441	0.53813
	0.32091	0.34512
	0.14875	0.16870
	0.03863	0.04561
1.0	0.00000	0.00000

Chapter 5

FINITE ELEMENT MODEL

5.1 Introduction

In the previous chapter, a plate-membrane coupling model was presented to obtain the large deformation behavior of circular quasi-isotropic laminates under point loads. To verify the plate-membrane coupling model, a finite element formulation, which uses appropriate linearization of strain-displacement relations [36] is developed and presented in this chapter. The formulation is based on a variational technique and uses the principle of minimum potential energy [28]. As pointed out in Chap. 1, several investigators [36-44] used a linearization technique, to study the geometrically nonlinear circular plate problems. However, earlier investigators ignored the membrane effects due to mid plane stretching. In this chapter, the membrane effects due to the mid-plane stretching are incorporated in the finite element model. This model is used to analyze the large deformation behavior of the circular quasi-isotropic laminates under point loads. The results from this model are compared with the results from the plate-membrane coupling model.

5.2 Finite Element Method

The basis of the finite element is the representation of a body or structure by an assemblage of subdivisions (finite elements). Simple functions are then chosen to approximate the distribution or variation

of the actual displacements over each element. These functions are usually referred to as shape functions. A variational principle, such as the principle of minimum potential energy, is then employed to obtain the set of equilibrium equations for each element. The equilibrium equations for the entire body are then obtained by combining the equations of the individual elements. The equations are modified for the given force or displacement boundary conditions and then solved to obtain the unknown displacements.

Mathematically, the finite element representation of continuum strongly resembles the Ritz method [28], in which the displacements of the plate are approximated by the sum of the functions, each multiplied by an unknown constant. These unknowns are determined from the minimum potential energy theorem. While using the Ritz method, the assumed series expression describes the total displacement field of the entire plate, in the finite element method individual displacement patterns for each element are assumed. The entire displacement field of the plate can be approximated piecewise. The total potential of the plate, obtained from the sum of the total potentials of the individual elements, has a stationary value when the node points are in equilibrium. This conditions leads to minimization of the total potential of the structural system, which, in turn, yields the displacement field corresponding to its equilibrium condition.

The application of the finite element method to obtain the large deformation solution for the quasi-isotropic circular plates under point loads is presented in following sections.

5.3 Plate Configuration

As before the plate configuration used was that of a quasi-isotropic circular plate with a concentrated load at the center. The plate is assumed flexurally isotropic and the equivalent flexural modulus D_{eq} of the plate is computed as described in Chap. 2. With this assumption of the flexural isotropy the problem of a circular quasi-isotropic plate subjected to a central point load reduces to an axisymmetric problem. This problem is then analyzed by the finite element method as shown in the following sections.

5.3.1 Strain-Displacement Relations

For the axisymmetrically loaded circular plate the deflection surface is axisymmetrical. Due to the symmetry the shearing stresses $\tau_{r\theta}$ are zero. Also from the basic assumptions of the plate theory (Chap. 2), shearing stresses τ_{rz} and normal stresses σ_z are zero.

For the circular plate undergoing large deformations, the radial and tangential bending strains at any distance z from the middle surface are,

$$\begin{Bmatrix} \epsilon_r \\ \epsilon_\theta \end{Bmatrix}_{\text{bending}} = z \begin{Bmatrix} -\frac{d^2 w}{dr^2} \\ -\frac{1}{r} \frac{dw}{dr} \end{Bmatrix} = z \begin{Bmatrix} \epsilon_r \\ \epsilon_\theta \end{Bmatrix}_b \quad (5.1)$$

and the membrane strain-displacement matrix is (Eqs. (3.3) and (3.4))

$$\begin{Bmatrix} \epsilon_r \\ \epsilon_\theta \end{Bmatrix}_{\text{membrane}} = \begin{Bmatrix} \frac{du}{dr} + \frac{1}{Z} \left(\frac{dw}{dr} \right)^2 \\ \frac{u}{r} \end{Bmatrix} = \begin{Bmatrix} \epsilon_r \\ \epsilon_\theta \end{Bmatrix}_m \quad (5.2)$$

Therefore the total radial and tangential strain-displacement

matrix is

$$\begin{Bmatrix} \epsilon_r \\ \epsilon_\theta \end{Bmatrix} = z \begin{Bmatrix} \epsilon_r \\ \epsilon_\theta \end{Bmatrix}_b + \begin{Bmatrix} \epsilon_r \\ \epsilon_\theta \end{Bmatrix}_m \quad (5.3)$$

or in concise form

$$\{\epsilon\} = z \{\epsilon_b\} + \{\epsilon_m\} \quad (5.4)$$

The stresses and strains are related by a material properties matrix, $[H]$, forming the following constitutive equation

$$\{\sigma\} = [H] \{\epsilon\} \quad (5.5)$$

where

$$[H] = \frac{E_{eq}}{(1-\nu_{eq})^2} \begin{bmatrix} 1 & \nu_{eq} \\ \nu_{eq} & 1 \end{bmatrix} \quad (5.6)$$

where E_{eq} and ν_{eq} are the equivalent Young's modulus and Poisson's ratio for the quasi-isotropic plate and were calculated by using the technique presented in Chap. 2.

5.4 The Axisymmetric Finite Element

An axisymmetric finite element in the form of a ring of constant cross section is shown in Fig. 5.1. The node points of such an element are in fact nodal circles, and the volume of such an element is dependent on both its cross-sectional area and the radii of these nodal circles.

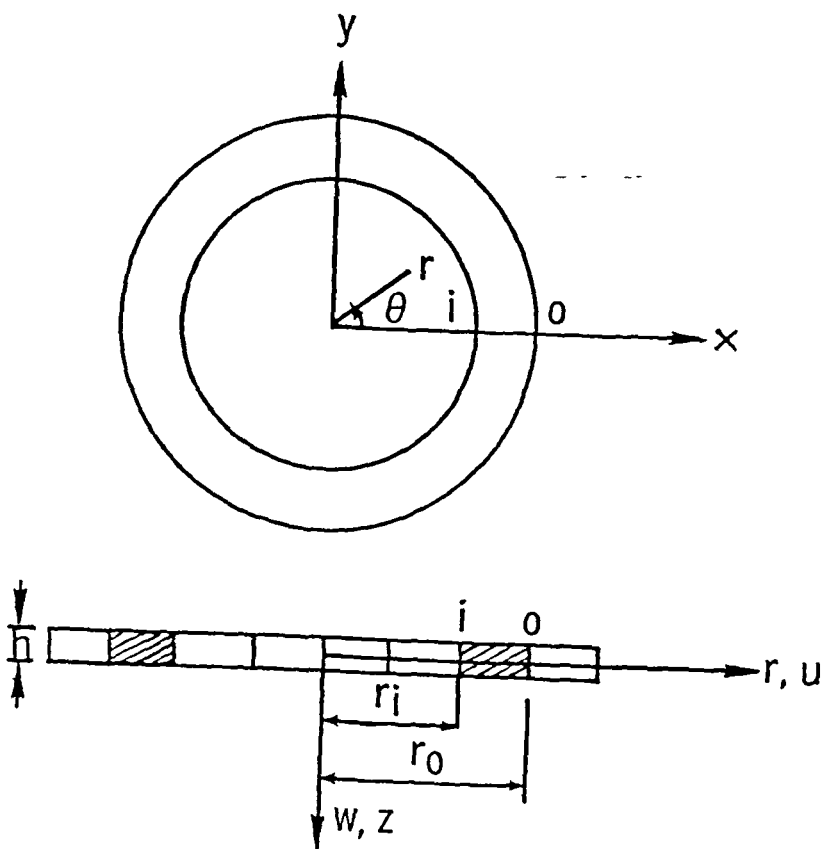


Fig. 5.1 Axisymmetric Element

A convenient approach for derivation of the finite element governing expressions is based on the principle of minimum potential energy. Consider a circular plate discretized into n number of axisymmetric elements. Each element is of a constant thickness h , with r_i and r_o as inner and outer radii (Fig. 5.1). Let U_e be the strain energy of the axisymmetric element and A represents the surface area of the element. The total potential energy π_e of an element is the total strain energy of the element minus the total work done and can be expressed as

$$\pi_e = U_e - \iint_A \{S\}^T \{f\} dA \quad (5.7)$$

where $\{S\}$ is a vector of nodal displacement and $\{f\}$ is the corresponding load vector containing inplane loads I , the transverse loads p and the applied moments M at all nodes on the element. U_e in the Eq. (5.7) is the strain energy of the axisymmetric element and is given by

$$U_e = \frac{1}{2} \int_{vol} \{\sigma\}^T \{\epsilon\} d(vol) \quad (5.8)$$

vol in Eq. (5.8) is the volume of the axisymmetric element. Substituting Eq. (5.5) into Eq. (5.8) strain energy for the element was written as

$$U_e = \frac{1}{2} \int_{vol} \{\epsilon\}^T [H] \{\epsilon\} d(vol) \quad (5.9)$$

where $[H]$ is the constitutive matrix given by Eq. (5.6). For a plate under combined bending and stretching the strain-displacement relation is given by Eq. (5.4). Substituting Eq. (5.4) into equation (5.9), strain energy U_e is:

$$U_e = \pi C_{eq} \int_{r_i}^{r_o} \{\epsilon_m\}^T [Q] \{\epsilon_m\} r dr \quad (5.10)$$

$$+ \pi D_{eq} \int_{r_i}^{r_o} \{\epsilon_b\}^T [Q] \{\epsilon_b\} r dr$$

C_{eq} and D_{eq} in Eq. (5.10) are called the membrane and the bending stiffness coefficients respectively and are given by

$$C_{eq} = \frac{E_{eq} h}{(1-\nu_{eq}^2)} \quad \text{and} \quad D_{eq} = \frac{E_{eq} h^3}{12 (1-\nu_{eq}^2)} \quad (5.11)$$

and

$$[Q] = \begin{bmatrix} 1 & \nu_{eq} \\ \nu_{eq} & 1 \end{bmatrix} \quad (5.12)$$

Substituting Eq. (5.10) into Eq. (5.7), the total potential energy of the element is:

$$\begin{aligned} \pi_e = & [\pi C_{eq} \int_{r_i}^{r_o} \{\epsilon_m\}^T [Q] \{\epsilon_m\} r dr \\ & + \pi D_{eq} \int_{r_i}^{r_o} \{\epsilon_b\}^T [Q] \{\epsilon_b\} r dr \\ & - 2\pi \int_{r_i}^{r_o} \{S\}^T \{f\} r dr] \end{aligned} \quad (5.13)$$

By using the principle of minimum potential energy, the element stiffness matrix was obtained as follows:

5.5. Stiffness Matrix of an Axisymmetric Element

A cubic displacement in w and a linear displacement in u were assumed in the plate element as

$$w = a_0 + a_1r + a_2r^2 + a_3r^3 \quad (5.14)$$

$$u = b_0 + b_1r \quad (5.15)$$

These displacement functions ensure the continuity of displacements between adjacent elements. Thus these displacement functions satisfy the compatibility requirements, which state that at element interfaces the field variables u , w and any of its partial derivatives up to one order less than the highest order derivative appearing in the energy expressions π_p must be continuous.

In the plate problems, the bending strains are defined by second derivatives of the transverse displacements. Therefore a cubic function in w will give a constant strain in an element. Similarly the membrane strains are defined by first derivatives of the radial displacements and thus a linear function in u will give a constant strain in an element. Therefore a cubic displacement function in w and a linear displacement function in u meets the constant strain condition in the element and thus satisfies the convergence criteria in the finite element. Equations (5.14) and (5.15) contains six unknowns a_0 , a_1 , a_2 , a_3 , b_0 , and b_1 and the axisymmetric plate element has two nodes, therefore each

node was assumed to have three degrees of freedom, the radial displacement u , the transverse displacement w , and the rotation $\frac{dw}{dr}$. These 3 degrees of freedom satisfy the compatibility requirements discussed earlier, which requires that the u , w , and $\frac{dw}{dr}$ should be continuous at element interfaces.

For any axisymmetric element with radius r_i and r_o , nodal displacements can be expressed in terms of generalized displacements as:

$$\begin{Bmatrix} u_i \\ w_i \\ \left(\frac{dw}{dr}\right)_i \\ u_o \\ w_o \\ \left(\frac{dw}{dr}\right)_o \end{Bmatrix} = \begin{bmatrix} 0 & 0 & 0 & 0 & 1 & r_i \\ 1 & r_i & r_i^2 & r_i^3 & 0 & 0 \\ 0 & 1 & 2r_i & 3r_i^2 & 0 & 0 \\ 0 & 0 & 0 & 0 & 1 & r_o \\ 1 & r_o & r_o & r_o & 0 & 0 \\ 0 & 1 & 2r_o & 3r_o^2 & 0 & 0 \end{bmatrix} \begin{Bmatrix} a_0 \\ a_1 \\ a_2 \\ a_3 \\ b_0 \\ b_1 \end{Bmatrix} \quad (5.16)$$

where subscripts i and o represent inner and outer nodes. Equation (5.16) was expressed in the concise form as follows:

$$\{\delta\}_e = [A] \{\alpha\} \quad (5.17)$$

where $\{\delta\}_e$ = the nodal displacement vector. From the foregoing, the solution for the unknown constant is

$$\{\alpha\} = [A]^{-1} \{\delta\}_e \quad (5.18)$$

Now consider the total potential energy equation (Eq. (5.13)). Applying the principle of the minimum potential energy, the variation in the

total potential energy should be equal to zero. Therefore the variation in the potential energy from Eq. (5.13) is

$$\begin{aligned}\Delta \pi_e &= [2\pi D_{eq} \int_{r_i}^{r_o} \{\Delta \varepsilon_b\}^T [Q] \{\varepsilon_b\} r dr \\ &\quad + 2\pi C_{eq} \int_{r_i}^{r_o} \{\Delta \varepsilon_m\}^T [Q] \{\varepsilon_m\} r dr] \\ &\quad - 2\pi \int_{r_i}^{r_o} \{\Delta s\}^T \{f\} r dr = 0\end{aligned}\quad (5.19)$$

The bending strains $\{\varepsilon_b\}$ in Eq. (5.19) are (Eq. (5.1))

$$\{\varepsilon_b\} = \left\{ \begin{array}{l} -\frac{d^2 w}{dr^2} \\ -\frac{1}{r} \frac{dw}{dr} \end{array} \right\}$$

Using the shape functions (Eq. (5.14)), $(\frac{dw}{dr})$ and $(\frac{d^2 w}{dr^2})$ can be written as

$$\frac{dw}{dr} = a_1 + 2a_2r + 3a_3r^2 \quad (5.20)$$

and

$$\frac{d^2 w}{dr^2} = 2a_2 + 6a_3r \quad (5.21)$$

Using Eqs. (5.20) and (5.21), $\{\varepsilon_b\}$ can be expressed in matrix form as

$$\{\epsilon_b\} = \begin{bmatrix} 0 & 0 & -2 & -6r & 0 & 0 \\ 0 & -\frac{1}{r} & -2 & -3r & 0 & 0 \end{bmatrix} \begin{Bmatrix} a_0 \\ a_1 \\ a_2 \\ a_3 \\ b_0 \\ b_1 \end{Bmatrix} \quad (5.22)$$

or concisely as,

$$\{\epsilon_b\} = [R] \{\alpha\} \quad (5.23)$$

$$= [R] [A]^{-1} \{\delta\}_e \quad (5.24)$$

Using Eq. (5.24), $\{\Delta\epsilon_b\}$ can be written as

$$\{\Delta\epsilon_b\} = [R] [A]^{-1} \{\Delta\delta\}_e \quad (5.25)$$

5.5.1 Nonlinear Terms: - Linearization Procedure

Consider the membrane strains $\{\epsilon_m\}$ in the equation (5.19). They are:

$$\{\epsilon_m\} = \begin{Bmatrix} \frac{dr}{dr} + \frac{1}{2} \left(\frac{dw}{dr} \right)^2 \\ \frac{u}{2} \end{Bmatrix}$$

Since the vector $\{\epsilon_m\}$ contains a nonlinear term $\frac{1}{2} \left(\frac{dw}{dr} \right)^2$ a linearization technique [36] needs to be used. The linearization procedure used is as follows:

Consider a nonlinear term $\frac{1}{2} \left(\frac{dw}{dr} \right)^2$ in the membrane strains $\{\epsilon_m\}$.

$$\text{Let } \frac{1}{2} \frac{dw}{dr} = B \quad (5.26)$$

where B is called as a linearization constant. Using this definition the membrane strains can be written as,

$$\{\varepsilon_m\} = \begin{Bmatrix} \frac{dr}{dr} + B \frac{dw}{dr} \\ \frac{u}{r} \end{Bmatrix} \quad (5.27)$$

Using Eq. (5.15), $\frac{du}{dr}$ and $\frac{u}{r}$ can be written as

$$\frac{du}{dr} = b_1 \quad (5.28)$$

and

$$\frac{u}{r} = \frac{b_0}{r} + b_1 \quad (5.29)$$

Using Eqs. (5.20), (5.28) and (5.29), $\{\varepsilon_m\}$ can be expressed in matrix form as

$$\{\varepsilon_m\} = \begin{bmatrix} 0 & B & 2 Br & 3 Br^2 & 0 & 1 \\ 0 & 0 & 0 & 0 & \frac{1}{r} & 1 \end{bmatrix} \begin{Bmatrix} a_0 \\ a_1 \\ a_2 \\ a_3 \\ b_0 \\ b_1 \end{Bmatrix} \quad (5.30)$$

or concisely as,

$$\{\varepsilon_m\} = [T] \{\alpha\} \quad (5.31)$$

$$= [T] [A]^{-1} \{\delta\}_e \quad (5.32)$$

The next step is to evaluate the variation of the membrane strains, $\{\Delta\epsilon_m\}$. This is achieved as follows:

The membrane strains $\{\epsilon_m\}$ can be represented as the sum of the two vectors, one containing only the linear terms, whereas the other containing the nonlinear terms. Therefore,

$$\{\epsilon_m\} = \{\epsilon_L\} + \{\epsilon_{NL}\} \quad (5.33)$$

where

$$\{\epsilon_L\} = \begin{Bmatrix} \frac{du}{dr} \\ \frac{u}{r} \end{Bmatrix} \quad (5.34)$$

$$\{\epsilon_{NL}\} = \begin{Bmatrix} \frac{1}{2} \left(\frac{dw}{dr} \right)^2 \\ 0 \end{Bmatrix} \quad (5.35)$$

The variation of $\{\epsilon_m\}$, then is

$$\{\Delta\epsilon_m\} = \{\Delta\epsilon_L\} + \{\Delta\epsilon_{NL}\} \quad (5.36)$$

or

$$\{\Delta\epsilon_m\} = \begin{Bmatrix} \Delta \left(\frac{du}{dr} \right) \\ \Delta \left(\frac{u}{r} \right) \end{Bmatrix} + \begin{Bmatrix} \Delta \left\{ \frac{1}{2} \left(\frac{dw}{dr} \right)^2 \right\} \\ \Delta (0) \end{Bmatrix} \quad (5.37)$$

or

$$\{\Delta\epsilon_m\} = \begin{Bmatrix} \Delta \left(\frac{du}{dr} \right) \\ \Delta \left(\frac{u}{r} \right) \end{Bmatrix} + \begin{Bmatrix} \frac{1}{2} \cdot 2 \cdot \frac{dw}{dr} \Delta \left(\frac{dw}{dr} \right) \\ 0 \end{Bmatrix} \quad (5.38)$$

The linearization constant B is then used in Eq. (5.38) and $\{\Delta\epsilon_m\}$ is rewritten as,

$$\{\Delta\epsilon_m\} = \begin{Bmatrix} \Delta \left(\frac{du}{dr} \right) \\ \Delta \left(\frac{u}{r} \right) \end{Bmatrix} + \begin{Bmatrix} 2 B \Delta \left(\frac{dw}{dr} \right) \\ \Delta (o) \end{Bmatrix} \quad (5.39)$$

Using the shape functions for u and w the variation of membrane strains can be expressed in the matrix form as,

$$\begin{aligned} \{\Delta\epsilon_m\} &= \Delta \begin{bmatrix} 0 & 0 & 0 & 0 & 0 & 1/r & 1 \end{bmatrix} \begin{Bmatrix} a_0 \\ a_1 \\ a_2 \\ a_3 \\ b_0 \\ b_1 \end{Bmatrix} \\ &\quad + \Delta \begin{bmatrix} 0 & 2 B & 4 Br & 6 Br^2 & 0 & 0 \\ 0 & 0 & 0 & 0 & 0 & 0 \end{bmatrix} \begin{Bmatrix} a_0 \\ a_1 \\ a_2 \\ a_3 \\ b_0 \\ b_1 \end{Bmatrix} \quad (5.40) \end{aligned}$$

or in concise form as,

$$\{\Delta\epsilon_m\} = \Delta [[Y_1] [A]^{-1} \{\delta\}_e + [Y_2] [A]^{-1} \{\delta\}_e] \quad (5.41)$$

$$= [Y_1 + Y_2] [A]^{-1} \{\delta\}_e \quad (5.42)$$

Lastly consider a generalized displacement vector $\{S\}$

$$\{S\} = \begin{Bmatrix} u \\ w \\ \frac{dw}{dr} \end{Bmatrix} \quad (5.43)$$

Using Eqs. (5.14), (5.15) and (5.20), a generalized displacement vector can be expressed in the matrix form as

$$\{S\} = \begin{bmatrix} 0 & 0 & 0 & 0 & 1 & r \\ 1 & r & r^2 & r^3 & 0 & 0 \\ 0 & 1 & 2r & 3r^2 & 0 & 0 \end{bmatrix} \begin{Bmatrix} a_0 \\ a_1 \\ a_2 \\ a_3 \\ b_0 \\ b_1 \end{Bmatrix} \quad (5.44)$$

or in concise form

$$\{S\} = [N] \{\alpha\} \quad (5.45)$$

By using Eq. (5.18) for $\{\alpha\}$, in Eq. (5.45), Eq. (5.45) was written as

$$\{S\} = [N] [A]^{-1} \{\delta\}_e \quad (5.46)$$

and

$$\{\Delta S\} = [N] [A]^{-1} \{\Delta \delta\}_e \quad (5.47)$$

In summary the matrices obtained so far are,

$$\{\epsilon_b\} = [R] [A]^{-1} \{\delta\}_e \quad \{\Delta \epsilon_b\} = [R] [A]^{-1} \{\Delta \delta\}_e$$

$$\{\epsilon_m\} = [T] [A]^{-1} \{\delta\}_e \quad \{\Delta \epsilon_m\} = [Y_1 + Y_2] [A]^{-1} \{\Delta \delta\}_e$$

$$\{S\} = [N] [A]^{-1} \{\delta\}_e \quad \{\Delta S\} = [N] [A]^{-1} \{\Delta \delta\}_e$$

The variation in the potential energy of the element ($\Delta \pi_e$) of Eq.(5.19) is then,

$$\begin{aligned} \Delta \pi_e &= 2\pi D_{eq} \int_{r_i}^{r_o} \{\Delta \delta\}_e^T [[A]^{-1}]^T [R]^T [Q] [R] [A]^{-1} \{\delta\}_e r dr \\ &\quad + 2\pi C_{eq} \int_{r_1}^{r_o} \{\Delta \delta\}_e^T [[A]^{-1}]^T [Y_1 + Y_2]^T [Q] [T] [A]^{-1} \{\delta\}_e r dr \\ &\quad - 2\pi \int_{r_i}^{r_o} \{\Delta \delta\}_e^T [[A]^{-1}]^T [N]^T \{f\}_e r dr = 0 \end{aligned} \quad (5.48)$$

Since Eq. (5.48) should be valid for arbitrary values of $\{\Delta \delta\}_e$, Eq. (5.48) reduces to

$$\{[k_L]_e + [k_{NL}]_e\} \{\delta\}_e = \{F\}_e \quad (5.49)$$

where $[k_L]_e$ and $[k_{NL}]_e$ are called the bending and the membrane stiffness matrix for the element and $\{F\}_e$ is the corresponding load vector and are given by

$$[k_L]_e = 2\pi D_{eq} \int_{r_i}^{r_o} [[A]^{-1}]^T [R]^T [Q] [R] [A]^{-1} r dr \quad (5.50)$$

$$[k_{NL}]_e = 2\pi C_{eq} \int_{r_i}^{r_o} [[A]^{-1}]^T [Y_1 + Y_2]^T [Q] [T] [A]^{-1} r dr \quad (5.51)$$

$$\{F\}_e = 2\pi \int_{r_i}^{r_o} [A]^{-1}]^T [N]^T \{f\} r dr \quad (5.52)$$

Assembling the element stiffnesses and nodal loads, global stiffness matrix and total load vector can be obtained and Eq. (5.49) can be written as:

$$[K] \{\delta\} = \{F\} \quad (5.53)$$

where $[K]$ is a global stiffness matrix and is given by

$$[K] = \sum_1^n \{[k_L]_e + [k_{NL}]_e\} \quad (5.54)$$

and

$$\{F\} = \sum_1^n \{F\}_e \quad (5.55)$$

5.5.2 Boundary Conditions

For the clamped circular quasi-isotropic plate with axisymmetric loading, boundary conditions are

1. The radial displacement u and the rotation $(\frac{dw}{dr})$ equal zero at the center ($r = 0$).
2. The radial displacement u , the transverse displacement w , and the rotation $(\frac{dw}{dr})$ equal zero at the clamped edge ($r = a$).

5.6 Solution Procedure

To solve the governing Eq. (5.53) for the nodal displacements $\{\delta\}$, the solution domain was discretized into n axisymmetric elements and $(n+1)$ nodes. Each node had three degrees of freedom, the radial displacement u , the transverse displacement w , and the rotation $(\frac{dw}{dr})$. In Eq. (5.53), $[K]$ is a global stiffness matrix and is given by the Eq. (5.54) as:

$$[K] = \sum_1^n \{[k_L]_e + [k_{NL}]_e\}$$

In order to evaluate the global stiffness matrix $[K]$, it is required to obtain the bending stiffness matrix $[k_L]_e$ and the membrane stiffness $[k_{NL}]_e$ for each element. However, the membrane stiffness matrix $[k_{NL}]_e$ (Eq. (5.51)) contains the linearizing function "B" and as the function "B" was not known a priori, an iterative scheme was adopted in the present solution. The details of the iterative scheme are given below and presented in the flow chart of Fig. 5.2.

The linear bending stiffness $[k_L]_e$ and the load vector $\{F\}_e$ were computed by using Eqs. (5.50) and (5.52) (step 3, Fig. 5.2). Since the linearizing function B, was not known a priori, it was assumed zero and hence the membrane stiffness $[k_{NL}]_e$ was a null matrix (step 4, Fig. 5.2). Using Eqs. (5.54) and (5.55), the global stiffness matrix $[K]$ and the load vector $\{F\}$ were computed (step 6, Fig. 5.2). Equation (5.53) was then solved to obtain the linear displacement solution $\{\delta\}$ (step 7, Fig. 5.2). By using the linear displacements and the rotations at each node, the linearizing function "B" and the membrane stiffness

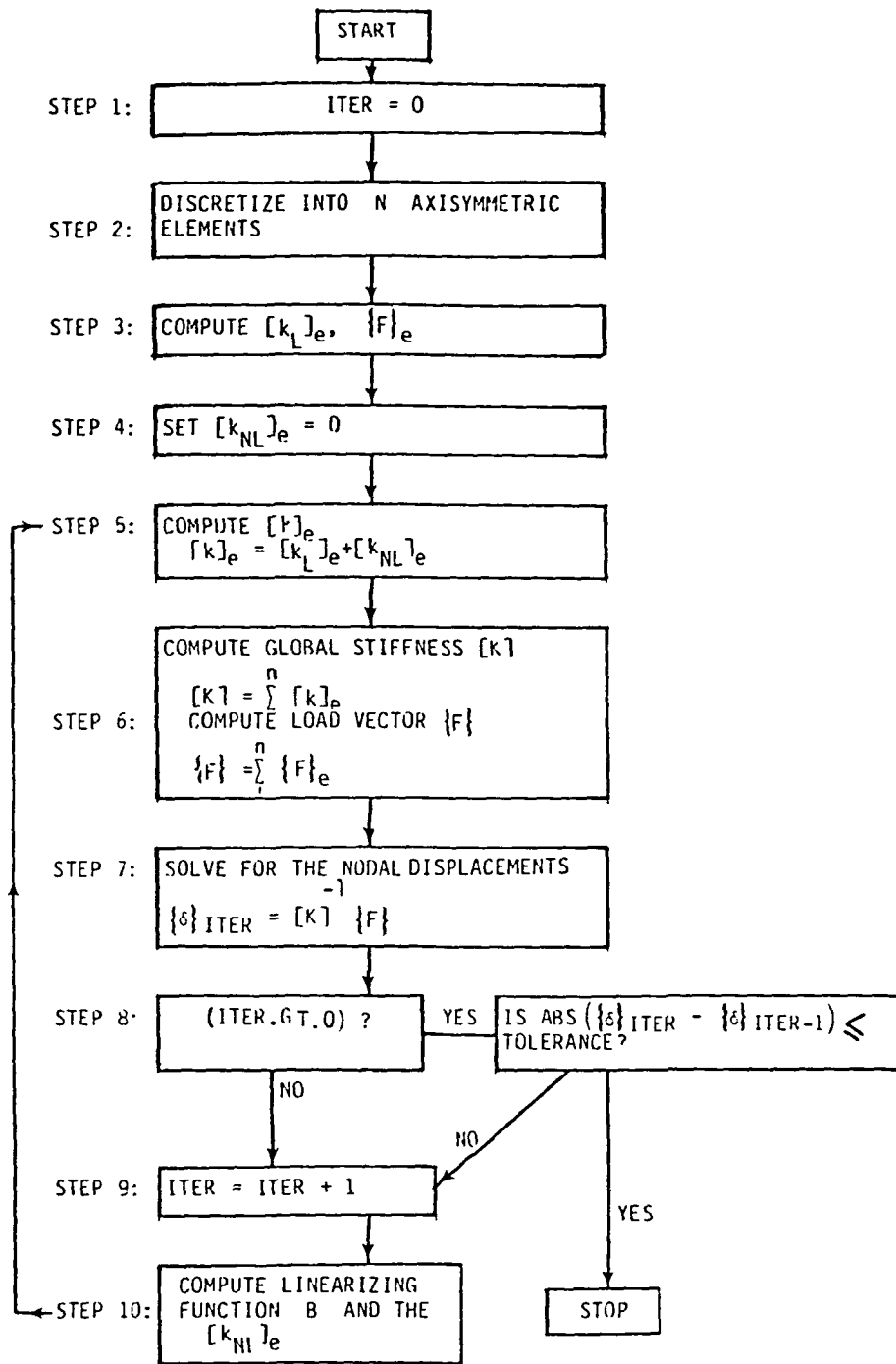


Fig. 5.2 Flow Chart for the Finite Element Model

$[k_{NL}]_e$ were computed (step 10, Fig. 5.2). The total stiffness matrix of the element $[k]_e$ is then the sum of the linear bending stiffness $[k_L]_e$ and current membrane stiffness $[k_{NL}]_e$. The global stiffness matrix $[K]$ was then formed and the new displacements were computed. Using the new displacements a new $[k_{NL}]_e$ matrix is computed. This iterative procedure was continued until there was no significant difference in displacements between the successive iterations.

5.7 Convergence Study

To study the convergence of the present method, the circular plate was discretized into n axisymmetric elements and $(n+1)$ nodes. A systematic convergence study was made by increasing the number of elements in the idealizations. The number of elements used in this convergence study were 2, 4, 8, 16, 32, 40, and 48. For the centrally loaded clamped circular plate with center deflection to plate thickness ratio of 2.0, a 48 element idealization was found to obtain a converged nonlinear solution. Figure 5.3 presents the relative errors in the maximum deflections normalized with respect to the converged maximum center deflections. The solution shows a rapid convergence and about 32 regions were found to be necessary to yield a solution which is with 0.01 percent of the converged solution.

By using the 48 element idealization, the clamped quasi-isotropic circular plate was analyzed to obtain the large deformation solutions for various center deflection-to-plate thickness ratios. As the center deflection-to-plate thickness ratio increases, the number of iterations required to obtain the large deformation solution increased. Table 5.1 presents the number of iterations required to obtain the large deforma-

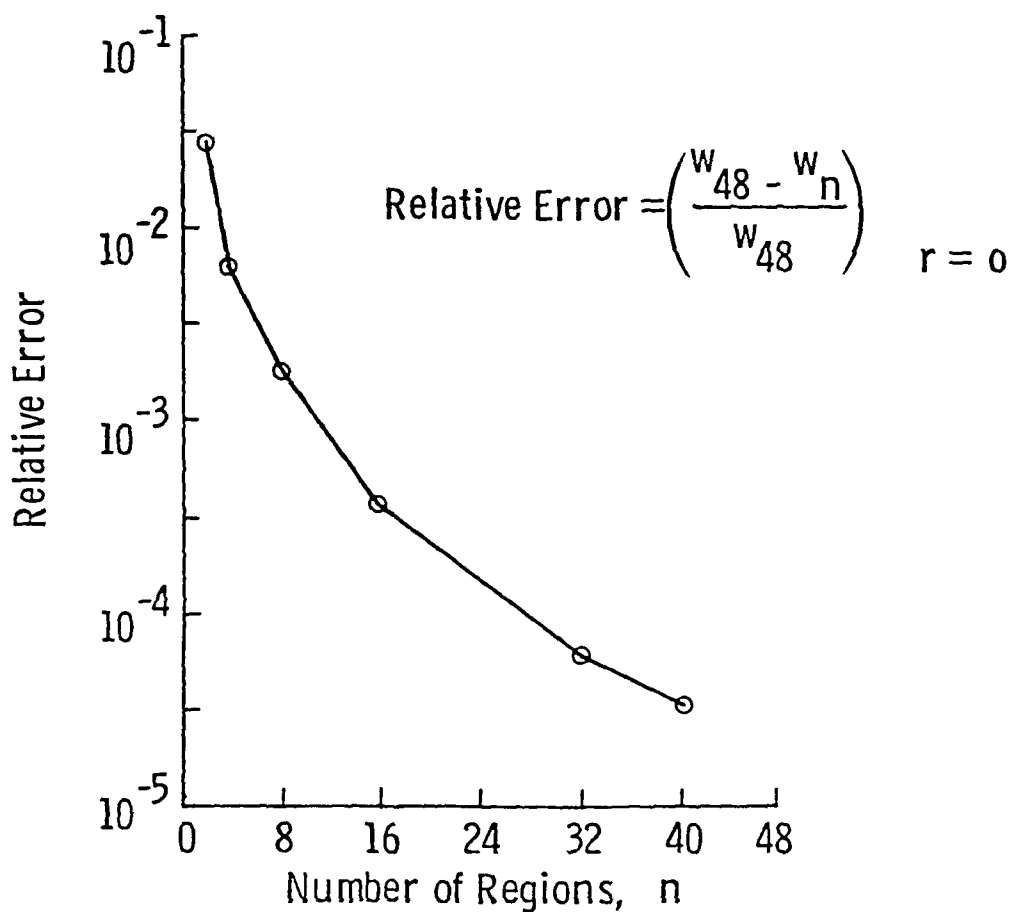


Fig. 5.3 Convergence Study for the Plate Carrying a Concentrated Load at the Center

tion solution of the clamped circular quasi-isotropic laminates under point loads for central deflection-to-plate thickness ratios ranging from 0.5 to 2.0.

5.8 Results and Discussion

In this section, the deflected shapes obtained with the finite element model for the central deflection to plate thickness ratios ranging from 0.5 to 2.0 are compared with the deflected shapes obtained by using the plate-membrane coupling model. Next the load-displacement curve obtained by using the finite element model is compared with the load-displacement curve obtained earlier by using the plate-membrane coupling model.

The transverse displacements w obtained by using the finite element model and the plate-membrane coupling model (Chap. 4) for various central deflection to plate thickness ratios ranging from 0.5 to 2.0 are presented in Table 5.2. The results obtained by the finite element model are in excellent agreement with those obtained earlier by using the plate-membrane coupling model.

Figure 5.4 presents a comparison between the load-displacement curves obtained by using the finite element model and the plate-membrane coupling model. Figure 5.4 indicates that the results obtained by using the finite element model compare well with those obtained by using the plate-membrane coupling model. Figure 5.4 also shows the effect of nonlinearity on the plate deflection. For any given load the nonlinear displacement is much smaller than the linear displacement.

As pointed out in the introduction, in the current finite element formulation, the membrane effects due to the mid-plane stretching are

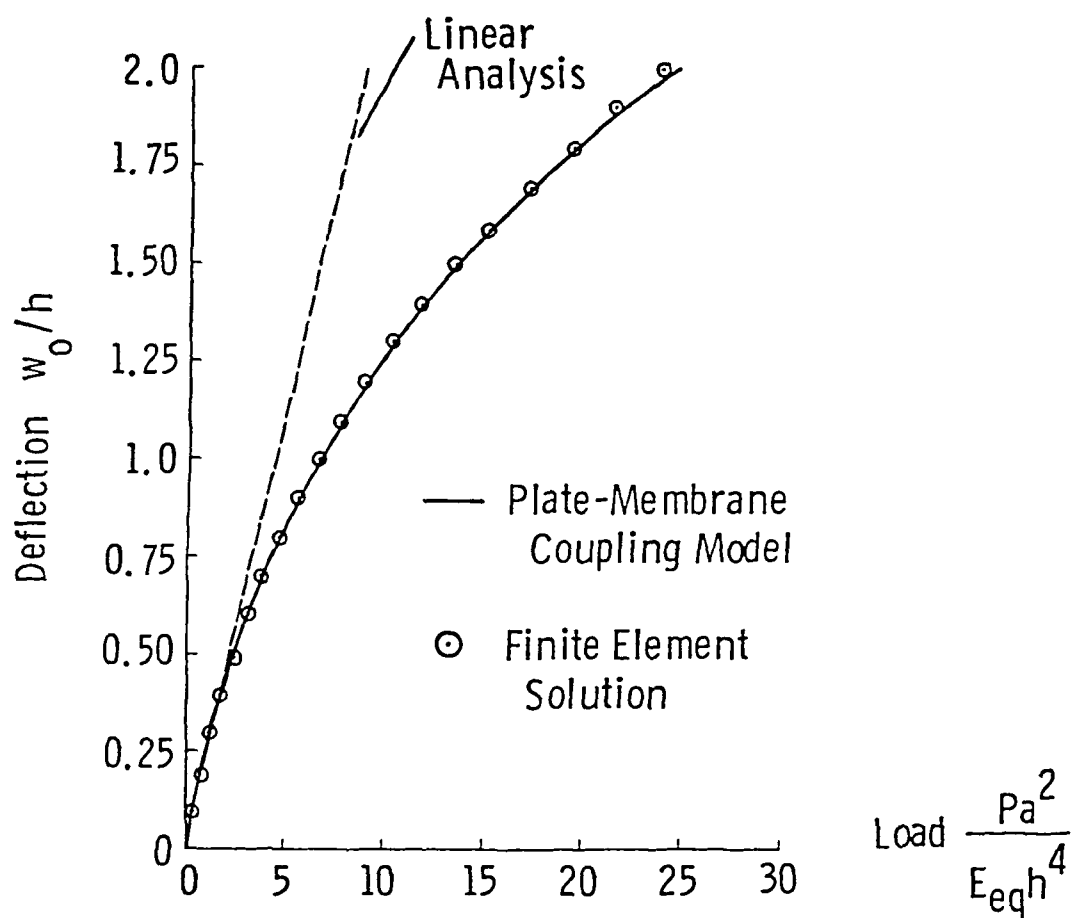


Fig. 5.4 Load-Displacement Curve

considered. So it is interesting to compare the radial displacements obtained by using the finite element model, with those obtained by using the classical solution (Appendix B). Figures 5.5 and 5.6 show a comparison of the radial displacements for the central deflection to plate thickness ratios of 0.5 to 2.0. The functional form of the radial displacement curve obtained by using the classical solution is identical for the central deflection to plate thickness ratios of 0.5 and 2.0. On the other hand, the functional form of the radial displacement curve obtained by using the finite element model and the plate-membrane coupling model is different for the central deflection to plate thickness ratios of 0.5 and 2.0.

Figures 5.5 and 5.6 also show that the magnitudes of the radial displacements are three orders less as compared to the magnitudes of the transverse displacements. Although the radial displacements are much smaller in comparison with the transverse displacements, their contribution to the membrane radial strains, and the tangential strains is significant. These membrane strains are particularly important for strain energy calculations in the back face spalling model. Thus for accurate predictions of stresses and strains in the plate, the radial displacements should be incorporated into the finite element formulation.

Figure 5.6 indicates that, for the central deflection to plate thickness ratio of 2.0, radial displacements obtained by using the classical solution are in good agreement with those obtained by using the finite element solution and the plate-membrane coupling model solution. On the other hand, Fig. 5.5 shows that, for the center deflection to plate thickness ratio of 0.5, radial displacements

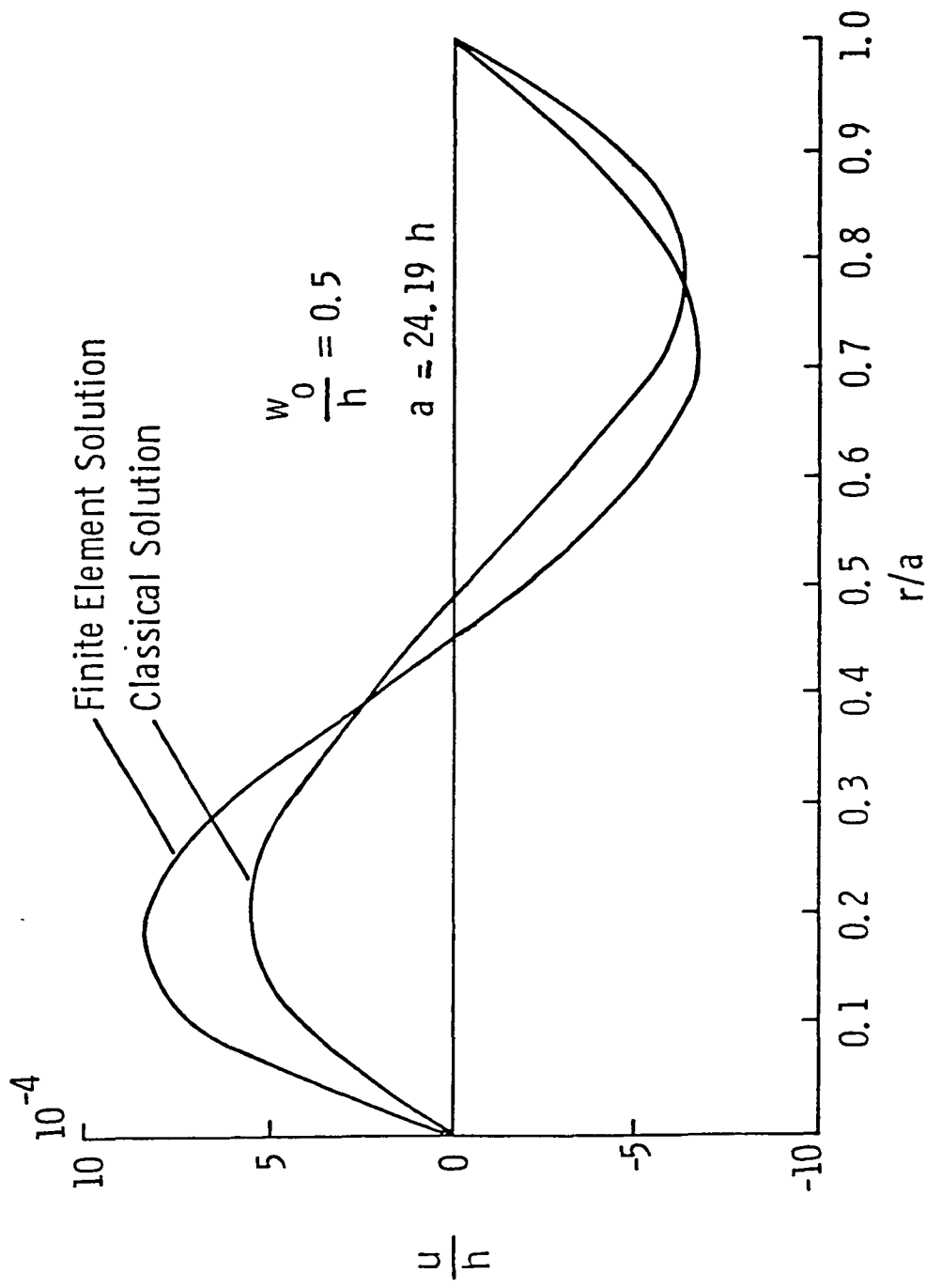


Fig. 5.5 Comparison of Radial Displacements for the Center Deflection to the Plate Thickness Ratio Equal to 0.5

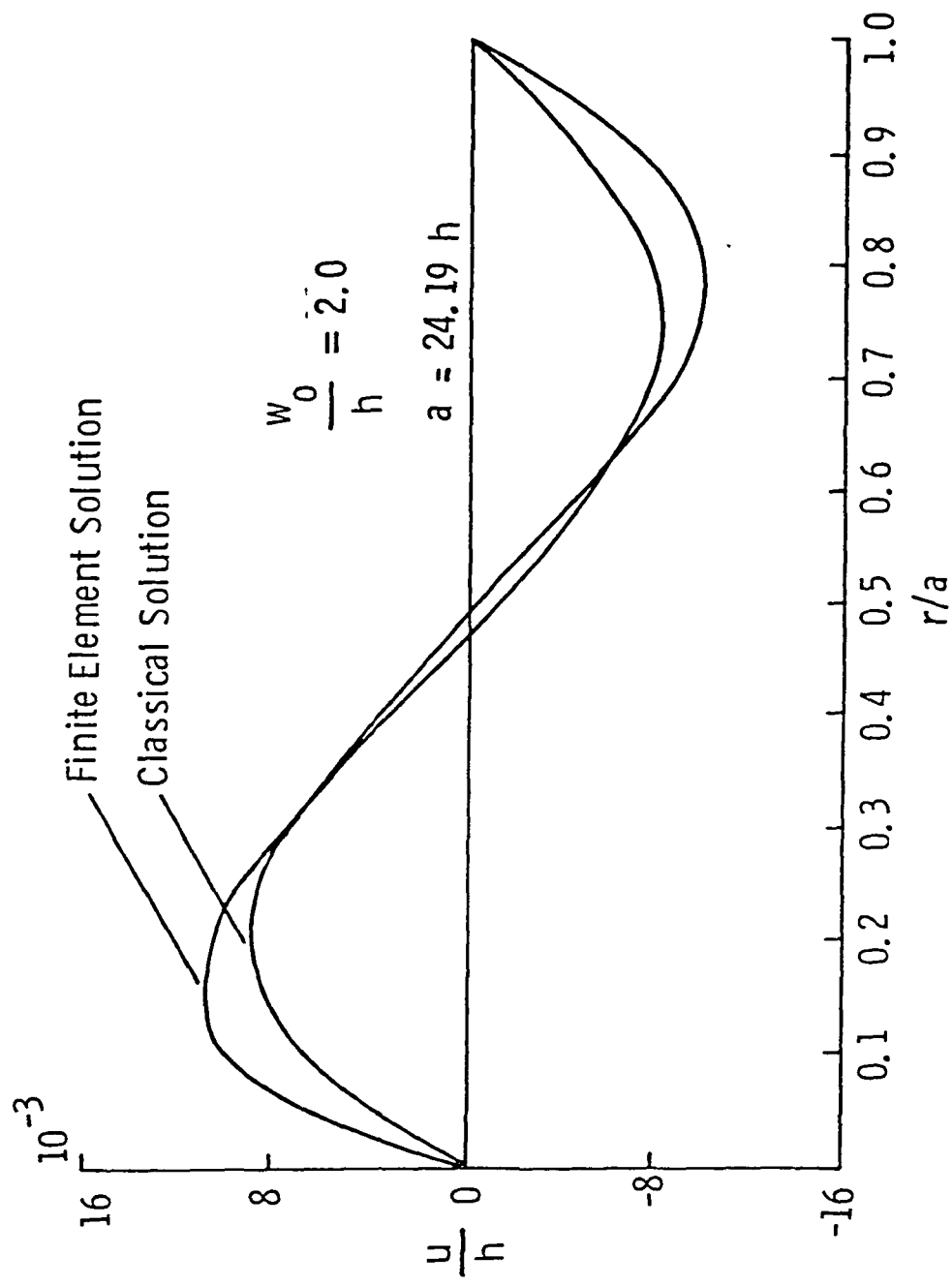


Fig. 5.6 Comparison of Radial Displacements for the Center Deflection to the Plate Thickness Ratio Equal to 2.0

obtained by using the classical solution differ considerably from the corresponding finite element solution and the plate-membrane coupling model solution. Therefore the functional form of the radial displacements assumed in the classical solution would predict correct radial displacements only for higher values of the center-deflection to plate thickness ratios, while for lower values of the center deflection to plate thickness ratios, the functional form of the radial displacements assumed in the classical solution would predict incorrect values of the radial displacements.

5.9 Concluding Remarks

In this chapter, circular quasi-isotropic composite plates were analyzed to study the large deformation behavior under point loads. A finite element model was formulated to study the large deformation behavior of these plates. A finite element model, in contrast to those in the literature, considers both radial and transverse displacements in its formulation. This model uses a linearization technique with an iterative procedure to obtain the large deformation shapes for thin composite laminates under the point loads.

The deformation shapes obtained by using the finite element model agreed very well with the deformation shapes obtained by using the plate-membrane coupling model. The load-deflection curve was obtained using the finite element model and compared with the load-deflection curve obtained by using the plate-membrane coupling model. Excellent agreement was observed between the two results. The classical solution [27], based on the energy method, assumes that the functional form of the radial displacements curve is identical for the various values of

ORIGINAL PAGE IS
OF POOR QUALITY

the central displacements to plate thickness ratios, whereas the finite element model indicates that the functional form of the radial displacements curve is different for the various values of the central displacements to plate thickness ratios. The radial displacements are found to be about three orders of magnitude less, as compared to the transverse displacements. The radial displacements obtained by using the finite element solution compares well with the classical solution for the central deflection to plate thickness ratio of 2.0, but they are significantly different from the classical solution for the center deflection to plate thickness ratio of 0.5.

Table 5.1 - Number of Iterations Required to Obtain Large Deformation Solution of a Clamped Circular Plate Under Central Point Load

Plate center deflection to thickness ratio ($\frac{w_0}{h}$)	Number of iterations
0.5	4
1.0	9
1.5	17
2.0	29

Table 5.2(a) - Comparison of the Transverse Displacements w
 Obtained by Using the Finite Element Model and
 the Plate-Membrane Coupling Model for $(\frac{w_0}{h})$ Ratios
 of 0.5 and 1.0.

r/a		Finite Element Model	Plate-Membrane Coupling Model
$(\frac{w_0}{h}) = 0.5$	0.0	0.50000	0.50000
	0.1	0.46810	0.46764
	0.2	0.40963	0.40842
	0.3	0.34011	0.33791
	0.4	0.26712	0.26484
	0.5	0.20418	0.20311
	0.6	0.13558	0.13506
	0.7	0.07916	0.07762
	0.8	0.03763	0.03828
	0.9	0.00983	0.01001
$(\frac{w_0}{h}) = 1.0$	1.0	0.00000	0.00000
	0.0	1.00000	1.00000
	0.1	0.93167	0.93050
	0.2	0.81098	0.80831
	0.3	0.67184	0.66745
	0.4	0.53024	0.52491
	0.5	0.39756	0.39392
	0.6	0.27246	0.27028
	0.7	0.16224	0.16570
	0.8	0.07546	0.07719
	0.9	0.02024	0.02074
	1.0	0.00000	0.00000

Table 5.2(b) - Comparison of the Transverse Displacements w
 Obtained by Using the Finite Element Model and
 the Plate-Membrane Coupling Model for $(\frac{w_0}{h})$ Ratios
 of 1.5 and 2.0.

r/a		Finite Element Model	Plate-Membrane Coupling Model
$(\frac{w_0}{h}) = 1.5$	0.0	1.50000	1.50000
	0.1	1.38780	1.38595
	0.2	1.19976	1.19548
	0.3	0.99214	0.98512
	0.4	0.79318	0.78421
	0.5	0.59440	0.58841
	0.6	0.40648	0.40245
	0.7	0.24651	0.25309
	0.8	0.11811	0.12140
	0.9	0.03186	0.03286
$(\frac{w_0}{h}) = 2.0$	1.0	0.00000	0.00000
	0.0	2.00000	2.00000
	0.1	1.83683	1.83399
	0.2	1.57758	1.57111
	0.3	1.30415	1.29297
	0.4	1.03569	1.02026
	0.5	0.78009	0.77129
	0.6	0.54370	0.53813
	0.7	0.33418	0.34512
	0.8	0.16317	0.16870
	0.9	0.04395	0.04561
	1.0	0.00000	0.00000

Chapter 6

PLATE MECHANICS EXPERIMENTS

6.1 Introduction

In Chaps. 4 and 5, the plate-membrane coupling model and the finite element model were developed to study the large deformation behavior of circular quasi-isotropic plates. Both of these models assume that the quasi-isotropic T300/5208 graphite/epoxy laminates with stacking sequence [45/0/-45/90]_S, are flexurally isotropic. In this chapter this assumption of flexural isotropy is experimentally verified.

The large deformation shapes and the load-displacement curves for the circular quasi-isotropic plates under central point loads were obtained by conducting series of tests on the circular quasi-isotropic laminates. First, the experimentally obtained deflected shapes are compared with the analytical deflected shapes obtained by using the plate-membrane coupling model and the finite element model. Then, the experimental load-displacement curve is compared with those of the plate-membrane coupling model and the finite element model.

6.2 Test Set-up

To study the large deformation behavior of circular plates under central point loads, a torque bolt arrangement and a servo-hydraulic testing machine were used. The torque bolt arrangement was used to obtain the large deformation shapes of the circular plates under central

point loads and the servo-hydraulic testing machine was used to obtain the load-displacement behavior of the circular plates under central point loads. For both tests, quasi-isotropic graphite/epoxy laminates, with the stacking sequence of $[45/0/-45/90]_S$ and the material properties given in Table 2.1 were used. Circular laminates with 76.2 mm (3 inches) or 101.6 mm (4 inches) diameters were bolted between two steel annular plates as shown in Fig. 6.1. These steel plates provided clamped boundary conditions for the specimens. A torque bolt arrangement was used to push a 25.4 mm diameter steel ball against the laminate, to provide the desired static loading (Fig. 6.2). Although the ball diameter was 25.4 mm, the contact radius between the ball and the plate was very small (of the order of 1 mm) and thus pushing the steel ball simulated the desired static point load conditions.

A traversing horizontal direct current differential transducer (DCDT) and a vertical DCDT were used to measure the deflected shapes of the clamped circular quasi-isotropic laminates as shown in Fig. 6.1.

To obtain a load-deflection curve, the static loading tests were conducted in a servo-hydraulic testing machine. The test specimens were clamped to a platform, shown in Fig. 6.3, which was mounted on the hydraulic ram, and load was applied to the center of the specimen by means of a punch, tipped with a 25.4 mm diameter steel ball. A DCDT displacement gauge was attached to the indenter to measure plate deflection as the load was applied. The electric signals from the load cell and the displacement gauge were given as an input to the x-y plotter to allow direct load-displacement plotting.

ORIGINAL PAGE IS
OF POOR QUALITY



Fig. 6.1 Experimental Set Up

ORIGINAL PAGE IS
OF POOR QUALITY

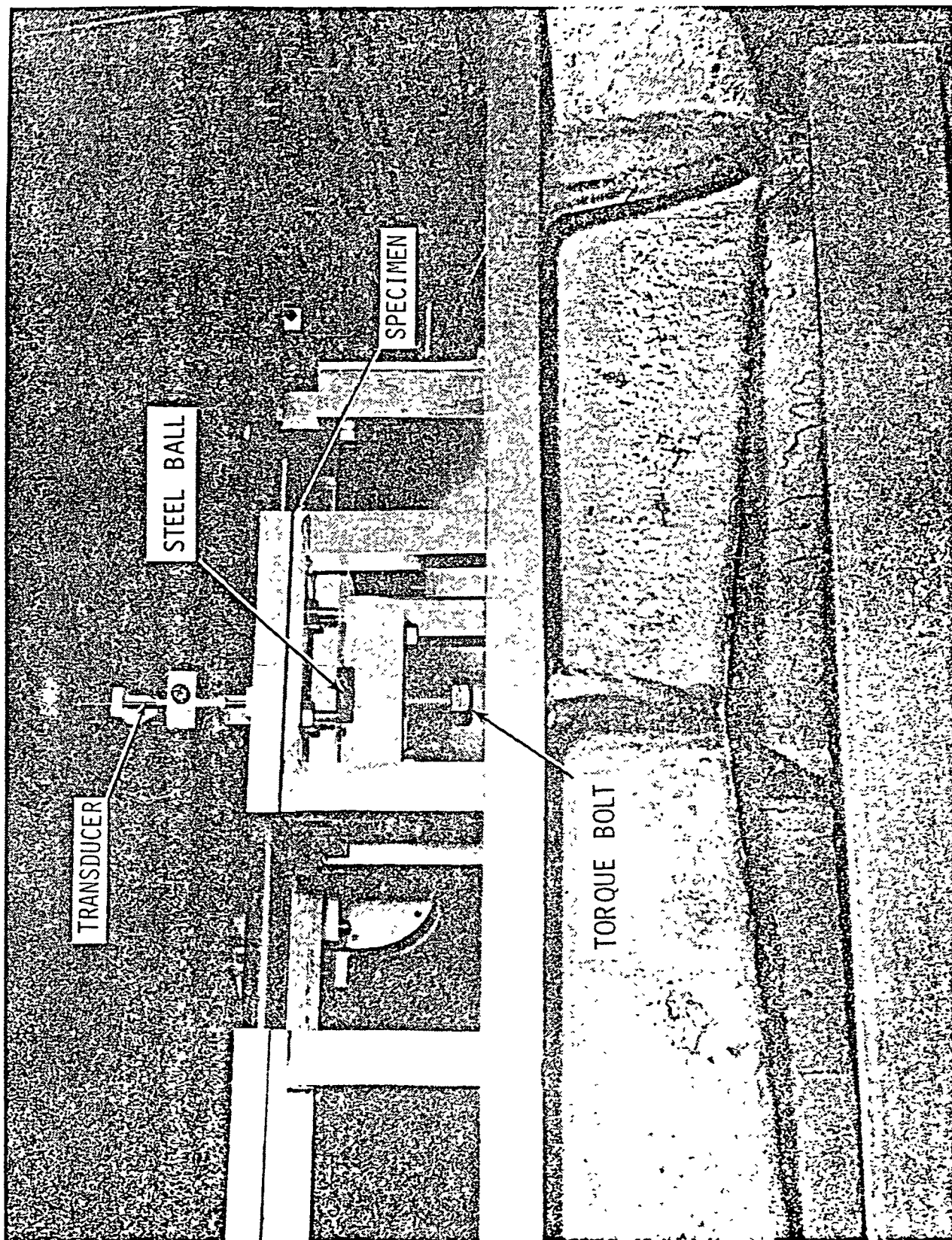


Fig. 6.2 Loading on the Specimen

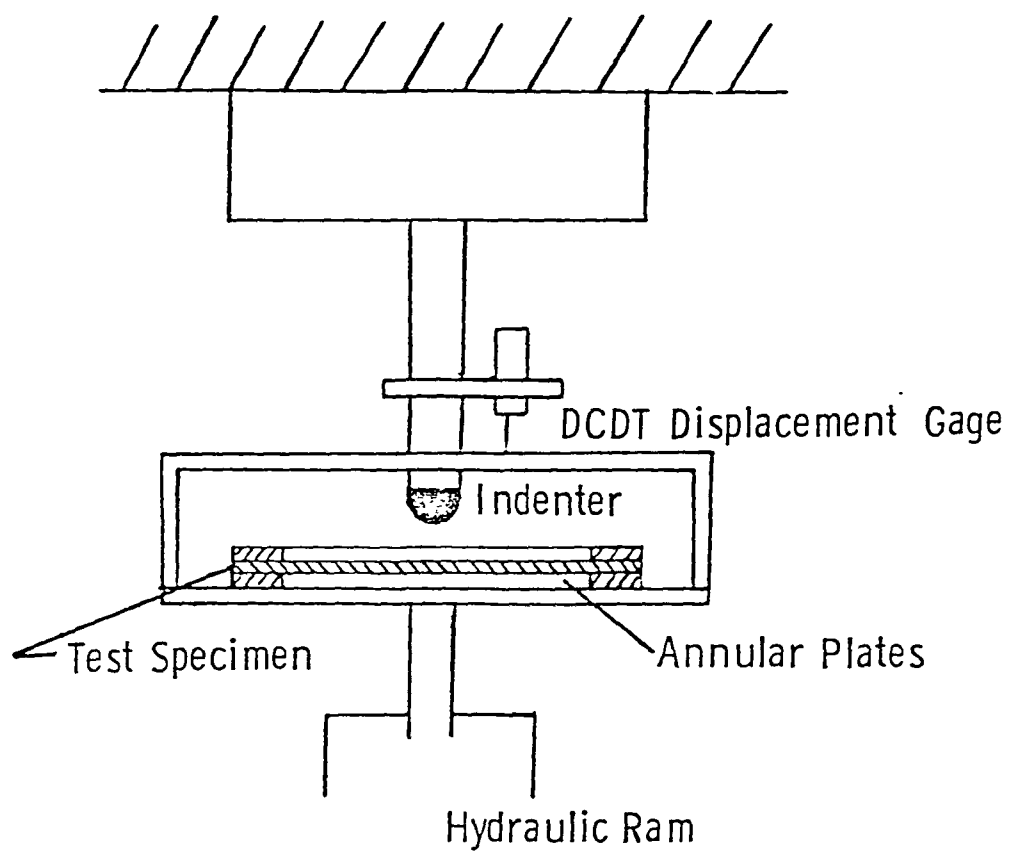


Fig. 6.3 Static Loading on the Quasi-Isotropic Circular Laminate

6.3 Test Data

Circular quasi-isotropic plates of two sizes with diameters 76.2 mm and 101.6 mm were tested. By using the torque bolt arrangement, the 76.2 mm diameter plate was loaded till the desired center deflection was obtained. This center displacement was measured by using the vertical DCDT. Once the desired center displacement was obtained, the first set of observations were made along the fiber direction ($\theta = 0^\circ$) of the eighth ply (farthermost ply from the point of load application). The second and third set of observations were made on a line perpendicular to the fiber direction of the eighth ply, ($\theta = 90^\circ$) and on a line 45° ($\theta = 45^\circ$) to the fiber direction of the eighth ply, respectively. These three sets of observations were recorded for central deflection-to-plate-thickness ratio ($\frac{w_0}{h}$) of 0.5, 1.0, 1.5, and 2.0. Similar observations were made for 101.4 mm diameter plate.

The load-displacement data were obtained by using the servo-hydraulic machine. The 76.2 mm diameter and the 101.4 mm diameter plates were loaded and the corresponding central deflections were recorded till the central deflection was about two times the plate thickness.

6.4 Results and Discussion

In this section, first the validity of flexural isotropy in circular quasi-isotropic laminate is discussed. Then the measured deflected shapes are compared with the plate-membrane coupling model and the finite element model.

To verify the flexural isotropy in the circular quasi-isotropic laminates, experimental measurements made along three diametral lines at

$\theta = 0^0$, $\theta = 45^0$ and $\theta = 90^0$, for various values of the central deflection-to-plate thickness ratios ranging from 0.5 to 2.0 were compared. Figure 6.4 presents the typical deflected shapes for $(\frac{w_0}{h})$ ratios of 0.5 and 1.5 along $\theta = 0^0$ and 90^0 radial lines. The deflected shapes for ratios of 1.0 and 2.0 showed similar trends and hence are not shown. The experimental observations showed that the deflected shapes along $\theta = 45^0$ were bounded by the shapes along $\theta = 0^0$ and $\theta = 90^0$. The maximum differences between the $\theta 0^0$ and 90^0 observations occurred near $(\frac{r}{a}) = 0.4$ and were about six percent of the maximum center deflections. Thus the experimental observations indicate that clamped circular quasi-isotropic laminates, subjected to axisymmetric loading, exhibit near flexural isotropy and show nearly axisymmetric bending behavior.

Figures 6.5 and 6.6 present the measured deflected shapes at $\theta = 0^0$ and the analytical deflected shapes obtained with the plate-membrane coupling model for $(\frac{w_0}{h})$ ratios ranging from 0.5 to 2.0. Since the deflected shapes obtained by using the finite element model are almost identical to those obtained by using the plate-membrane coupling model (Table 4.1), only the plate-membrane coupling model results are compared with the experimental data. In Figs. 6.5 and 6.6 the experimental results are shown as circular symbols and solid lines represent the results of the plate-membrane coupling model. Figures 6.5 and 6.6 show excellent agreement between analytical and experimental results.

Figure 6.7 presents the measured load-deflection curve and the analytical load-deflection curve obtained by using the plate-membrane coupling model and the finite element model. The analytical results

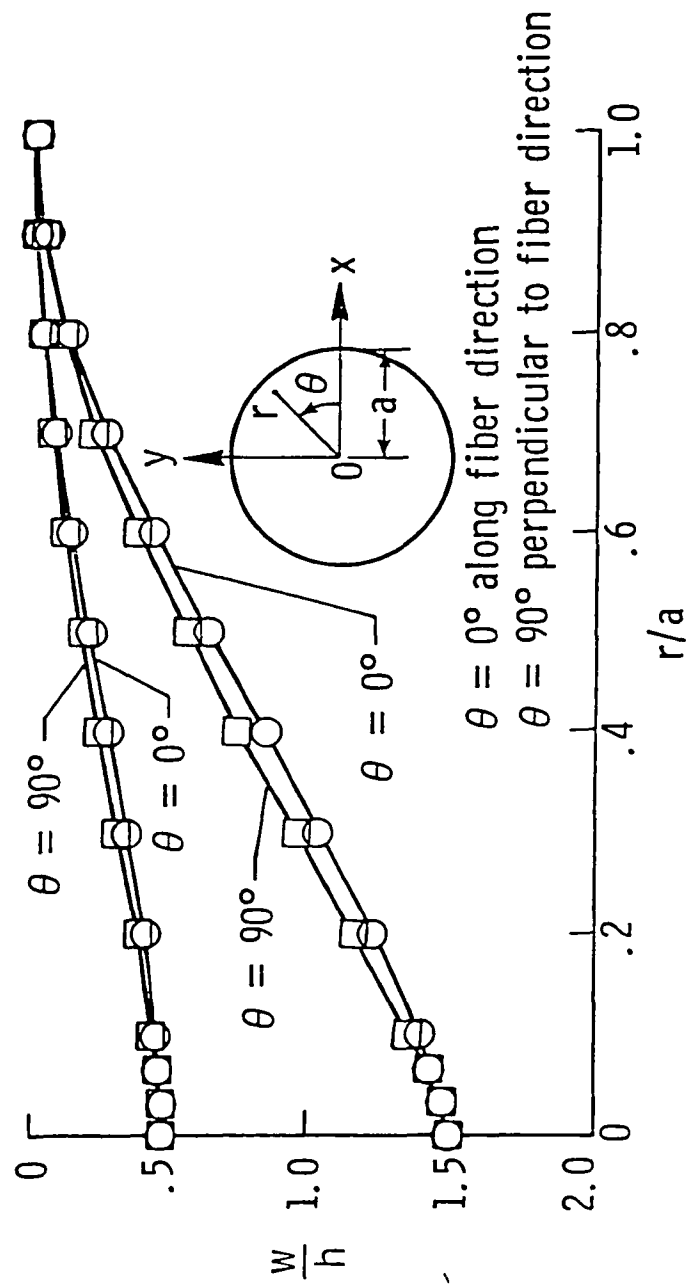


Fig. 6.4 Axisymmetric Validation for Quasi-Isotropic 8-Ply T300/5208 Laminate

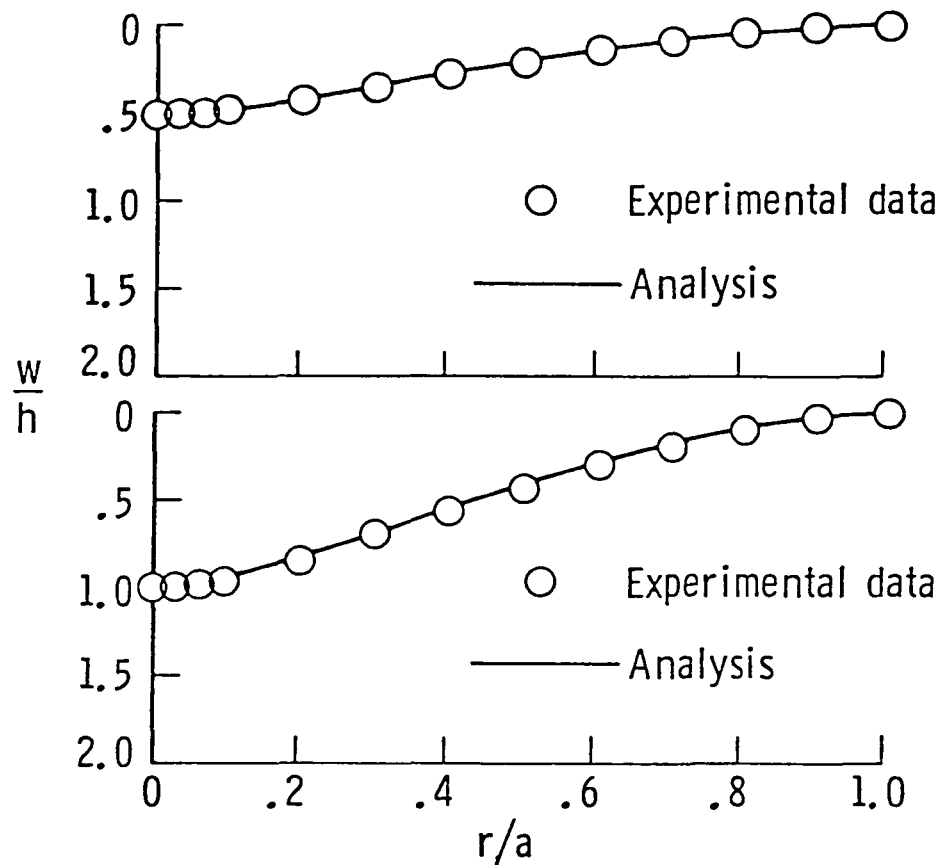


Fig. 6.5 Deflected Shapes for the Laminate Under Quasi-Static Point Loads for $w_0/h = 0.5$ and 1.0 .

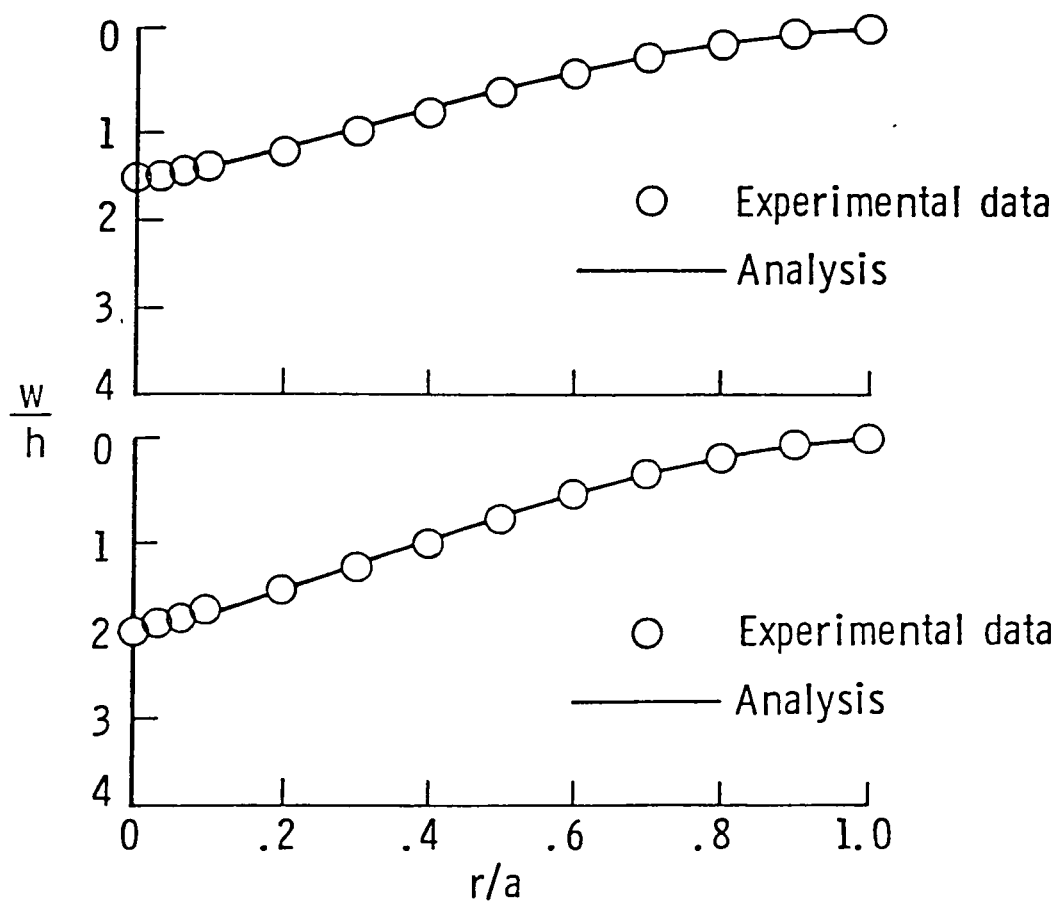


Fig. 6.6 Deflected Shapes for the Laminate Under Quasi-Static Point Loads for $w_0/h = 1.5$ and 2.0

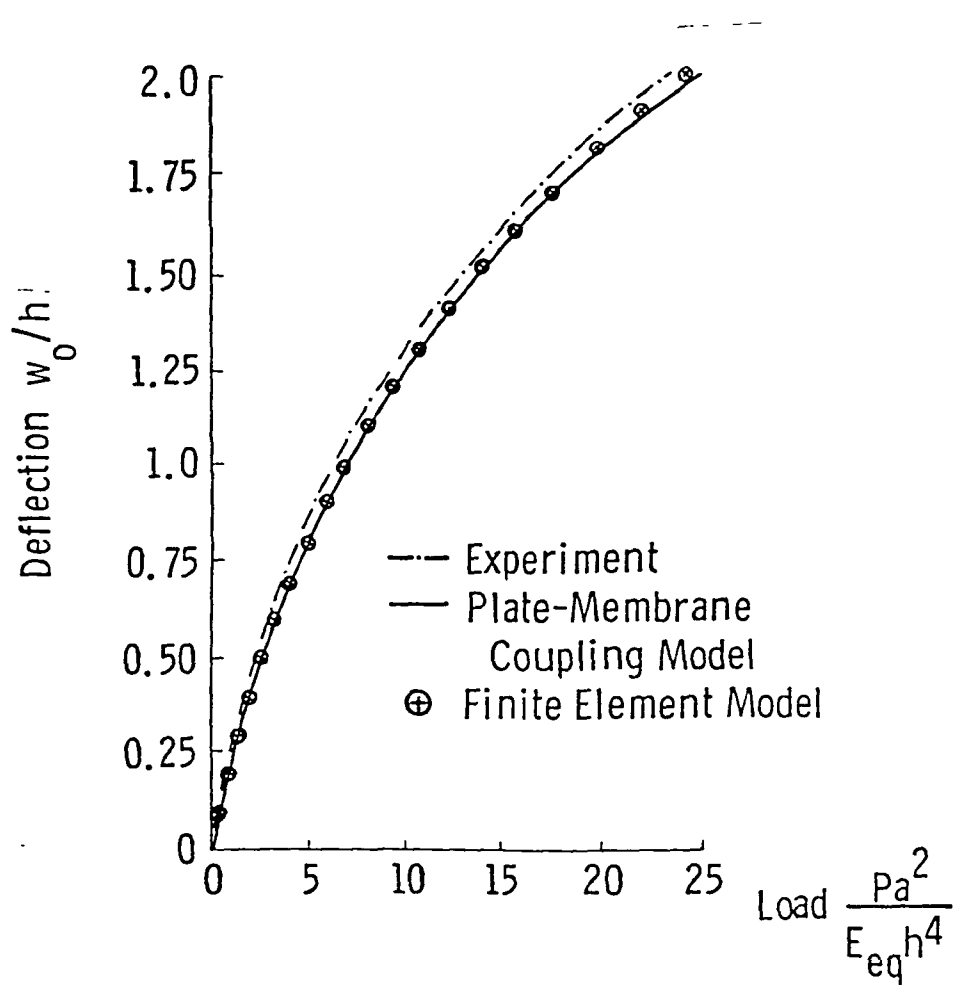


Fig. 6.7 Load-Deflection Curve Comparison

were found to be within six percent of the experimental results. These differences between the analytical and experimental results are probably due to experimental errors which might have been introduced while practically simulating the clamped boundary conditions.

6.5 Concluding Remarks

Eight ply T300/5208 quasi-isotropic circular plates were tested to verify the assumption of flexural isotropy and to study the large deformation behavior under central point loads. The experimental observations indicate that clamped circular quasi-isotropic laminates, subjected to a central point loading, behave as if they are almost flexurally isotropic and they show nearly axisymmetric bending behavior.

The experimentally obtained large deformation shapes and the load-displacement curves were compared with those obtained with the plate-membrane coupling model and the finite element solution. The experimental results are in good agreement with the analytical results obtained by using the plate-membrane coupling model and the finite element model.

In the next chapter, the large deformation shapes of the quasi-isotropic circular plate obtained by using the plate-membrane coupling model and the finite element model are used in conjunction with the fracture mechanics approach to describe the back face spalling phenomenon in thin quasi-isotropic circular laminates.

Chapter 7

BACK FACE SPALLING MODEL

7.1 Introduction

In Chaps. 4 and 5, the plate-membrane coupling model and the finite element model were developed to study the large deformation behavior of clamped circular quasi-isotropic laminates under static point loads. These models were verified by conducting tests on the clamped circular laminates. In this chapter a simple analytical model is developed to describe the back face spalling phenomenon in thin quasi-isotropic laminates. The model is based on the fracture mechanics principles and uses the large deformation shapes of the plates obtained earlier by using the plate-membrane coupling model. This analytical model is verified by conducting the experiments on thin quasi-isotropic T300/5208 circular plates.

7.2 Back Face Spalling Mechanism

As discussed in Chap. 1, for quasi-isotropic laminates under the central point loads, first visible damage occurs in the farthest ply from the load (i.e. 8th ply). The damage is in the form of a matrix cracking parallel to the fibers. Further increase in load level results in two dominant cracks in the 8th ply and surrounding these two cracks delaminations form between 7th and 8th plies. Additional increase in load causes these delaminations and cracking to propagate unstably in the fiber direction of the bottom ply. This unstable growth of delamina-

tions and the propagation of the two dominant cracks is known as the back face spalling phenomenon. During the back face spalling action, curved trajectory of the 8th ply center strip (formed by the two dominant cracks in the 8th ply) running under the load point in the fiber direction changes virtually to a straight line between the load point and the support (Fig. 7.1). A large fraction of strain energy from this 8th ply center strip is shed during this spalling action. This mechanism of the back face spalling is modeled by using the concepts of fracture mechanics in the following sections.

7.3 Fracture Mechanics Concepts

Any general deformation of a cracked body can be described by combination of three independent modes of deformation (Fig. 7.2). The three independent modes are: opening mode, sliding mode and tearing mode. Normal stresses give rise to the opening mode denoted as mode I. Inplane shear results in mode II or sliding mode. The tearing mode or mode III is caused by out-of-plane shear.

7.3.1 The Griffith Criterion

One of the basic criterion for fracture was established in 1921 by Griffith [54]. The Griffith energy criterion for fracture can be stated as "crack growth can occur if the energy required to form additional crack surfaces can be delivered by the system."

For example, consider a cracked plate of thickness B under a load P , as shown in Fig. 7.3. For a crack of size a the linear load-displacement relationship can be represented by line OA in Fig. 7.4. Similarly for a crack of size $a+da$ the load-displacement relation can

ORIGINAL PAGE IS
OF POOR QUALITY

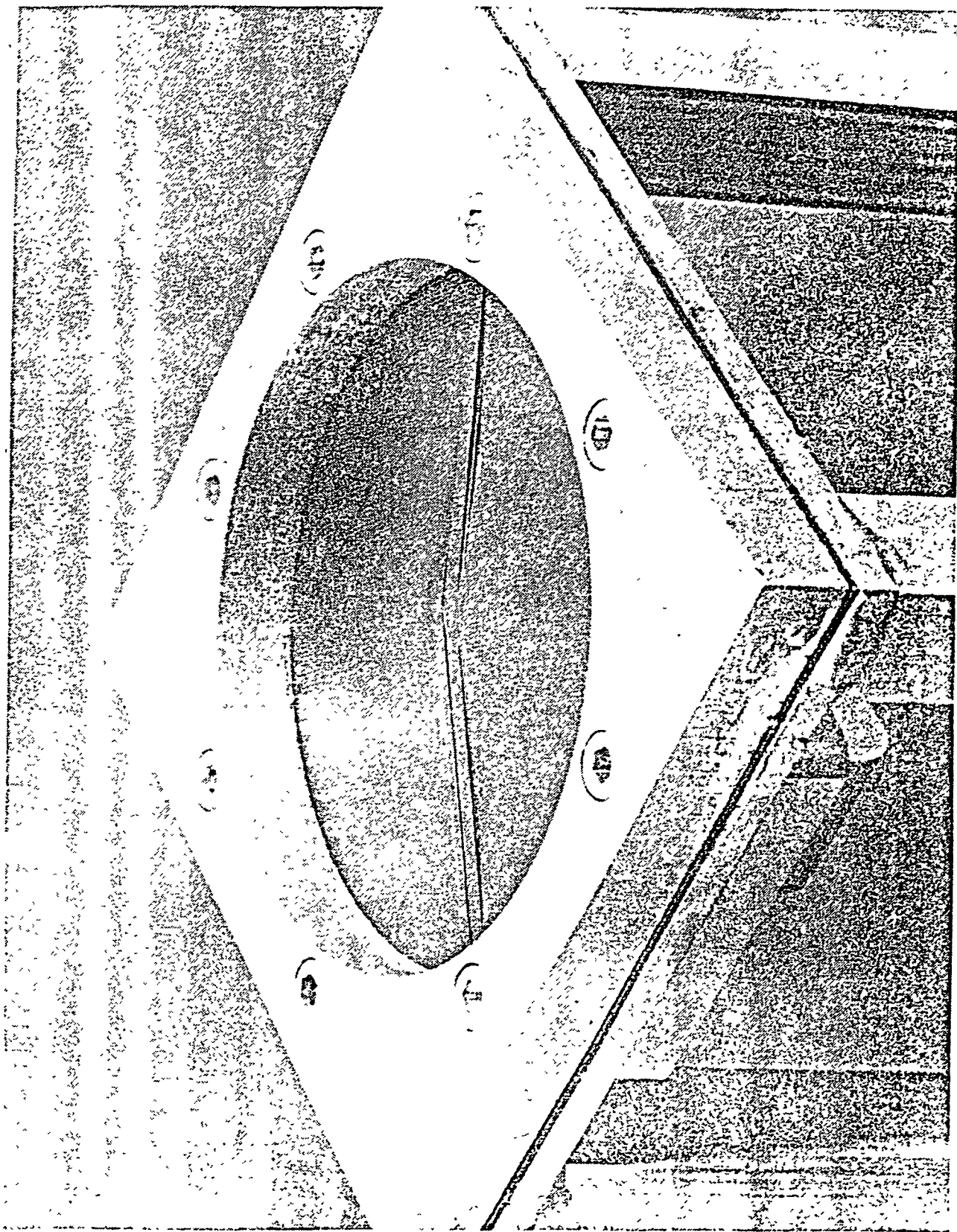


Fig. 7.1 Back Face Spalling in a Composite Plate

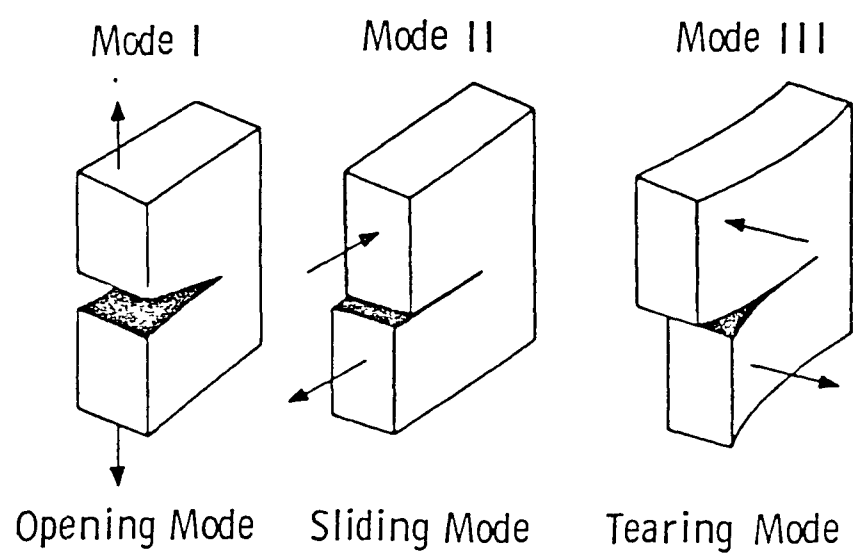


Fig. 7.2 Three Modes of Fracture

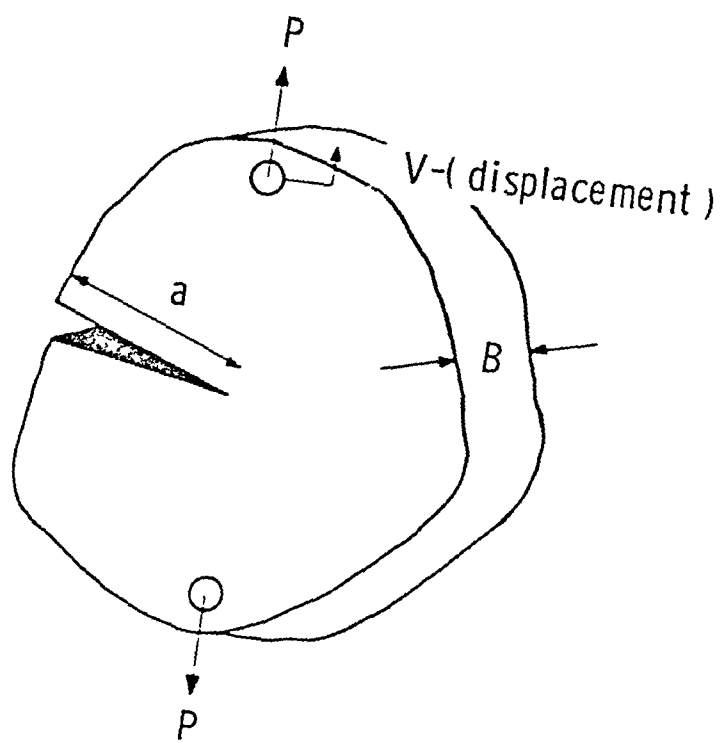


Fig. 7.3 Cracked Plate

be represented by the line OE (the line OE has a lower slope than the line OA because of reduced stiffness of the plate). If the ends of the plate are fixed and if crack extension takes place from A to $A+\Delta a$ at a load P_1 , the displacement remains constant and the load drops from point A to point B (Fig. 7.4). During this process elastic energy, represented by the area of triangle OAB, is released, which is $\frac{1}{2} \Delta P \cdot V$.

If crack extension takes place at constant load the displacement increases from point A to point E, i.e. by an amount ΔV (Fig. 7.4). Therefore the work done W , by the load is

$$W = P_1 \cdot \Delta V \quad (7.1)$$

The increase in the elastic energy of the plate is

$$\text{area (OEF)} - \text{area (OAC)} = \frac{1}{2} P_1 \cdot (V + \Delta V) - \frac{1}{2} P_1 \cdot V = \frac{1}{2} P_1 \cdot \Delta V \quad (7.2)$$

This increase in energy has to be provided by the load. The energy provided by the load is area (AEFC)

$$\text{area (AEFC)} = P_1 \cdot \Delta V \quad (7.3)$$

Equations (7.2) and (7.3) indicate that there remains an amount of energy equal to area (OAE). Area (OAE) can be expressed as

$$\text{area (OAE)} = \frac{1}{2} P_1 \cdot \Delta V = \frac{1}{2} \Delta P \cdot V + \frac{1}{2} \Delta P \cdot \Delta V \quad (7.4)$$

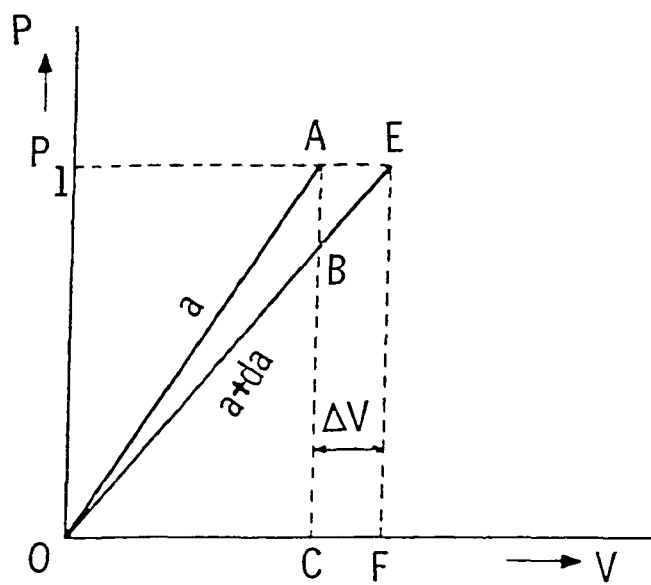


Fig. 7.4 Load-Displacement Curve

In Eq. (7.4) $\frac{1}{2} \Delta P \cdot \Delta V$ is the second order term and hence can be neglected. Thus it follows that area (OAB) \approx (OAE). This means that energy available for crack growth is the same in fixed grip and constant load case.

As seen earlier in the case of fixed grips the elastic energy is released as the crack grows from a to a+da. This elastic energy released per unit crack extension is called "elastic energy release rate" and is denoted by G. Since elastic energy is proportional to the strain energy, G is usually expressed in terms of the strain energy and is called "strain energy release rate."

7.3.2 Critical Strain Energy Release Rate G

Griffith [54] postulated that the crack growth occurs only when the strain energy release rate G exceeds certain critical values. This critical value is called a "critical strain energy release rate" and is denoted by G_c . This quantity G_c is a material property like the yield stress, Young's modulus and is different from material to material.

7.4 Back Face Spalling Model

As discussed earlier in the section 7.2, in quasi-isotropic laminates under the point loads, first visible damage occurs in the lowest ply in the form of two dominant cracks and surrounding these two cracks delaminations form between the 7th and 8th plies. With further increase in load at a certain plate center deflection w_0 , massive back face spalling occurs. During this spalling action the 8th ply center strip (formed by the two dominant cracks in the 8th ply) which is previously deformed in the same shape as that of a circular plate

changes virtually to a straight line between the load point and the support. This failure mechanism suggests that the complete back face spalling event can be explained by modeling the center strip in the 8th ply.

The center strip model developed here to describe the back face spalling phenomenon is based on the following assumptions:

1. Before the back face spalling occurs, the center strip in the 8th ply has the same deformed shape as that of a quasi-isotropic plate under the point load. Thus the radial displacements (u), the transverse displacements (w), and the rotations ($\frac{dw}{dr}$), in the center strip can be obtained by performing the large deflection analysis of the quasi-isotropic circular plate under point loads.
2. The initial delamination between the 7th ply and the center strip in the 8th ply is assumed to exist at the radius of inflection (the radius at which curvature in the strip is zero).
3. The change in stiffness of the plate due to the back face spalling action is assumed negligible and hence is not considered in the center strip model.
4. The effects of internal damage in the circular plate on the deformed shape of the plate are assumed to be negligible.
5. The center displacement of the plate is held constant and it does not change during the back face spalling action.

With these assumptions the center strip model was formulated and

solved to compute the strain energy release rates during the back face spalling action.

Consider a center strip in the 8th ply. The deformed shape of the strip is the same as that of the circular plate. The strip has a width b and the thickness t ($t = \text{one ply thickness}$). This center strip was discretized into m number of elements with $(m+1)$ nodes. The radial displacement (u), the transverse displacement (w), the rotation $(\frac{dw}{dr})$, and the curvature at each node were calculated by using the plate-membrane coupling analysis as described in Chap. 4. An initial delamination was assumed to exist between the center strip (of the 8th ply) and the 7th ply at the radius of inflection as shown in Fig. 7.5. This initial delamination was assumed to have a length equal to BD as shown in Fig. 7.5 where nodes B and D are the nodes adjacent to the node at the radius of inflection. Due to the presence of this initial delamination, the original deformed shape of the center strip ABCDEF as shown in Fig. 7.5 changed to the new deformed shape ABC'DEF. The center strip initially deformed between the nodes BD as BCD became straight as $BC'D$. Due to this change the original displacements, rotation and curvature at the node C have changed. The new displacements, rotation and curvature at the node C' were calculated as follows: The radial displacement at the node C' equal to

$$u_{C'} = \frac{(u_D - u_B)}{2(\Delta r)} \cdot (\Delta r) + u_B \quad (7.5)$$

The transverse displacement at the node C' equal to

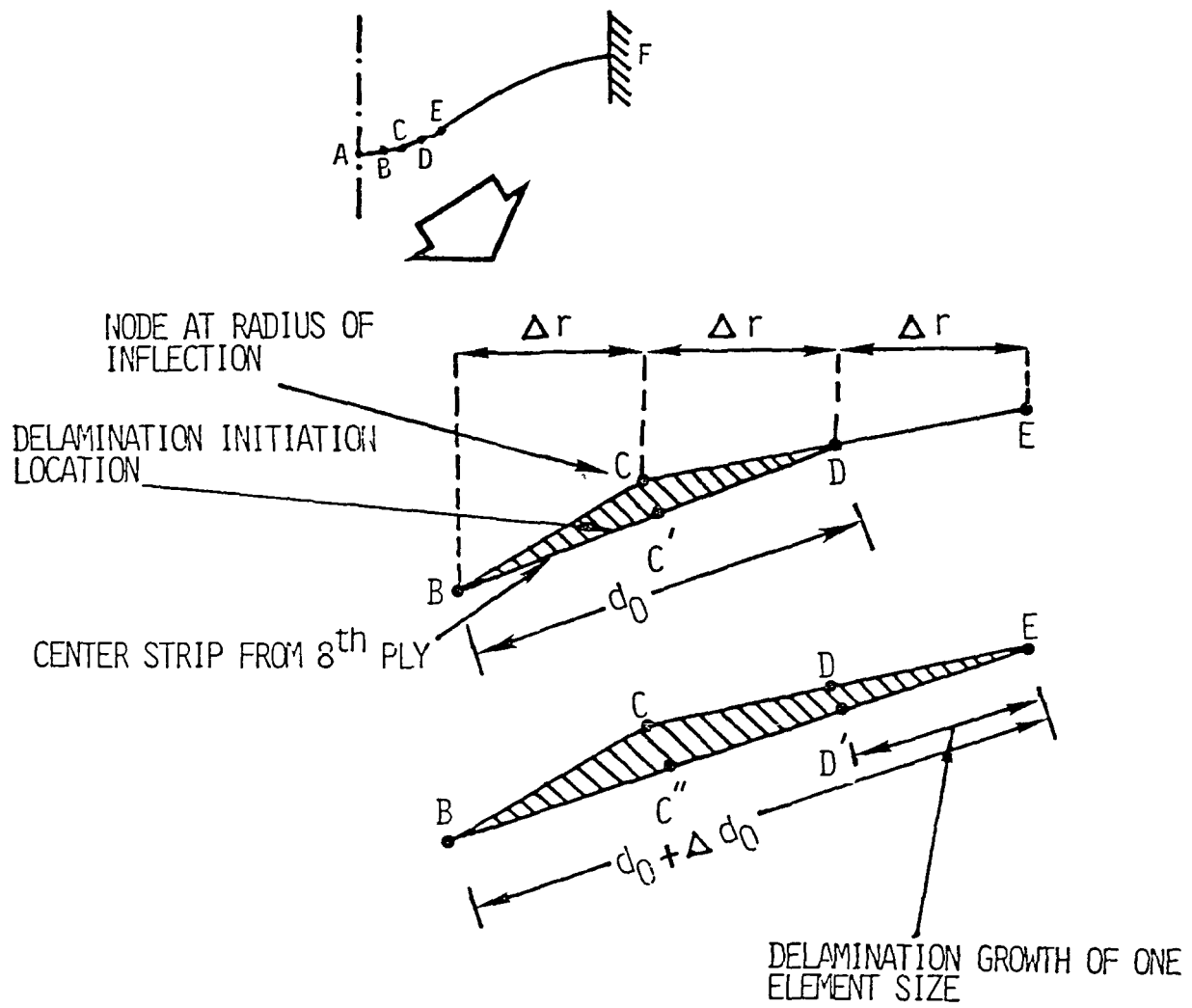


Fig. 7.5 Delaminations in Center Strip

$$w_{C'} = \frac{(w_D - w_B)}{2 \cdot (\Delta r)} \cdot (\Delta r) + w_B \quad (7.6)$$

The rotation at the node C' equal to

$$\left(\frac{dw}{dr}\right)_{C'} = \frac{(w_D - w_B)}{2 \cdot (\Delta r)} \quad (7.7)$$

The curvature at the node C' using finite difference approximation at C' is

$$\left(\frac{d^2 w}{dr^2}\right)_{C'} = \frac{w_D - 2 w_{C'} + w_B}{2 \cdot (\Delta r)} \quad (7.8)$$

Substituting equation (7.6) for $w_{C'}$ into Eq. (7.8)

$$\left(\frac{d^2 w}{dr^2}\right)_{C'} = 0 \quad (7.9)$$

Thus with an initial delamination the center strip had the same nodal displacements, rotations, and the curvatures as that of a plate, except at the node C' where the displacements and rotation are given by Eqs. (7.5)-(7.8). The curvature at the node C', however, is zero. By using these values of displacements, rotations and curvatures strain energy of the center strip was calculated as follows:

The strain energy U of a body in terms of stress (σ) and strain (ϵ) is given by:

$$U = \frac{1}{2} \int_{vol} \sigma \epsilon d(vol) \quad (7.10)$$

Only the transverse displacements (w) and the radial (axial) displacements (u) were assumed to be present in the strip. With these assumptions, the strip was modeled as a beam and hence only one stress σ_r exists in the center strip. The strain energy of the strip idealized as a beam is,

$$U = \frac{E_{rr}}{2} \int_{vol} \epsilon_r^2 d(vol) \quad (7.11)$$

where vol is the volume of the center strip and $E_{rr} = E_{11}$ is the elastic modulus of the strip in the fiber direction.

In Eq. (7.11) ϵ_r is the radial (axial) strain and is the sum of the membrane strains and the bending strains:

$$\epsilon_r = \frac{du}{dr} + \frac{1}{2} \left(\frac{dw}{dr} \right)^2 - z \frac{d^2 w}{dr^2} \quad (7.12)$$

where z in the Eq. (7.12) was measured with respect to the plate coordinate system.

A substitution of Eq. (7.12) in Eq. (7.11), gives the total strain energy of the strip U as

$$U = \frac{E_{11}}{2} \int_{vol} \left(\frac{du}{dr} + \frac{1}{2} \left(\frac{dw}{dr} \right)^2 - z \frac{d^2 w}{dr^2} \right)^2 d(vol) \quad (7.13)$$

Since z was measured with respect to the plate coordinate system, the limits of integration for the 8th ply center strip in z direction are $(3h/8)$ to $(h/2)$, therefore

$$U = \frac{E_{11}b}{2} \int_0^a \int_{3h/8}^{h/2} \left(\frac{du}{dr} + \frac{1}{2} \left(\frac{dw}{dr} \right)^2 - z \frac{d^2 w}{dr^2} \right)^2 dr dz \quad (7.14)$$

In order to evaluate the integral in Eq. (7.14), the center strip was discretized into m number of elements. The nodal displacements, the rotation, and the curvatures were computed by using the plate-membrane coupling model. These displacements, rotation and curvature were modified at the node C' (Fig. 7.5) by using Eqs. (7.5)-(7.9). Using these modified nodal displacements, Eq. (7.14) was numerically integrated to obtain a strain energy U of the center strip of the 8th ply. This procedure was repeated for various values of m , where number of elements m , were chosen as multiples of 10. About 60 elements and 90 elements were found necessary for a 25.4 mm and 38.1 mm length center strip respectively, to yield a converged solution for the strain energy U . Once the strain energy U was computed a delamination of one element size was allowed to grow in the outward direction as shown in Fig. 7.5. Due to this growth of delamination the deformed shape of the strip ABC'DEF changed into a new deformed shape ABC''D'EF as shown in Fig. 7.5. Thus due to growth of delamination the deformed shape of the strip between the nodes B and E is a continuous straight line. The new displacements, rotation and the curvatures at nodes C'', D' were calculated as follows:

The radial displacements of the nodes C'' and D' are

$$u_{C''} = \frac{(u_E - u_B)}{3 \cdot \Delta r} \cdot \Delta r + u_B \quad (7.15)$$

$$u_{D'} = \frac{(u_E - u_B)}{3 \cdot (\Delta r)} \cdot 2(\Delta r) + u_B \quad (7.16)$$

The transverse displacements at the nodes C'' and D' are

$$w_{C''} = \frac{(w_E - w_B)}{3 \cdot (\Delta r)} \cdot (\Delta r) + w_B \quad (7.17)$$

$$w_{D'} = \frac{(w_E - w_B)}{3 \cdot (\Delta r)} \cdot 2 (\Delta r) + w_B \quad (7.18)$$

The rotations at the nodes C'' and D' are

$$\left(\frac{dw}{dr}\right)_{C''} = \left(\frac{dw}{dr}\right)_{D'} = \frac{(w_E - w_B)}{3 \cdot (\Delta r)} \quad (7.19)$$

Since the deformed shape of the strip between the nodes B and E was straight, the curvatures at the nodes C'' and D' were zero. Therefore

$$\left(\frac{d^2 w}{dr^2}\right)_{C''} = \left(\frac{d^2 w}{dr^2}\right)_{D'} = 0 \quad (7.20)$$

Thus for the new deformed shape ABC''D'EF except at the nodes C'' and D' the nodal displacements, rotations, and curvatures of the center strip are the same as those obtained by using the plate-membrane coupling model. For the nodes C'', D', the displacements, rotations, and curvatures are given by Eqs. (7.15)-(7.20). Using these values of nodal displacements, rotations, and curvatures into equation (7.14), the new strain energy U₁ of the center strip with the deformation shape ABC''D'EF was calculated.

This strain energy U₁ corresponding to the deformed shape ABC''D'EF was found less than the strain energy U corresponding to the deformed

shape ABC'DEF. Thus during the delamination growth from BD to BE (Fig. 7.5), the amount of strain energy released ΔU is given by

$$\Delta U = U - U_1 \quad (7.21)$$

Expressing the strain energy released ΔU in terms of strain energy release rate G , one has

$$G = \frac{\partial U}{\partial A} \approx \frac{\Delta U}{\Delta A} \quad (7.22)$$

where

$$\Delta A = b \times \Delta d_0 \quad (7.23)$$

b = width of the strip

Δd_0 = length of the delamination growth

This G corresponds to a delamination length of $d_0 + \Delta d_0$.

By using the above procedure, the strain energy release rates were calculated by incrementing the delamination outward by one element length each time, until the delamination reached the clamped edge (node F, Fig. 7.5). This strain energy release rate analysis was repeated for several $(\frac{w_0}{h})$ ratios and for two plate sizes with radii 25.4 mm and 38.1 mm.

7.5 Strain Energy Release Rate Results

In this section the strain energy release rates obtained by using the center strip model are presented for two plate sizes with radii 25.4 mm and 38.1 mm. For each plate size strain energy release rates were

determined for each delamination length. Figures 7.6 and 7.7 present G as a function of delamination length for various values of plate center deflection w_0 . For all delamination lengths, Fig. 7.6 shows that larger values of center deflection w_0 gave larger values of the strain energy release rates. Figure 7.6 also indicates that beyond delamination length of 15 mm, the strain energy release rates reach a constant value and do no depend on the delamination length.

Figure 7.7 presents the strain energy release rate variation with delamination length for a plate radius of 38.1 mm, for various values of center deflection. This figure shows similar trends as Fig. 7.6.

7.6 Discussion of the Back Face Spalling Phenomenon

As pointed out earlier, the back face spalling phenomenon occurs spontaneously (i.e. a center strip from the 8th ply peels off unstably). This unstable peeling action suggests that, during delamination growth between the 7th ply and the center strip from the 8th ply, the strain energy release rate G must exceed the critical strain energy release rate for delamination growth. Assuming that the spalling occurs due to the peeling action alone, i.e. only mode I is present, then by using the critical strain energy release rate value of the T300/5208 graphite/epoxy material in the opening mode $(G_I)_c$, the back face spalling damage can be predicted by using the center strip model.

Consider a 25.4 mm radius plate. The critical strain energy release rate value $(G_I)_c$, for the T300/5208 graphite/epoxy material is 0.1 KJ/m^2 [55]. Figure 7.6 shows that for the plate center deflections of 1.60 mm or less, the calculated G values to grow initial delamination length $BC'D$ to new delamination length $BC''D'E$ (Fig. 7.5), are less than

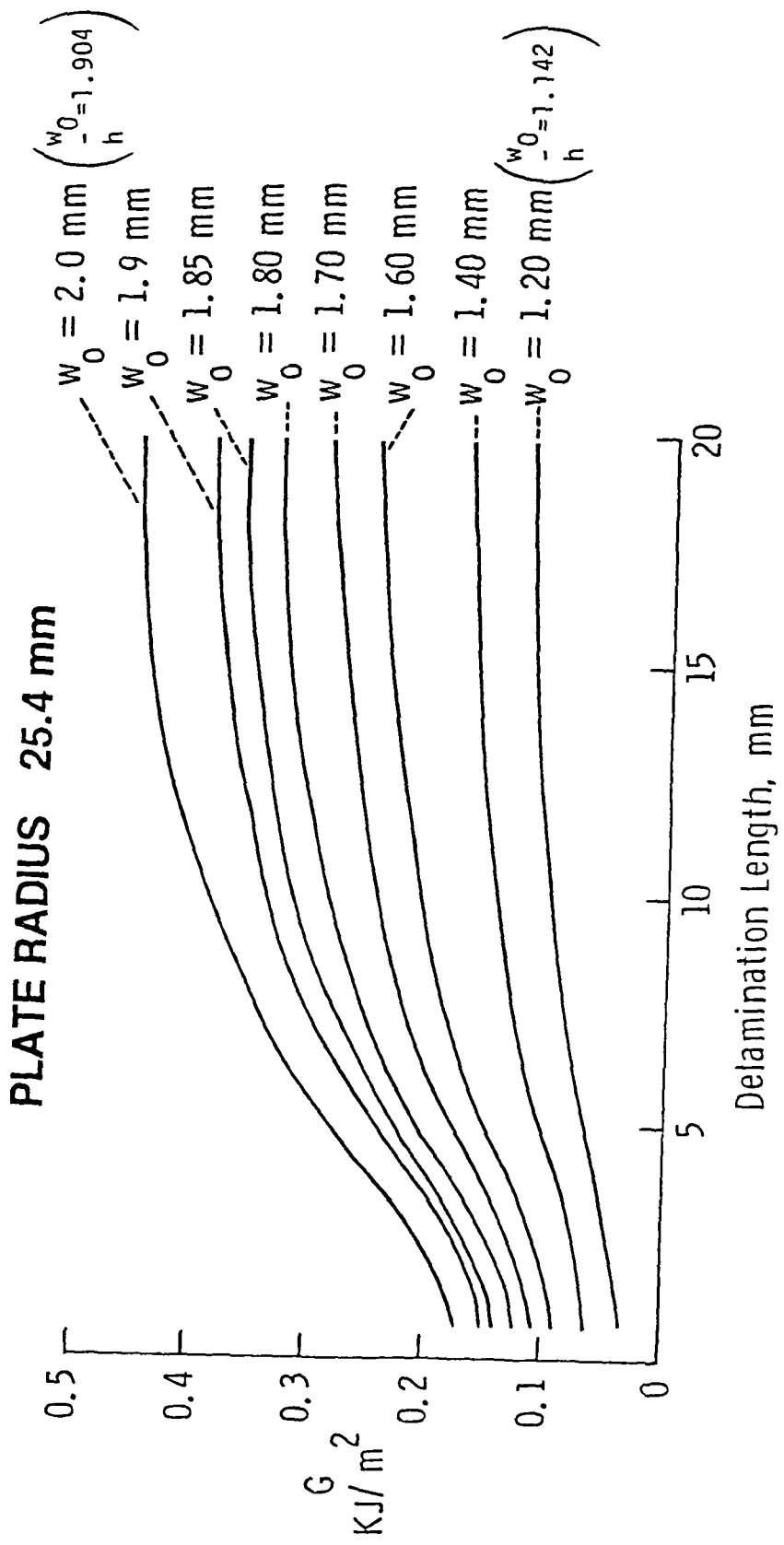


Fig. 7.6 Variation of Strain Energy Release Rates with Delamination Length for a Plate Radius of 25.4 mm

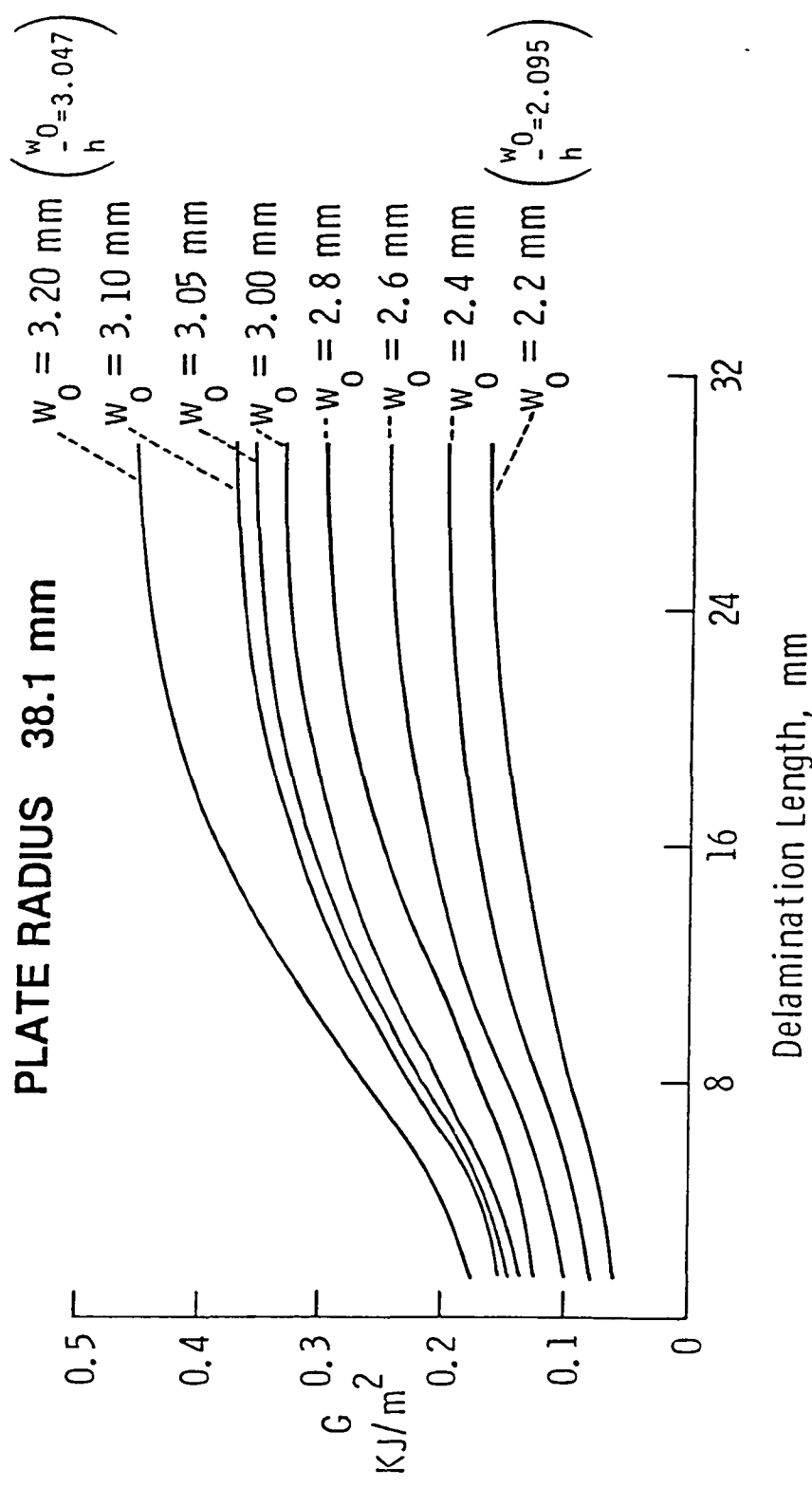


Fig. 7.7 Variation of Strain Energy Release Rates with Delamination Length for a Plate Radius of 38.1 mm

0.1 KJ/m² or $(G_I)_C$ value. This indicates that for the plate center deflections of 1.60 mm or less, the initial delamination between the center strip and the 7th ply will not grow. However, for the plate center deflections of 1.70 mm or more, Fig. 7.6 shows that the calculated G values to grow the initial delamination length BC'D to new delamination length BC''D'E (Fig. 7.5), exceed $(G_I)_C$ value. Therefore, for plate center deflections equal to or greater than 1.7 mm the initial delamination between the center strip and the 7th ply will grow unstably and the center strip will peel off, thus resulting into the back face spalling action. Figure 7.6 also indicates that if the initial delamination lengths are large, the back face spalling action will occur at lower values of central deflection w_0 . For example consider an initial delamination length of 5 mm. From Fig. 7.6 the calculated G value required for growth in the initial delamination length of 5 mm exceeds 0.1 KJ/m² or $(G_I)_C$ value when w_0 is 1.60 mm. That means even at the center deflection of 1.60 mm, the initial delamination of 5 mm length will grow unstably resulting in the back face spalling action.

Next consider the larger plate of 38.1 mm radius. Figure 7.7 shows that for the plate center deflection of 2.6 mm or more, the calculated G values to grow an initial delamination length BC'D to new delamination length BC''D'E (Fig. 7.5), exceeds $(G_I)_C$ value. Therefore, for plate center deflections equal to or greater than 2.6 mm the initial delamination between the center strip and the 7th ply will grow unstably and the center strip will peel off, thus resulting into the back face spalling action. Figure 7.7 also indicates that if the delamination lengths are large, the back face spalling action will occur at lower values of center deflections w_0 .

7.7 Back Face Spalling Experiments

To verify the back face spalling model, experiments were performed on clamped circular quasi-isotropic plates. Quasi-isotropic graphite/epoxy laminates, with the stacking sequence of [45/0/-45/90]_S and the material properties given in Table 2.1 were used for the tests. Circular laminates with 25.4 mm and 38.1 mm radii were bolted between two annular steel plates. By using the torque-bolt arrangement (similar to the one described earlier in Chap. 6), a 25.4 mm diameter steel ball was pushed against the laminate. Although the ball diameter was 25.4 mm, which was half the size of the plate diameter, the contact radius between the ball and the plate was very small (of the order of 1 mm) and thus pushing of the steel ball simulated the desired static point load conditions. A vertical DCDT was used to measure the center deflection w_0 . The static load on the plate was gradually increased by using the torque bolt, till the back face spalling occurred. At this instant the center deflection w_0 of the plate was measured. From the experiments it was observed that for 25.4 mm radius plate, the back face spalling occurred within the center deflections, ranging from 1.80 mm to 1.90 mm. For 38.1 mm radius plate the back face spalling occurred at higher center deflections, with the values ranging from 3.00 mm to 3.1 mm.

The back face spalling experiments show that for the two plate sizes studied, a plate with 25.4 mm radius failed at a mean center deflection of 1.85 mm. The critical strain energy release rate (G_c), corresponding to the center deflection $w_0 = 1.85$ mm from Fig. 7.6 is about 0.14 KJ/m². In the case of 38.1 mm radius plate back face spalling occurred at a mean center deflection of 3.05 mm. The critical strain energy release rate G_c , corresponding to the center deflection w_0

= 3.05 mm from Fig.7.7 is 0.147 KJ/m^2 . Thus the experimentally obtained critical strain energy release rates G_C , are about $0.14\text{--}0.15 \text{ KJ/m}^2$. Comparing these values with the opening mode critical strain energy release rate $(G_I)_C$ [55], G_C is somewhat higher than $(G_I)_C$. This may be due to the presence of shear sliding mode (mode II) in addition to the opening mode (mode I) during the back face spalling action.

Earlier investigators [56,57] have shown that for brittle systems like T300/5208 graphite/epoxy material under the mixed mode situations (opening mode and shear sliding mode), the failure is predominantly governed by the critical strain energy release rate in the opening mode. The present experimental values of G_C are very close to $(G_I)_C$. Hence, even though in the back face spalling phenomenon a mixed mode (mode I + mode II) situation may exist, the critical strain energy release rate in the opening mode $(G_I)_C$, probably governs the back face spalling mechanism in thin composite laminates.

7.8 Prevention of Back Face Spalling in Thin Composite Laminates

The analytical and experimental results form the back face spalling model suggest that, the composite laminates with higher $(G_I)_C$ values than T300/5208, will have better resistance to the back face spalling. For example consider composites AS1/3501-6 made by Hercules. Russel and Street [58] obtained the $(G_I)_C$ value of AS1/3501-6 as 0.15 KJ/m^2 . This value is fifty percent higher than that for T300/5208 composites. Therefore AS1/3501-6 composites may have better resistance to the back face spalling when compared to T300/5208 composites. Recently considerable attention is focused on the development of tough resins. The tough systems of composites usually have higher $(G_I)_C$ values than brittle

system of composites [56]. Mall and Johnson [59] determined the $(G_I)_C$ values for FM-300 tough matrix composite by Hexel. They found that $(G_I)_C$ values are 7 to 10 times higher than the brittle systems (i.e. T300/5208 and AS1/3501-6). Hunston [60] and O'Brien et al. [61] obtained $(G_I)_C$ values for F-185 matrix composite by American Cyanamide. They reported the value of $(G_I)_C$ for T6000/F185 composite as 2 KJ/m^2 , which is about 20 times higher than the T300/5208 values. Thus tough systems of composites may have superior resistance to back face spalling when compared to brittle systems of composite.

Some investigators [62] have found that "stitching" of the laminate decreases delamination. The stitching of the laminate may be particularly useful to prevent the back face spalling, as stitching has a restraining effect on peeling action. Another possible way to prevent the back face spalling, is to use woven ply on the back of the laminate, because the weave will not allow center strip from the bottom ply to peel off without involving cross-ply strips.

Finally, in the present analysis the plates were assumed to be stress free. If the plates are pre-stressed, the plates would react differently to the center point load. For the center point load, the center deflection w_0 of the tensile pre-stressed plate would be less compared to the center deflection w_0 of the plate with zero pre-stresses. This is because the tensile pre-stressed plate is more stiff compared to the plate with zero pre-stresses [27]. This suggests that the back face spalling would occur at higher loads in thin composite plates pre-stressed with tensile stresses compared to the initially stress free plates.

7.9 Conclusions

In this chapter a simple analytical model was developed to understand the back face spalling phenomenon in thin quasi-isotropic laminates. The model uses the large deformation plate shapes obtained by using the plate-membrane coupling model in conjunction with the fracture mechanics principles. The strain energy release rates during back face spalling action were obtained by using the analytical model for two plate sizes with plate radii of 25.4 mm and 38.1 mm. Experiments were performed on the 8 ply T300/5208 quasi-isotropic circular plates to obtain critical strain energy release rates during back face spalling action. Good agreement was observed between experimental and analytical results. Experimental and analytical results indicated that the back face spalling phenomenon in 8 ply T300/5208 quasi-isotropic laminates is governed by the critical strain energy release rate $(G_I)_C$ in the opening mode. Therefore the back face spalling in composites can be reduced by using the material with higher $(G_I)_C$ values than $(G_I)_C$ value of the brittle systems composite like T300/5208. Another possible way to prevent the back face spalling, is to stitch the laminate or to use a woven ply on the back of the laminate.

Chapter 8

SUMMARY AND CONCLUSIONS

The present investigation is concerned with the failure analysis of composite plates under low-velocity impact loads. This analysis is particularly important to understand the damage mechanics and to develop composites with improved impact resistance. The state-of-art of the low-velocity impact problem was reviewed and important aspects of the problem such as deformation mechanics, back face spalling phenomenon were investigated. Three models, plate-membrane coupling model, finite element model, and back face spalling model were developed. These investigations should help in understanding the low velocity impact problem and lead to better design and analysis of composite structures.

The low velocity impact problem in T300/5208 graphite/epoxy circular quasi-isotropic plates was formulated by replacing impact type point loads with equivalent quasi-static loads. The quasi-isotropic plates were modeled as isotropic plates having the flexural stiffness components equivalent to the flexural stiffness components of the quasi-isotropic plates. A plate-membrane coupling model and a finite element model were developed to obtain the large deformation behavior of circular composite plates under point loads. These models were verified by conducting plate mechanics experiments. From the study of these analytical models and experiments the following conclusions can be made:

1. A circular quasi-isotropic plate with stacking sequence of $[45/0/-45/90]_S$ can be modeled as an isotropic plate having flexural stiffness components equivalent to those of a quasi-isotropic plate.
2. The large deformation behavior of circular isotropic membranes subjected to arbitrary axisymmetric loading can be obtained by solving a single nonlinear governing equation in terms of radial stress using the finite difference method in conjunction with Newton-Raphson method.
3. Accurate large deformation behavior of thin circular quasi-isotropic plates can be obtained by using a simple plate-membrane coupling model.
4. The functional form of the deformed shape of the plate undergoing large deformations is different from the small deflection plate solution. The deformed shape is a function of the center point displacements and thus is different for different load levels. Furthermore, for a plate undergoing large deformations, there is an inward movement of the radii of points of inflection.

In addition to the deformation mechanics, a study was undertaken to develop a damage mechanics. From the experiments on thin laminates it was observed that first visible damage in circular quasi-isotropic laminates under quasi-static point loads occur on the back surface of the laminate in the form of spalling. To understand this back face spalling phenomenon, a simple model using the large deformation behavior

of thin composite plates in conjunction with fracture mechanics principles was developed. This back face spalling model was verified by conducting experiments on thin circular quasi-isotropic plates. The study resulted in the following conclusions:

1. The back face spalling action in thin composite laminates is a spontaneous action and can be modeled by using the fracture mechanics principles.
2. Mixed mode (I + II) type deformations probably occurs during the back face spalling action. However, analysis and experiments suggest that the mode I (opening mode) may be the dominant mechanism and governs the delamination growth during the spalling action.
3. Back face spalling model shows that the back face spalling occurs only when the strain energy release rate G , exceeds the critical value of strain energy release rate in the opening mode $(G_I)_C$. This implies that back face spalling can be reduced or prevented by:
 - (a) use of tough composites having higher values of $(G_I)_C$ compared to brittle resin systems like T300/5208.
 - (b) Stitching of the laminate, as stitching has a restraining effect on peeling action.
 - (c) To use woven ply on the back of the laminate, because the weave will not allow center strip from the bottom ply to peel off without involving cross-ply strips.

The present investigation has also shown that future research is warranted in the following areas:

1. To include effects of the internal damages in composite plates and develop more general deformation mechanics.
2. To extend the back face spalling model for rectangular composite plates by developing 2-D analysis.
3. To devleop a technique for identifying individual strain energy release rates in different modes I, II, and III during back face spalling action.
4. To determine the effects of stitching on the back face spalling action in thin composite laminates.
5. To extend present analysis to thick composite plates by incorporating the effects due to shear.
6. To perform a dynamic analysis and compare it with the quasi-static analysis.

REFERENCES

1. Rhodes, M. D., Williams, J. G., and Starnes, J. H., "Effect of Low-Velocity Impact Damage on the Compressive Strength of Graphite-Epoxy Hat-Stiffened Panels," NASA TN D-8411, April, 1977.
2. Starnes, J. H., Rhodes, M. D., and Williams, J. G., "Effect of Impact Damage and Holes on the Compressive Strength of a Graphite/Epoxy Laminate," Nondestructive Evaluation and Flaw Criticality for Composite Materials, ASTM STP 696, American Society for Testing and Materials, 1979, pp. 145-171.
3. Starnes, J. H. and Williams, J. G., "Failure Characteristics of Graphite-Epoxy Structural Components Loaded in Compression," NASA TM 84552, September 1982.
4. Lal, K. M., "Residual Strength Assessment of Low Velocity Impact Damage of Graphite-Epoxy Laminates," Journal of Reinforced Plastics and Composites, Vol. 2, October 1983, pp. 277-287.
5. Ramkumar, R. L., "Composite Impact Damage Susceptibility," Naval Air Development Center, NADC-79068-60, January 1981.
6. Wardle, M. W. and Tokarsky, E. W., "Drop Weight Impact Testing of Laminates Reinforced with Kevlar Aramid Fibers, E-Glass, and Graphite," Composite Technology Review, Vol. 5, No. 1, Spring 1983, pp. 4-10.
7. Hayes, S. V. and Adams, D. F., "Rate Sensitivity Tensile Impact Properties of Fully and Partially Loaded Unidirectional Composites," Journal of Testing and Evaluation, Vol. 10, No. 2, March 1982, pp. 61-68.
8. Elber, W., "Failure Mechanics in Low-Velocity Impacts on Thin Composite Plates," NASA TP 2152, May 1983.
9. Labor, J. D., "Service/Maintainability of Advanced Composite Structures," Airforce Flight Dynamic Laboratory Technical Report, AFFDL-TR-78155, November 1978.
10. Bhatia, N. M., "Impact Damage Tolerance of Thick Graphite/Epoxy Laminates," Naval Air Development Center, NADC-79038-60, January 1979.
11. Hertzberg, P. E., Smith, B. W., and Miller, A. G., "Effect of Matrix Resin on the Impact Fracture Characteristics of Graphite-Epoxy Laminates," NASA CR 165784, January 1982.

12. Rhodes, M. D. and Williams, J. G., "Concepts for Improving the Damage Tolerance of Composite Compression Panels," Proceedings of 5th DoD/NASA Conference on Fiberous Composites in Structural Design, New Orleans, Louisiana, January 1981.
13. McQuillen, E. J. and Gause, L. W., "Low Velocity Transverse Normal Impact of Graphite Epoxy Composite Laminates," Journal of Composite Materials, Vol. 10, January 1976.
14. Gause, L. W. and Huang, S. L., "Compression Fatigue of Impact Damaged Graphite Epoxy Sandwich Beams," Naval Air Development Center, NADC-77305-60, April 1978.
15. Card, M. F. and Rhodes, M. D., "Graphite-Epoxy Panel Compression Strength Reduction Due to Local Impact," Proceedings of the Agard 50th Meeting of the Structures and Materials Panel Specialists Meetings, Athens, Greece, April 1980.
16. Cristescu, N., Malvern, L. E., and Sierakowski, R. L., "Failure Mechanisms in Composite Plates Impacted by Blunt-Ended Penetrators," Foreign Object Impact Damage to Composites, ASTM STP 568, American Society for Testing and Materials, 1975, pp. 159-172.
17. Gause, L. W., "Low Speed, Hard Object Impact on Thick Graphite-Epoxy Plates," Naval Air Development Center, NADC-78051-60, May 1978.
18. Gause, L. M., Rosenfeld, M. S., and Vining, R. E., "Effect of Impact Damage on the XFV-12A Composite Wing Box," Naval Air Development Center, NADC-79255-60, August 1979.
19. Llorens, R. E. and Gause, L. W., "Low Velocity, Transverse Normal Impact of a Clamped Plate," Naval Air Development Center, NADC-81250-60, October 1981.
20. Dobyns, A. L. and Porter, T. R., "A Study of the Structural Integrity of Graphite/Epoxy Composite Structure Subjected to Low Velocity Impact," Polymer Engineering and Science, Vol. 21, No. 8, June 1981.
21. Dobyns, A. L., "Analysis of Simply Supported Orthotropic Plates Subjected to Static and Dynamic Loads," AIAA Paper No. 80-0608, April 1980.
22. Hayes, S. V. and Rybicki, E. F., "The Development of a Low Velocity Impact Methodology for Hybrid Material Systems," Advanced Technology Center Report, ATC R-92000/1CR-63, July 1981.
23. Greszczuk, L. B., "Damage in Composite Materials Due to Low Velocity Impact," Zukas, J. A., et al., Impact Dynamics, John Wiley and Sons, New York, 1982.

24. Bostaph, G. M. and Elber W., "Static Indentation on Composite Plates for Impact Susceptibility Evaluation," Proceedings of the Army Symposium on Solid Mechanics, Cape Cod, Massachusetts, September 1982.
25. Lal, K. M., "Low Velocity Transverse Impact Behavior of 8-Ply, Graphite-Epoxy Laminates," Journal of Reinforced Plastics and Composites, Vol. 2, October 1983, pp. 216-225.
26. Shivakumar, K. N., Elber, W., and Illg, W., "Analysis of Progressive Damage in Thin Circular Laminates Due to Static Equivalent Impact Loads," Proceedings of the AIAA/ASME/ASCE/AHS 24th Structures, Structural Dynamics and Materials Conference, Lake Tahoe, Nevada, May 1983.
27. Timoshenko, S. and Woinowsky-Krieger, S., Theory of Plates and Shells, McGraw-Hill, New York, 1959.
28. Washizu, K., Variational Methods in Elasticity and Plasticity, Pergamon Press, Second Edition, 1974.
29. Hencky, H., "Über den Spannungszustand in Kreisrunden Platten mit verschwindender Biegungssteifigkeit," Zeitschrift Fur Mathematic Und Physik, 63, pp. 311-317, 1915.
30. Dickey, R. W., "The Plane Circular Elastic Surface Under Normal Pressure," Archive for Rational Mechanics and Analysis, Vol. 26, September 1967, pp. 219-236.
31. Shaw, F. S. and Perron, N., "A Numerical Solution for the Non-Linear Deflections of the Membranes," Journal of Applied Mechanics, Vol. 21, June 1954, pp. 117-128.
32. Goldberg, M. A. and Pifko, A. B., "Iterative and Power Series Solutions for the Large Deflection of an Annular Membrane," AIAA Journal, Vol. 1, September 1963, pp. 211-215.
33. Weinitschke, H. J., "Some Mathematical Problems in the Non-Linear Theory of Elastic Membranes, Plates and Shells," Trends in Applications of Pure Mathematics to Mechanics (Lecce Symp.), G. Fichera (ed.), Pitman (London), 1976, pp. 409-424.
34. Weinitschke, H. J., "On Axisymmetric Deformations of Nonlinear Elastic Membranes," Mechanics Today, Vol. 5, Pergamon Press, 1980, pp. 523-542.
35. Callegari, A. J. and Reiss, E. L., "Nonlinear Boundary Value Problems for the Circular Membrane," Archives for Rational Mechanics and Analysis, Vol. 31, April 1968, pp. 390-400.
36. Rao, G. V., Raju, K. K., and Raju, I. S., "Finite Element Formulation for the Large Amplitude Free Vibrations of Beams and Orthotropic Plates," Journal of Computers and Structures, Vol. 6, June 1976, pp. 169-172.

37. Rao, G. V., Raju, I. S., and Raju, K. K., "Nonlinear Vibrations of Beams Considering Shear Deformation and Rotary Inertia," AIAA Journal, Vol. 14, May 1976, pp. 685-687.
38. Raju, K. K. and Rao, G. V., "Nonlinear Vibrations of Beams Carrying Concentrated Mass," Journal of Sound and Vibrations, Vol. 48, October 1976, pp. 445-449.
39. Raju, K. K., Sastry, B. P. and Rao, G. V., "A Finite Element Formulation for the Large Amplitude Vibrations of Tapered Beams," Journal of Sound and Vibrations, Vol. 47, August 1976, pp. 595-598.
40. Mei, C., "Nonlinear Vibrations of Beams by Matrix Displacement Method," AIAA Journal, Vol. 10, March 1972, pp. 335-337.
41. Mei, C., "Finite Element Displacement Method for Large Amplitude Free Oscillations of Beams and Plates," Journal of Computers and Structures, Vol. 3, January 1972, pp. 163-164.
42. Mei, C., "A Finite Element Approach for Nonlinear Panel Flutter," AIAA Journal, Vol. 15, August 1977, pp. 1107-1110.
43. Rao, G. V. and Rao, K. S., "Large Amplitude Supersonic Flutter of Panels with Ends Elastically Restrained Against Rotation," Journal of Computers and Structures, Vol. 11, March 1980, pp. 197-201.
44. Mei, C., Narayan Swami, R., and Rao, G. V., "Large Amplitude Free Flexural Vibrations of Thin Plates of Arbitrary Shape," Journal of Computers and Structures, Vol. 10, August 1979, pp. 675-681.
45. Prathap, G. and Vardhan, T. K., "Comments on the Finite Element Formulation for the Large Amplitude Vibration of Tapered Beams and Beams Carrying Concentrated Mass," Journal of Sound and Vibration, Vol. 54, September 1977, pp. 147-148.
46. Sarma, B. S. and Vardhan, T. K., "Certain Discussion on the Finite Element Formulation of the Nonlinear Vibration Analysis," Journal of Computers and Structures, Vol. 15, June 1982, pp. 643-646.
47. Prathap, G. and Bhashyam, G. R., "Comments on Nonlinear Vibrations of Immovably Supported Beams by Finite Element Method," AIAA Journal, Vol. 18, June 1980, pp. 773-734.
48. Prathap, G., "Comments on Large Amplitude Vibration of Circular Plates," Journal of Sound and Vibrations, Vol. 54, October 1977, pp. 601-602.
49. Love, A. E. H., A Treatise on the Mathematical Theory of Elasticity, Dover Publications, Inc., New York, 1944.
50. Jones, R. M., Mechanics of Composite Materials, McGraw-Hill, New York, 1975.

51. Trench, W. F., Advanced Calculus, Harper and Row, Publishers, New York, 1978.
52. Scarborough, J. B., Numerical Mathematical Analysis, The John Hopkins Press, 1966,
53. Kao, R., and Perrone, N., "Large Deflections of Axisymmetric Circular Membranes," International Journal of Solid Structures, Vol. 7, December 1971, pp. 1601-1612.
54. Griffith, A. A., "The Theory of Rupture," Proceedings of 1st International Congress Applied Mechanics, June 1924, pp. 55-63.
55. Ramkumar, R. L., "Performance of a Quantitative Study of Instability Related Delamination Growth," NASA CR 166046, March 1983.
56. Johnson, W. S. and Mangalgiri, P. D., "Influence of the Resin on Interlaminar Mixed-Mode Fracture," NASA TM 87571, June 1985.
57. O'Brien, T. K., "Mixed-Mode Strain-Energy-Release Rate Effects on Edge Delamination of Composites," Effects of Defects in Composite Materials, ASTM STP 846, American Society for Testing and Materials, 1984, pp. 125-142.
58. Russell, A. J. and Street, K. N., "Moisture and Temperature Effects on the Mixed-Mode Delamination Fracture of Unidirectional Graphite/Epoxy," Delamination and Debonding of Materials, ASTM STP 876, American Society Testing and Materials, 1985.
59. Mall, S. and Johnson, W. S., "Characterization of Mode I and Mixed Mode Failure of Adhesive Bonds Between Composite Adherends," NASA TM 86335, February 1985.
60. Hunston, D. L., "Composite Interlaminar Fracture: Effects of Matrix Fracture Energy," Composite Technology Review, Vol. 6, No. 4, Winter 1984, pp. 176-180.
61. O'Brien, T. K., Johnston, N. J., Morris, D. H., and Simmonds, R. A., "Determination of Interlaminar Fracture Toughness and Fracture Mode Dependence of Composites Using the Edge Delamination Test," Proceedings of the International Conference on Testing, Evaluation, and Quality Control of Composites, University of Surrey, Guilford, England, T. Feest, Ed., Butterworths, London, September 1983, pp. 223-232.
62. Williams, J. G. and Rhodes, M. D., "The Effect of Resin on the Impact Damage Tolerance of Graphite-Epoxy Laminates," NASA TM-83213, October 1981.

APPENDICES

APPENDIX A

NEWTON-RAPHSON METHOD FOR NONLINEAR SYSTEM

The purpose of this appendix is to present the Newton-Raphson method for solution of nonlinear simultaneous algebraic equations. First a method is explained with reference to a function involving one variable. Next, the method for a general n variable system is presented. Last, the method is illustrated with the set of nonlinear equations involving 5 variables derived in Chap. 3 for the membrane problem.

A.1 Newton-Raphson Method for One Dependent Variable

Consider a function $F(x)$ of one dependent variable x . The objective is to find the root of the equations $F(x) = 0$. Figure A-1 presents the function $F(x)$ graphically. The Newton-Raphson method is an iterative method which continuously updates an initial approximation until the actual root is found. Consider an approximation $x = x_0$ as the root. The value of $F(x)$ is $F(x_0)$ at point P as shown in Fig. A-1. At P draw a tangent to the curve. The tangent intersects the X axis at T. Therefore the next approximation for the root is $x_1 = x_0 + \Delta x_0$ where Δx_0 is MT in Fig. A-1. Next draw a tangent at point Q. This tangent intersects the X axis at T_1 . Therefore the next approximation for the root is $x_2 = x_1 + \Delta x_1$. Imagine a third tangent is drawn at R, this tangent will cut the X axis at some point T_2 between T_1 and S. Therefore points T, T_1 , T_2 , ... will approach the point S as a limit,

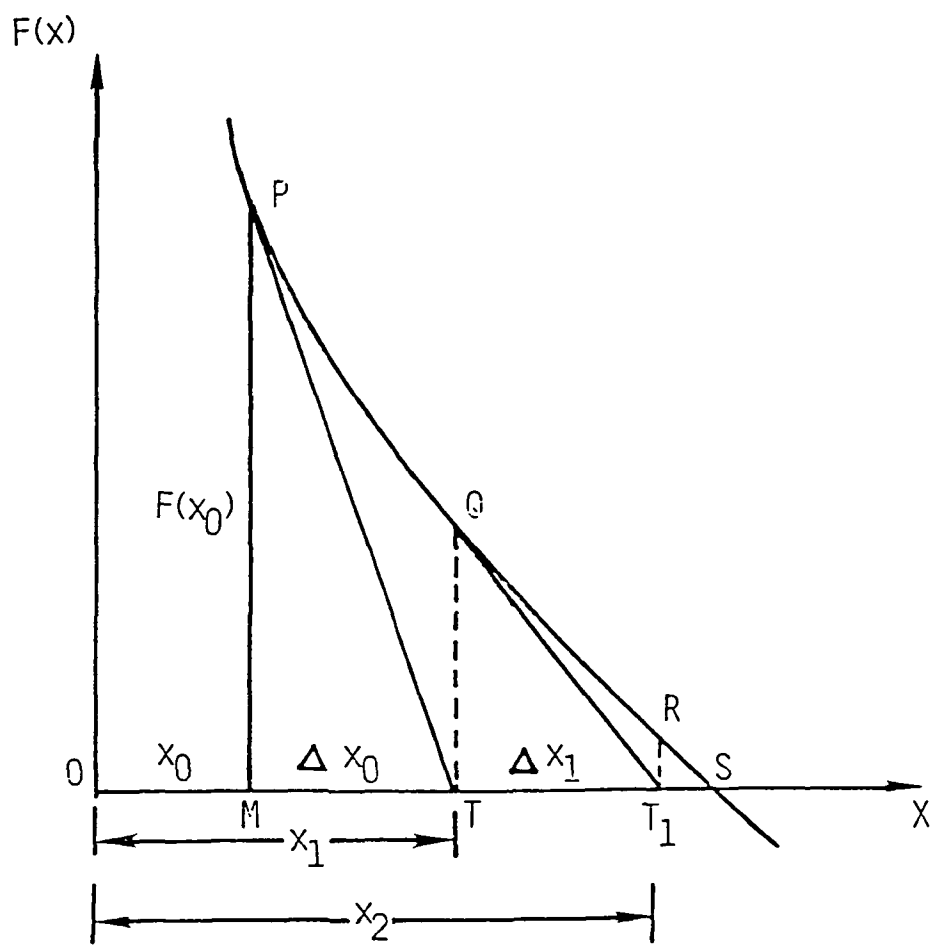


Fig. A-1 Graphical Representation of The Newton-Raphson Method

that is, the intercepts OT, OT_1, OT_2, \dots will approach the intercept OS as a limit. But OS represents the real root of the equation $F(x) = 0$. Hence the quantities OT, OT_1, OT_2, \dots are successive approximations to the desired root. The fundamental formula for finding the root of the equation $F(x) = 0$ can be derived by using Fig. A-1 as follows:

Consider Fig. A-1. Let $MT = \Delta x_0$, and $TT_1 = \Delta x_1$, etc. The slope of the graph at P is $F'(x_0)$. From the Fig. A-1, $PM = F(x_0)$ and slope at the point $P = \tan \angle XTP = F'(x_0) = -\frac{F(x_0)}{\Delta x_0}$. Therefore

$$\Delta x_0 = \frac{-F(x_0)}{F'(x_0)} \quad (A-1)$$

The improved value of the root is then

$$x_1 = x_0 + \Delta x_0 \quad (A-2)$$

Similarly succeeding approximations are

$$x_2 = x_1 + \Delta x_1$$

$$x_3 = x_2 + \Delta x_2 \quad (A-3)$$

$$x_n = x_{n-1} + \Delta x_{n-1}$$

where

$$\Delta x_i = \frac{-F(x_i)}{F'(x_i)} \quad (A-4)$$

where $F'(x_i)$ is the derivative of the $F(x)$ at x_i . In the one-variable

case $F'(x) = [J(x_i)]_{1 \times 1}$, where $[J]$ is called as Jacobian.

The value of x is updated till the $|\Delta x_i| < \epsilon$, where ϵ is the specified tolerance. The corresponding root of the equation $F(x) = 0$ is x_i . The above procedure can be generalized for n variables as follows:

A.2 Newton-Raphson Method for n Variables

Consider a system of simultaneous nonlinear algebraic equations with n variables, $(x_1, x_2, x_3, \dots, x_n)$ as

$$f_1(x_1, x_2, x_3, \dots, x_n) = R_1$$

$$f_2(x_1, x_2, x_3, \dots, x_n) = R_2 \quad (A-5)$$

⋮

$$f_n(x_1, x_2, x_3, \dots, x_n) = R_n$$

Equations in (A-5) can be represented as

$$\{F(x)\} = \{(f_1 - R_1), (f_2 - R_2), \dots, (f_n - R_n)\}^T \quad (A-6)$$

The approximate solution of the nonlinear system (Eq. (A-5)) can be obtained starting with an initial approximation X_0 as follows:

With the initial approximation X_0 , $[J(X_0)]$ is first evaluated as:

$$[J(x_0)] = \begin{bmatrix} \frac{\partial f_1(x)}{\partial x_1} & \frac{\partial f_1(x)}{\partial x_2} & \dots & \frac{\partial f_1(x)}{\partial x_n} \\ \frac{\partial f_2(x)}{\partial x_1} & \frac{\partial f_2(x)}{\partial x_2} & \dots & \frac{\partial f_2(x)}{\partial x_n} \\ \vdots & \vdots & & \vdots \\ \frac{\partial f_n(x)}{\partial x_1} & \dots & \dots & \frac{\partial f_n(x)}{\partial x_n} \end{bmatrix} \quad (A-7)$$

$\{x\} = \{x_0\}$

Next $\{F(x_0)\}$ is evaluated by using Eq. (A-6). With these values of $\{F(x_0)\}$ and $[J(x_0)]$ the next approximation x_1 is obtained as,

$$\{x_1\} = \{x_0\}_{n \times 1} - [[J(x_0)]_{n \times n}^{-1} \{F(x_0)\}_{n+1}] \quad (A-8)$$

With this new value of $\{x_1\}$, $\{F(x_1)\}$ and $[J(x_1)]$ are calculated and then $\{x_2\}$ is calculated as:

$$\{x_2\} = \{x_1\}_{n \times 1} - [[J(x_1)]_{n \times n}^{-1} \{F(x_1)\}_{n \times 1}] \quad (A-9)$$

This iterative procedure is continued till the maximum difference in $\{x\}$ values between the successive iterations is within specified tolerance of ϵ i.e.

$$\text{Max } | \{x_i\} - \{x_{i-1}\} | < \epsilon \quad (A-10)$$

When Eq. (A-10) is satisfied the iterations are stopped and the solution of Eq. (A-5) is $\{x_i\}$.

A.3 Example Problem

In the illustrative example (section 3.3.2), a circular membrane with radius a and thickness h , and with a uniform loading over the region $0 < \frac{r}{a} < 0.5$ was analyzed. By using the four region idealization and a finite difference technique, five nonlinear equations were obtained. These five nonlinear equations (Eqs. (3.26), (3.27), (3.28), (3.29) and (3.24)) were expressed in terms of normalized stresses as:

$$-3 \bar{\sigma}_r(0) + 4 \bar{\sigma}_r(1) - \bar{\sigma}_r(2) = 0 \quad (\text{A-11})$$

$$-0.5 \bar{\sigma}_r(0) \bar{\sigma}_r^2(1) - 2 \bar{\sigma}_r^3(1) + 2.5 \bar{\sigma}_r(2) \bar{\sigma}_r^2(1) = -\frac{1}{128} \quad (\text{A-12})$$

$$\bar{\sigma}_r(1) \bar{\sigma}_r^2(2) - 8 \bar{\sigma}_r^3(2) + 7 \bar{\sigma}_r(3) \bar{\sigma}_r^2(2) = -\frac{1}{32} \quad (\text{A-13})$$

$$4.5 \bar{\sigma}_r(4) \bar{\sigma}_r^2(3) + 1.5 \bar{\sigma}_r(2) \bar{\sigma}_r^2(3) - 6 \bar{\sigma}_r^3(3) = -\frac{1}{216} \quad (\text{A-14})$$

$$\bar{\sigma}_r(4) (6.69) - 8 \bar{\sigma}_r(3) + 2 \bar{\sigma}_r(2) = 0 \quad (\text{A-15})$$

where

$$\bar{\sigma}_r = \frac{\sigma_r}{\left(\frac{p^2 a^2 E_{eq}}{h^2}\right)^{1/3}}$$

Using Newton-Raphson method [$J(\bar{\sigma}_r)$] was obtained as:

$$\left[\begin{array}{ccccc} -3 & 4 & -1 & 0 & 0 \\ -\bar{\sigma}_r(0) \bar{\sigma}_r(1) & & & & \\ -0.5 \bar{\sigma}_r^2(1) & -6 \bar{\sigma}_r^2(1) & 2.5 \bar{\sigma}_r^2(1) & 0 & 0 \\ +5 \bar{\sigma}_r(2) \bar{\sigma}_r(1) & & & & \\ \\ 0 & \bar{\sigma}_r^2(2) & 2 \bar{\sigma}_r(1) \bar{\sigma}_r(2) & 7 \bar{\sigma}_r^2(2) & 0 \\ & & -24 \bar{\sigma}_r^2(2) & & \\ & & +14 \bar{\sigma}_r(3) \bar{\sigma}_r(2) & & \\ \\ 0 & 0 & 1.5 \bar{\sigma}_r^2(3) & 9 \bar{\sigma}_r(4) \bar{\sigma}_r(3) & 4.5 \bar{\sigma}_r^2(3) \\ & & & +3 \bar{\sigma}_r(2) \bar{\sigma}_r(3) & \\ & & & -18 \bar{\sigma}_r^2(3) & \\ \\ 0 & 0 & 2 & -8 & 6.69 \end{array} \right] \quad (A-16)$$

An initial approximation for the normalized stress $\bar{\sigma}_r(0)$, $\bar{\sigma}_r(1)$, $\bar{\sigma}_r(2)$, $\bar{\sigma}_r(3)$, and $\bar{\sigma}_r(4)$ was assumed as unity. With this assumption, the function $\{F(\bar{\sigma}_r)\}$ and $[J(\bar{\sigma}_r)]$ were evaluated. They are

$$[F(\bar{\sigma}_r)] = \begin{Bmatrix} 0 \\ 1/128 \\ 1/32 \\ 1/216 \\ 0.69 \end{Bmatrix} \quad [J(\bar{\sigma}_r)] = \begin{bmatrix} -3 & 4 & -1 & 0 & 0 \\ -0.5 & -2 & 2.5 & 0 & 0 \\ 0 & 1 & -8 & 7 & 0 \\ 0 & 0 & 1.5 & -6 & 4.5 \\ 0 & 0 & 2 & -8 & 6.69 \end{bmatrix} \quad (A-17)$$

The next approximation for $\{\bar{\sigma}_r\}$ was obtained by using Eq. (A-8) as:

$$\begin{Bmatrix} \bar{\sigma}_r(0) \\ \bar{\sigma}_r(1) \\ \bar{\sigma}_r(2) \\ \bar{\sigma}_r(3) \\ \bar{\sigma}_r(4) \end{Bmatrix} = \begin{Bmatrix} 1 \\ 1 \\ 1 \\ 1 \\ 1 \end{Bmatrix} - \begin{bmatrix} -3 & 4 & -1 & 0 & 0 \\ -0.5 & -2 & 2.5 & 0 & 0 \\ 0 & 1 & -8 & 7 & 0 \\ 0 & 0 & 1.5 & -6 & 4.5 \\ 0 & 0 & 2 & -8 & 6.69 \end{bmatrix} \begin{Bmatrix} 0 \\ 1/128 \\ 1/32 \\ 1/216 \\ 0.69 \end{Bmatrix} \quad (A-18)$$

Solution of Eq. (A-18) is

$$\left\{ \begin{array}{l} \bar{\sigma}_r(0) \\ \bar{\sigma}_r(1) \\ \bar{\sigma}_r(2) \\ \bar{\sigma}_r(3) \\ \bar{\sigma}_r(4) \end{array} \right\} = \left\{ \begin{array}{l} 0.02039 \\ 0.01941 \\ 0.01648 \\ 0.01160 \\ 0.0089 \end{array} \right\} \quad (A-19)$$

The above procedure was repeated and the next approximation to $\{\bar{\sigma}_r\}$ was obtained as:

$$\left\{ \begin{array}{l} \bar{\sigma}_r(0) \\ \bar{\sigma}_r(1) \\ \bar{\sigma}_r(2) \\ \bar{\sigma}_r(3) \\ \bar{\sigma}_r(4) \end{array} \right\} = \left\{ \begin{array}{l} 27.5628 \\ 27.7630 \\ 28.3637 \\ 27.3757 \\ 24.2568 \end{array} \right\} \quad (A-20)$$

This iterative procedure was continued till the maximum difference in $\{\bar{\sigma}_r\}$ values between the successive iterations was less than $1E-6$ or $\max |\Delta \bar{\sigma}_{r_i}| < 1E-6$. The solution converged after 18 iterations, and the corresponding normalized stress values were: $\bar{\sigma}_r(0) = 0.3156$, $\bar{\sigma}_r(1) = 0.3065$, $\bar{\sigma}_r(2) = 0.2726$, $\bar{\sigma}_r(3) = 0.2233$, and $\bar{\sigma}_r(4) = 0.1851$.

APPENDIX B

LARGE DEFLECTION SOLUTION OF CLAMPED CIRCULAR PLATE LOADED AT
THE CENTER USING THE ENERGY METHOD

Consider clamped circular plate of thickness h and radius a , subjected to a center point load P . The classical large deflection solution based on the energy method assumes that the deformation shape of a clamped circular plate under center point load has the same equation as in the case of small deflections, therefore

$$w(r) = w_0 \left[1 - \left(\frac{r^2}{a^2} \right)^2 + 2 \left(\frac{r^2}{a^2} \right) \ln \left(\frac{r}{a} \right) \right] \quad (B-1)$$

where w_0 is the central displacement of the plate.

The corresponding strain energy of bending can be written as [27]

$$U_b = \frac{D_{eq}}{2} \int_0^{2\pi} \int_0^a \left[\left(\frac{d^2 w}{dr^2} \right)^2 + \frac{1}{r^2} \left(\frac{dw}{dr} \right)^2 + \frac{2\nu_{eq}}{r} \frac{dw}{dr} \frac{d^2 w}{dr^2} \right] r dr d\theta \quad (B-2)$$

$$= \frac{8 \pi D_{eq} w_0^2}{a^2} \quad (B-3)$$

where D_{eq} is a flexural modulus and is given by

$$D_{eq} = \frac{E_{eq} h^3}{12 (1-\nu_{eq}^2)} \quad (B-4)$$

where E_{eq} and ν_{eq} are the equivalent Young's modulus and Poisson's ratio for the quasi-isotropic plate and were obtained by using the technique described in Chap. 2.

For the radial displacement u , classical solution assumes the expression

$$u = r(a - r)(C_1 + C_2r) \quad (B-5)$$

Equation (B-5) satisfies the boundary conditions that u must vanish at the center and at the edge of the plate.

The strain energy due to stretching of the middle plane of the plate is given by [27]

$$U_m = \frac{\pi E_{eq} h}{(1-\nu_{eq}^2)} \int_0^a (\epsilon_r^2 + \epsilon_\theta^2 + 2\nu_{eq} \epsilon_r \epsilon_\theta) r dr \quad (B-6)$$

where ϵ_r and ϵ_θ are radial and tangential strains and are given by Eqs (3.3) and (3.4) from Chap. 3 as:

$$\epsilon_r = \frac{du}{dr} + \frac{1}{2} \left(\frac{dw}{dr} \right)^2 \quad (B-7)$$

$$\epsilon_\theta = \frac{u}{r} \quad (B-8)$$

From expressions (B-1) and (B-5) for the displacements, the strain components ϵ_r and ϵ_θ were calculated by using Eq. (B-7) and (B-8). Substituting these strain components in Eq. (B-6) strain energy due to

stretching U_m was obtained as

$$\begin{aligned}
 U_m = & \frac{\pi E_{eq} h a^2}{(1 - v_{eq}^2)} [0.250 C_1^2 a^2 + 0.1167 C_2^2 a^4 \\
 & + 0.300 C_1 C_2 a^3 + 0.06332 C_1 \frac{w_0^2}{a} \\
 & + 0.09851 C_2 w_0^2 + 0.18240 \frac{w_0^4}{a^4}]
 \end{aligned} \quad (B-9)$$

The constants C_1 and C_2 were determined from the condition that the total energy of the plate for a position of equilibrium is minimum. Hence

$$\frac{\partial U_m}{\partial C_1} = 0 \text{ and } \frac{\partial U_m}{\partial C_2} = 0 \quad (B-10)$$

Substituting Eq. (B-9) for U_m , following two linear equations for C_1 and C_2 were obtained

$$0.50 C_1 a^2 + 0.300 C_2 a^3 - 0.06332 \frac{w_0^2}{a} \quad (B-11)$$

$$0.2334 C_2 a^4 + 0.300 C_1 a^3 = - 0.09851 w_0^2 \quad (B-12)$$

Equations (B-11) and (B-12) were solved simultaneously and C_1 and C_2 were obtained as:

$$C_1 = 0.5531 \frac{w_0^2}{a^3} \quad C_2 = -1.133 \frac{w_0^2}{a^4} \quad (B-13)$$

Substituting values of C_1 and C_2 from Eq. (B-13) into Eq. (B-9), U_m was obtained as

$$U_m = \frac{\pi E_{eq} h}{(1 - v_{eq}^2)} [0.14409 \frac{w_0^4}{a^2}] \quad (B-14)$$

Total potential energy π_p was written as the sum of the bending energy and stretching energy minus the work done, therefore

$$\pi_p = \frac{8 \pi D_{eq} w_0^2}{a^2} + 0.114409 \frac{w_0^4}{a^2} \frac{\pi E_{eq} h}{(1 - v_{eq}^2)} - P w_0 \quad (B-15)$$

Minimizing π_p with respect to w_0 , following relationship between load P and w_0 was obtained

$$16 \pi D_{eq} \frac{w_0}{a^2} + 0.57636 \frac{w_0^3}{a^2} \frac{\pi E_{eq} h}{(1 - v_{eq}^2)} = P \quad (B-16)$$

Substituting $D_{eq} = \frac{E_{eq} h^3}{12 (1 - v_{eq}^2)}$, and rearranging the terms, Eq. (B-16) can be written as:

$$\left(\frac{w_0}{h}\right) + 0.433 \left(\frac{w_0}{h}\right)^3 = 0.2157 \frac{P a^2}{E_{eq} h^4} \quad (B-17)$$

Equation (B-17) is the classical large deflection solution for clamped circular plate under central point load P .

APPENDIX C

DERIVATION FOR THE RADIUS OF INFLECTION

The classical large deformation theory [27], assumes the deformation shape of a clamped circular plate under central point load as:

$$w(r) = w_0 \left[1 - \left(\frac{r^2}{a^2} \right) + 2 \left(\frac{r^2}{a^2} \right) \ln \left(\frac{r}{a} \right) \right] \quad (C-1)$$

Furthermore the classical theory assumes that the functional form of the deformation shape remains unchanged for various values of central deflection, w_0 . Thus the radius of inflection (the radius at which curvature is zero) is independent of $\left(\frac{w_0}{h}\right)$. The radius of inflection can be obtained as follows:

By differentiating Eq. (C-1) twice, curvature can be written as

$$\frac{d^2 w}{dr^2} = \frac{4 w_0}{a^2} \left[1 + \ln \left(\frac{r}{a} \right) \right] \quad (C-2)$$

The radius of inflection is the radius at which $\left(\frac{d^2 w}{dr^2}\right) = 0$.

Hence,

$$\frac{4 w_0}{a^2} \left[1 + \ln \left(\frac{r}{a} \right) \right] = 0 \quad (C-3)$$

yields the radius of point of inflection as

$$\left(\frac{r}{a} \right) = e^{-1} = 0.3678 \quad (C-4)$$

BIOGRAPHY

Ajit Dhundiraj Kelkar was born in Indore, India, on April 10, 1953. He graduated from N. M. V. High School, Pune, India, in 1969. In 1975 he graduated from the College of Engineering, Pune, with a Bachelor's degree in Mechanical Engineering. He then took a position in Kirloskar Cummins Engine Company, Pune, as a Production Engineer. In 1978, he joined Telco, Pune, as a Quality Control Engineer. In 1979, he came to the United States to pursue graduate studies. He received his Master of Science degree in Mechanical Engineering from the South Dakota State University, Brookings, South Dakota in 1981. In August 1981, he moved to Norfolk, Virginia and since then he has worked towards a Ph.D. degree in Engineering Mechanics at the Old Dominion University, Norfolk, Virginia under a joint NASA-ODU Research Participation in Aeronautics Program.